# Volatiles in Protoplanetary Disks

Thesis by

Ke Zhang

In Partial Fulfillment of the Requirements

for the Degree of

Doctor of Philosophy

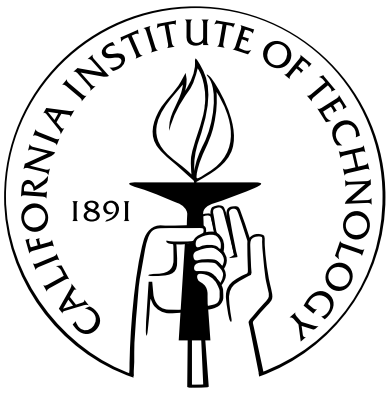


California Institute of Technology

Pasadena, California

2015

(Defended May 15, 2015)

# Acknowledgements

First and foremost, I would like to thank my advisor, Geoffrey Blake, for his patience, guidance, support, and inspiration that made this thesis possible. In retrospect, I am so grateful to have chosen Geoff as my mentor. He is a very special kind of advisor, so rare in the fast-paced world, who can be incredibly patient, waiting for a student to find her passion. But once the student has made up her mind, and starts to ask for resources, opportunities, and attention, he is so supportive and resourceful that the only limitation for the student is herself. It was a great privilege working with Geoff, who is ingeniously creative and vastly knowledgeable. Thank you for all the lessons, support, and, most importantly, for believing in and encouraging me.

I'm also thankful for John Carpenter who opened for me the wonderful door of (sub)mm-wave interferometry and gave me a very first opportunity to work with ALMA data. John, you are my role model as a rigorous scientist who understands his field profoundly and is dedicated to getting things right. I would also like to thank Colette Salyk for being such a great mentor and a supportive friend during my years in graduate school. Thanks for taking me to the summit of Mauna Kea and beautiful Charlottesville.

The contributions of many wonderful collaborators are presented in this thesis. I'm particularly thankful for Klaus Pontoppidan and Andrea Isella, who kindly let me use their codes and always provided perceptive and critical comments on my manuscripts and proposals. A big thank you goes to Nate Crockett for many beneficial discussions and for his tremendous help during my job applications over the past several months.

I thank my thesis and candidacy defense committee: Geoffrey Blake, John Carpenter, Lynne Hillenbrand, Nick Scoville, and Dave Stevenson, for their time and

effort in my development as an independent scholar.

I thank my fellow graduate students for enriching my life at Caltech immeasurably. I'm thankful for students in the Blake group: Alex Lockwood, Masha Kleshcheva, Katie Kaufman, Danielle Piskorz, Dana Anderson, Brett McGuire, Brandon Carroll, Ian Finneran, and Marco Allodi. It was a great pleasure to work with you all and be your friend. Your company and laugher have turned many long nights in the remote observing room into fun and interesting times together. I'm grateful to my great class mates Kunal Mooley and Matt Schenker. Thank you for all the fun times in our first-year office, which made the stressful first-year transition into graduate school far more manageable. This was made all the easier thanks to the great atmosphere among the graduate students in both the Astronomy and Planetary Science options. Thank you all, especially Laura Pérez, Shriharsh Tendulkar, Ryan Trainor, Swarnima Manohar, Jackie Villadsen, Sebastian Pineda, Gwen Rudie, Allison Strom, Xi Zhang, Miki Nakajima, Chen Li, Zhan Su, Qiong Zhang, and Da Yang. A special thank you goes to Xuan Zhang, my best friend at Caltech, for very many happy lunches together and for sharing happiness, sorrow, and a belief in life and its joys.

I am very grateful to my parents, for letting their only daughter pursue her goals and dreams in a foreign land and culture, seven thousand miles away from them. Finally, I would like to thank my husband Shen Li for all his love and encouragement. I'm so grateful that I met you and I cannot imagine another life without you. I love you.

# Abstract

Planets are assembled from the gas, dust, and ice in the accretion disks that encircle young stars. Ices of chemical compounds with low condensation temperatures (<200 K), the so-called *volatiles*, dominate the solid mass reservoir from which planetesimals are formed and are thus available to build the protoplanetary cores of gas/ice giant planets. It has long been thought that the regions near the condensation fronts of volatiles are preferential birth sites of planets. Moreover, the main volatiles in disks are also the main C-and O-containing species in (exo)planetary atmospheres. Understanding the distribution of volatiles in disks and their role in planet-formation processes is therefore of great interest.

This thesis addresses two fundamental questions concerning the nature of volatiles in planet-forming disks: (1) how are volatiles distributed throughout a disk, and (2) how can we use volatiles to probe planet-forming processes in disks? We tackle the first question in two complementary ways. We have developed a novel super-resolution method to constrain the radial distribution of volatiles throughout a disk by combining multi-wavelength spectra. Thanks to the ordered velocity and temperature profiles in disks, we find that detailed constraints can be derived even with spatially and spectrally unresolved data – provided a wide range of energy levels are sampled. We also employ high-spatial resolution interferometric images at (sub)mm frequencies using the Atacama Large Millimeter Array (ALMA) to directly measure the radial distribution of volatiles.

For the second question, we combine volatile gas emission measurements with those of the dust continuum emission or extinction to understand dust growth mechanisms in disks and disk instabilities at planet-forming distances from the central

star. Our observations and models support the idea that the water vapor can be concentrated in regions near its condensation front at certain evolutionary stages in the lifetime of protoplanetary disks, and that fast pebble growth is likely to occur near the condensation fronts of various volatile species.

# Contents

**Acknowledgements** **iii**

**Abstract** **v**

**1 Introduction** **1**

1.0.1 Protoplanetary disks . . . . . 2

1.0.2 Volatiles in planet formation . . . . . 6

1.0.3 Observations of volatile in prototplanetary disks . . . . . 8

1.0.4 Thesis Outline . . . . . 8

**2 Evidence for a Snow Line Beyond the Transitional Radius in the TW Hya Protoplanetary Disk** **11**

2.1 Abstract . . . . . 12

2.2 Introduction . . . . . 13

2.3 Data reduction . . . . . 16

2.4 The TW Hya disk structure . . . . . 17

2.4.1 The dust temperature and density structure . . . . . 19

2.4.2 The gas density and temperature . . . . . 21

2.5 Retrieving the radial water vapor profile . . . . . 25

2.5.1 The water line model . . . . . 25

2.5.2 Best-fitting model . . . . . 28

2.5.2.1 The inner disk . . . . . 28

2.5.2.2 The transition region and the snow line . . . . . 32

2.5.2.3 The outer disk . . . . . 33

2.6 Discussion . . . 34
2.6.1 The origin of the surface water vapor . . . 35
2.6.2 The water vapor abundance distribution in transitional disks . 37
2.6.3 Molecular mapping with multi-wavelength spectra . . . 39
2.7 Conclusions . . . 43

**3 Comparison of the dust and gas radial structure in the transition disk [PZ99] J160421.7-213028 44**
3.1 Abstract . . . 45
3.2 Introduction . . . 46
3.3 Observations . . . 48
3.4 Results . . . 49
3.5 Modeling Analysis . . . 51
3.5.1 Dust emission: model description . . . 52
3.5.2 Dust emission: fitting procedure and results . . . 53
3.5.3 CO emission: model description . . . 57
3.5.4 CO emission: fitting procedure and results . . . 58
3.5.5 Uncertainties from the choice of $\gamma$ . . . 59
3.6 Discussion . . . 60
3.6.1 Comparing J1604-2130 with other transition disks . . . 60
3.6.2 Formation of the J1604-2130 transition disk . . . 61
3.6.3 Pressure trap and evolution . . . 64
3.6.4 Dust inside the cavity . . . 65
3.6.5 Outer disk radius . . . 65
3.7 Summary . . . 66
3.8 Acknowledgments . . . 67

**4 Dimming and CO absorption toward the AA Tau protoplanetary disk: An infalling flow caused by disk instability? 75**
4.1 Abstract . . . 76
4.2 Introduction . . . 77

4.3 Observations . . . . . 78
4.4 Results . . . . . 80
4.4.1 The physical properties of the absorbing gas . . . . . 81
4.5 The origin of the absorbing gas . . . . . 84
4.6 Acknowledgments . . . . . 88

**5 Evidence of fast pebble growth near condensation fronts in the HL Tau protoplanetary disk 93**
5.1 Abstract . . . . . 94
5.2 Introduction . . . . . 95
5.3 Observations . . . . . 96
5.4 Charactering the emission dips . . . . . 97
5.5 Condensation fronts of major volatiles in protoplanetary disks . . . . 98
5.6 Dust properties inside the dips . . . . . 101
5.7 Discussion . . . . . 104
5.8 Acknowledgement . . . . . 105

**6 Conclusions and Future Directions 109**
6.1 Summary of this thesis . . . . . 109
6.2 Future directions . . . . . 111
6.2.1 Opportunities from ALMA . . . . . 111
6.2.2 Combining multi-wavelength observations . . . . . 112

# List of Figures


1.1 The current theoretical framework for the formation of a low-mass star such as the Sun . . . . . 3

1.2 Physical and chemical structure of a protoplanetary disk . . . . . 5

1.3 *Spitzer* IRS data on volatile molecule emission in protoplanetary disks 9

2.1 The Spitzer IRS spectrum of TW Hya . . . . . 18

2.2 SED fit and disk structure of TW Hya . . . . . 20

2.3 Model CO rovibrational fluxes of the TW Hya disk . . . . . 23

2.4 The best-fit radial abundance of water vapor in TW Hya . . . . . 29

2.5 Detailed comparisons of the *Spitzer* IRS spectrumwith RADLite LTE water models . . . . . 30

2.6 The sensitivity of selected water line fluxes to variations in the water vapor column density distribution . . . . . 31

2.7 Constraints on the sharpness of the snow-line in TW Hya . . . . . 34

2.8 The $\chi^2$ surface for LTE slab model water fits for TW Hya as a function of $N$ and $T$ . . . . . 37

2.9 The radial and vertical locations bounding water vapor emission from the TW Hya disk . . . . . 42

3.1 880 $\mu$m continuum map of J1604-2130 . . . . . 68

3.2 ALMA observations of CO $J$ = 3-2 emission from J1604-2130 . . . . . 69

3.3 Dust surface density model of J1604-2130 . . . . . 70

3.4 Spectral energy distribution and model for J1604-2130 . . . . . 71

3.5 Comparison of the ALMA 880 $\mu$m continuum image with the synthetic model . . . . . 72
3.6 CO model for J1604-2130 . . . . . 72
3.7 Models with different $\gamma$ . . . . . 73
3.8 ComparingJ1604-2130 with other transition disks . . . . . 74

4.1 $V$-band photometry time series of AA Tau . . . . . 89
4.2 CO $M$-band spectra of AA Tau before and after the 2011 $V$-band dimming 90
4.3 Time variation in the low-$J$ $^{12}$CO and $^{13}$CO line shape(s) . . . . . 91
4.4 Model of the $^{12}$CO and $^{13}$CO absorption components in January 2013 . 92

5.1 Normalized radial surface brightness distributions of HL Tau at 0.87 (blue), 1.3 (red), and 2.9 mm (black) . . . . . 106
5.2 The expected condensation fronts in the disk mid-plane of HL Tau . . 107
5.3 Crosscuts of the spectral index in the HL Tau disk . . . . . 108

6.1 ALMA SV image of the HL Tau protoplanetary disk . . . . . 113

# List of Tables

2.1 Disk parameters for the dust model . . . . . 21
2.2 Observed and calculated water line fluxes . . . . . 27
2.3 Volatile line tracers at different disk radii . . . . . 42

3.1 Disk parameters . . . . . 56
3.2 Continuum model parameters for different $\gamma$ . . . . . 60

4.1 AA Tau Observation Log . . . . . 80

5.1 Parameters of the dips, normalized to the local continuum . . . . . 98
5.2 Condensation temperatures of the major volatiles in disks . . . . . 100

# Chapter 1

# Introduction

How did we get here? Are we alone in the Universe? Humankind has been seeking answers to these two enduring questions since ancient times. The answers to both questions demand an understanding of the formation of our own Solar system as well as the planetary systems around other stars.

We are privileged to be at a juncture where giant steps forward are being made in our understanding of planet formation. Over the past decade, more than three thousand planet candidates around other stars have been identified, indicating planet formation is a ubiquitous process in the local Universe. It is, however, striking to have discovered that most of the planetary systems around nearby stars show properties wholly distinct from our Solar system. What drives the large diversity observed? Might there be life in other planetary systems that are clearly so different from our own? There are two principal approaches to be taken in seeking further answers. One avenue involves the study of mature planetary systems around other stars, much as we have been doing for the Solar system. The architecture and chemical composition of a planetary system provides rich information on how it was formed. On the other hand, since planet formation is ubiquitous, we can also take advantage of nearby forming planetary systems to characterize the birth environments of planets directly, and use our knowledge of physics and chemistry to decipher the ongoing processes of planet formation.

The second approach is adopted in this thesis. Planets are formed in disks of gas and dust rotating around young stars. The physical and chemical structure of these

disks largely regulates the final outcome of planetary system formation. Over the past decade, significant advances have been made in characterizing many basic properties of these disks, including the dust mass in disks and the disk evolutionary timescale(s). One of the most basic properties of disks, that of its chemical composition, is still largely unknown, however. Indeed, a rocky planet at the 'right' orbital distance may not be a habitable one, because it also must retain sufficient liquid water and critical elements such as carbon and nitrogen to form life.

Thus, we want to know the distribution of essential living-giving materials, or volatiles, such as water, $CO/CO_2$ and $NH_3$, in disks, before planetary surfaces are assembled. In particular, this thesis will focus recent steps toward understanding the distribution of volatiles in planet-forming disks, and seeks to answer questions such as: how are volatiles distributed in the disks? How does the general evolution of disks change their distribution? This brief introductory chapter is organized as follows: protoplanetary disks, in the context of star and planet formation, are defined and discussed in Section 1.0.1. I then introduce the definition of volatiles and discuss the important role that they play in planet formation processes in Section 1.0.2. I next describe current observations of volatiles in disks (Section 1.0.3), and conclude with an outline of the main chapters in this thesis.

### 1.0.1 Protoplanetary disks

Stars are formed from the interstellar medium through the collapse of matter inside the dense cores of molecular clouds. An *accretion disk* is developed during the process because the collapsing gas (principally $H_2$+He) has too much angular momentum to collapse directly to center of the core. Conventionally, Young Stellar Objects (YSO) are grouped into Class 0, I, II, and III objects empirically based on the infrared (and far-infrared) slope of their Spectral Energy Distribution (SED), which measures the distribution of flux as a function of wavelength (Lada & Wilking, 1984). This classification has later been given physical meaning thorough modeling of each stage in the process (Adams et al., 1987), see Figure 1.1.

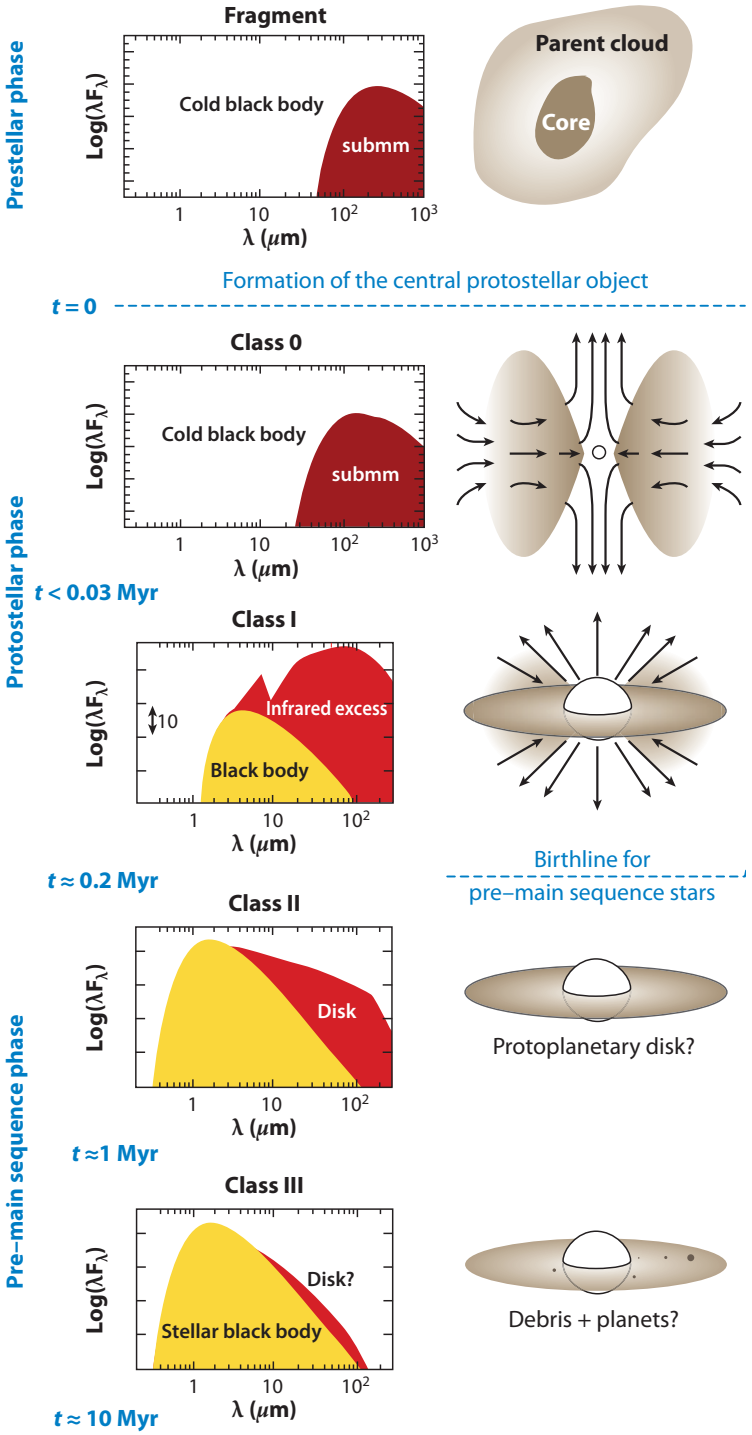


Figure 1.1 The current theoretical framework for the formation of a low-mass star (illustration adapted from Dauphas & Chaussidon 2011). The left column shows a canonical spectral energy distribution for each one of the stages that are shown. The right column presents an illustration of the main components that characterize each stage. From top to bottom: a fragment inside a molecular cloud experiences contraction under its own self gravity (top). Runaway growth ensues and a protostar is formed (Class 0 YSO). Angular momentum is conserved and a disk of material orbiting the star results, but the star+disk system is still surrounded by an envelope (Class I YSO). Once the envelope dissipates the central object becomes visible at optical wavelengths, with only a disk surrounding the pre-main sequence star (Class II YSO). Finally, the disk is accreted but collisions between macroscopic bodies may create a debris disk (Class III YSO).

The earliest stages of cloud collapse is represented by the so-called Class 0 objects – systems so deeply embedded within optically thick gas and dust that they are not visible even in deep near-IR rimages. At this stage, a rotationally supported disk may have been formed, but high angular resolutions observations are still sufficiently rare that our characterization the properties of the disks in this stage is poor. Unlike Class 0 objects, a rotational signature of a disk can easily be detected in Class I objects, which still have an envelope of infalling material, and which are usually associated with strong outflows or jets. The transition from a Class 0 to Class I object takes less than 0.5 Myr (Evans et al., 2009). As accretion proceeds, the envelope eventually dissipates ($\sim$1 Myr) and the central young star becomes optically visible, representing the start of the Class II phase. For low and medium mass stars($\lesssim 3\,M_{\odot}$), the gas disk is called a ***protoplanetary disk*** (Figure 1.2). These disks can last for a few million years (e.g., Haisch et al. 2001, Damjanov et al. 2007, Gutermuth et al. 2008), setting a critical limit for the timescale of the formation of gas giant planets. Once the gas disk has dissipated, the accretion onto the central star wanes and the flux excess at long-wavelengths decreases. A dusty debris disk of so-called 'second generation' dust (and small amounts of gas) can be formed via collisions between planetesimals (Class III).

This thesis focuses on the Class I and II stage, the two critical stages for the earliest steps in planet formation. It is mainly at these stages that (sub)micron-sized interstellar grains grow into planetesimals and planets. Because the core of a giant planet must grow massive enough to accrete gas before the primordial disk is dissipated, the lifetime of the gas disk sets a hard upper limit to the formation timescale of giant planets. Since planets are built from the materials in disks, the chemical reactions that occur during this stage will define the chemical composition of any future planetary system.

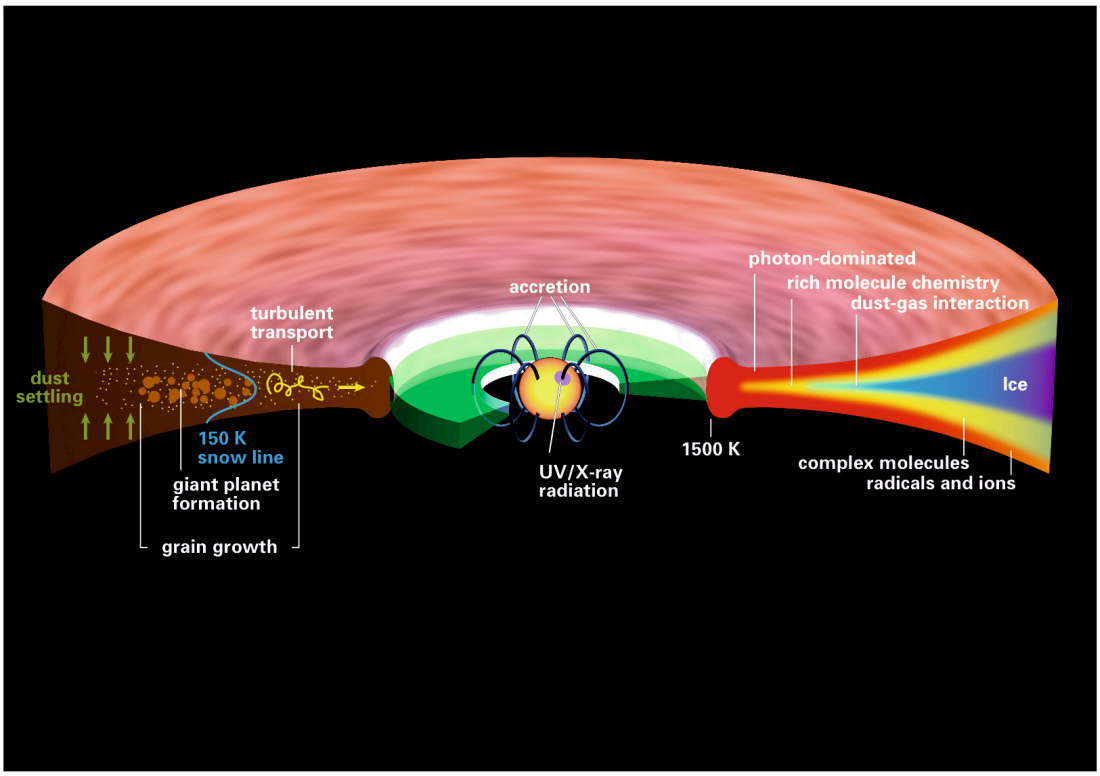


Figure 1.2 Sketch of the physical and chemical structure of a $\sim$1$-$5 Myr old protoplanetary disk around a Sun-like star, adapted from Henning & Semenov (2013).

### 1.0.2 Volatiles in planet formation

Volatiles are compounds with low sublimation temperatures (<200 K). In protoplanetary disks, these are usually small molecules that form the principle reservoirs of the abundant elements carbon, nitrogen, and oxygen. The most important examples include water, CO, and $N_2/NH_3$.

Volatiles, especially water, play an essential role in planet formation. They not only provide the major solid mass reservoir for planetesimal and planet formation at sufficiently low temperatures, but also set the initial chemical composition in the atmospheres of forming planets.

Recent studies have also suggested that volatiles can greatly accelerate the formation of planetesimals, from which planets are built. Planetesimals are usually defined as solid bodies that are held together by self-gravity rather than material strength (minimum size 100-1000 meters, Benz 2000). The growth from (sub)micron-sized ISM grains to planetesimals is a difficult process in protoplanetary disks, because once the grains grow into millimeter or larger size, the strong gas drag in a disk will cause solid bodies to collide destructively or they are dragged radially into the central star before they can grow into planetesimals. Volatiles can accelerate the growth process primarily via two routes: (i) condensed volatiles can add a large amount of solid material that is available for planetesimal formation; and (ii) the icy mantle formed by condensed volatiles on dust grains can greatly enhance their 'stickiness' in binary collisions.

The initial distribution of volatiles in a protoplanetary disk thus determines the chemical composition of planetesimals, which will later contribute to the bulk chemical composition of planets. Asteroids, meteorites and comets are believed to be the remnants of Solar system planetesimals that are either primitive or have that undergone dynamical and chemical processes. Nevertheless, these objects are our best window into the volatile composition of the Solar protoplanetary disk.

In core accretion planet formation theories, the regions just beyond the condensation fronts of most abundant volatiles are optimal locations for building giant planet

cores. In our Solar system, the terrestrial planets are all in the inner region while the gas and ice giants are located at further distances from the Sun. This architecture is attributed to the dividing line provided by the water condensation front, or *snow line*, where most of the locally available water vapor condenses as solid ice. The condensed water ice can directly increase the surface density of solids beyond the snow line by factors of a few (between 2-4, depending on the elemental ratios adopted). Furthermore, the competition between the inward migration of icy grains and the outward diffusion of water vapor can enhance the local surface density just beyond the snow line by much larger factors (up to $\sim$75, Stevenson & Lunine 1988). As was mentioned above, the enhanced surface density can significantly accelerate the formation of planetesimals and planetary cores. The regulation of other condensation fronts is probably less significant than the water snowline, but it has been suggested that many properties of Neptune and Uranus can be accounted for if they formed just beyond the CO condensation line in the Solar protoplanetary disk (Ali-Dib et al., 2014).

Besides accelerating the formation of giant planets, volatiles also set the initial chemical composition in the atmosphere of giant planets. For example, one important parameter of planetary atmospheres is the elemental C/O ratio, determining whether a carbon-dominated or oxygen-dominated chemistry is manifest. Due to the preferable condensation of oxygen carriers over some regions of the disk (outside the water sonwline but inside the CO snow line), the C/O ratio in disk gas can be higher than the that of the central star. If a giant planet forms via core accretion from solids followed by the accretion of a gaseous envelope, it will inherit the high C/O ratio in its atmosphere (Öberg et al., 2011).

At smaller distances from the young star, volatiles are crucial components to the creation of habitable planets. It is still under debate where the water in the Earth's oceans originated, since terrestrial planets are thought to be assembled from dust in the innermost regions of the disk where volatiles are relatively depleted. The leading theories suggest that water was deposited on the near-surface of the early Earth through bombardment by asteroids and comets which were formed at disk radii beyond the snow line.

### 1.0.3 Observations of volatile in prototplanetary disks

For many years, the Solar system provided our only case study of planet formation. Direct sampling or spectroscopic observations of planets, meteorites, and comets provided key information on the chemical composition of materials formed in the primordial Solar Nebula and retained in the current planetary system. It is found that the C, N, and O elemental abundances increase with the distance from the Sun and that the terrestrial planets have the largest depletion. Since the majority of the C, N, and O elements are in volatiles, this trend is also that of volatile depletion. As noted above, the distribution of terrestrial planets inside of 3 AU and massive gas/ice giant planets orbiting beyond this radius has long been thought to be related to the presence of a water ice condensation front.

The last decade brought several breakthroughs in the observations of volatiles within protoplanetary disks. Thanks to great sensitivity of the *Spitzer* Space Telescope and Infrared ground-based facilities on 8-10m telescopes, for example, simple volatiles have now been detected in a large number of protoplanetary disks, including water, CO, $C_2H_2$, HCN, and $CO_2$ (Carr & Najita, 2008; Pontoppidan et al., 2010b; Salyk et al., 2011), see Figure 1.3. Modeling shows that these emission bands originate from the warm inner region of protoplanetary disks (that is, distances out to a few AU). In the far-IR wavelength range, the *Herschel* Space Telescope has detected water vapor emission in a few protoplanetary disks (Hogerheijde et al., 2011). At (sub)mm wavelengths, ALMA is rapidly expanding our understanding of volatiles in disks (e.g., Qi et al. 2013, Öberg et al. 2015) .

### 1.0.4 Thesis Outline

In this thesis, I aim to observationally constrain the distribution of volatiles in protoplanetary disks by employing multi-wavelength spectroscopic observations, high spatial resolution interferometric imaging, and long-term spectroscopic monitoring. By studying the distribution of volatiles in planet-forming disks, we constrain the initial conditions for planetesimal and planet formation. The structure of this thesis

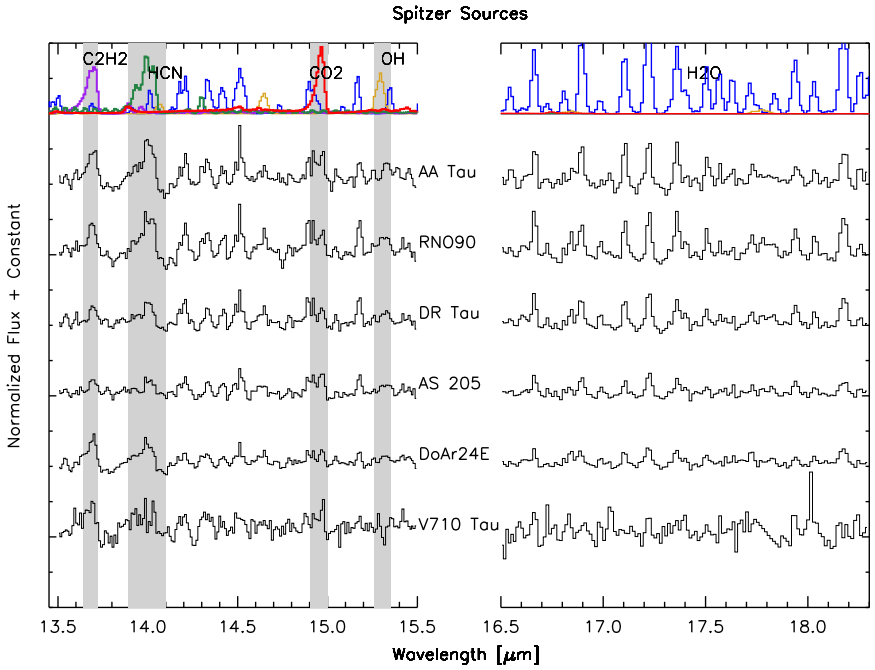


Figure 1.3 *Spitzer* IRS data on volatile molecule emission in protoplanetary disks. The spectra on the top row are synthetic models for different molecules: Water (blue), HCN (green), $C_2H_2$ (purple), $CO_2$ (red), and OH (Orange).

is as follows:

In Chapter 2, I discuss the use of multi-wavelength water emission spectra from the mid- to far-IR to constrain the location of the water snowline in the gas-rich protoplanetary disk around TW Hya. This is the first observational constraint on the location of snow line in a protoplanetary disk.

In Chapter 3, I present high spatial resolution interferometry observations of the dust and several volatile molecules in the so-called transition disk around the young star J1604-2130 in the Upper Sco-Cen association. I explain in detail how these observations show that the distribution of dust and gas can be shaped quite differently when the disk undergoes significant structural evolution, likely as the result of planet formation.

In Chapter 4, I present the analysis of near-IR spectroscopic mentoring of the highly inclined protoplanetary disk surrounding the classical T Tauri star AA Tau, which showed a sudden dimming in its optical photometry after maintaining a nearly constant luminosity for more than two decades. I demonstrate that the photometric variation and CO line shape changes associated with AA Tau possibly arise from a disk instability/outburst, which powers material transport from large scale heights in the outer disk toward the inner disk region.

In Chapter 5, I analyze ALMA (sub)mm long baseline Science Verification continuum images of the young star HL Tau, which shows a mysterious suite of dark rings. I show that the most prominent rings are remarkably close to the expected condensation fronts of major volatiles in the mid-plane of the disk, and that the dust emissivity changes between 1.3 and 0.877 mm wavelengths are consistent with dust growth into decimeter size scales inside the dips. These observations suggest that fast pebble growth is likely to be driven around the condensation fronts of abundant volatiles.

In Chapter 6, I summarize the findings of this thesis and discuss future prospects in the study of volatiles within protoplanetary disks.

# Chapter 2

# Evidence for a Snow Line Beyond the Transitional Radius in the TW Hya Protoplanetary Disk

Ke Zhang[1], Klaus M. Pontoppidan[2], Colette Salyk[3], Geoffrey A. Blake[4]

1. Division of Physics, Mathematics & Astronomy, MC 249-17, California Institute of Technology, Pasadena, CA 91125, USA; kzhang@astro.caltech.edu

2. Space Telescope Science Institute, Baltimore, MD 21218, USA

3. National Optical Astronomy Observatory, 950 N. Cherry Ave., Tucson, AZ 85719, USA

4. Division of Geological & Planetary Sciences, MC 150-21, California Institute of Technology, Pasadena, CA 91125, USA

*Keywords:* planetary systems: protoplanetary disks — astrochemistry — stars: individual (TW Hya)

This chapter, with minor differences, was published in its entirety under the same title in *The Astrophysical Journal*, 2013, Volume 766, pp. 82-92.

## 2.1 Abstract

We present an observational reconstruction of the radial water vapor content near the surface of the TW Hya transitional protoplanetary disk, and report the first localization of the snow line during this phase of disk evolution. The observations are comprised of *Spitzer*-IRS, *Herschel*-PACS, and *Herschel*-HIFI archival spectra. The abundance structure is retrieved by fitting a two-dimensional disk model to the available star+disk photometry and all observed $H_2O$ lines, using a simple step-function parameterization of the water vapor content near the disk surface. We find that water vapor is abundant ($\sim 10^{-4}$ per $H_2$) in a narrow ring, located at the disk transition radius some 4 AU from the central star, but drops rapidly by several orders of magnitude beyond 4.2 AU over a scale length of no more than 0.5 AU. The inner disk (0.5-4 AU) is also dry, with an upper limit on the vertically averaged water abundance of $10^{-6}$ per $H_2$. The water vapor peak occurs at a radius significantly more distant than that expected for a passive continuous disk around a 0.6 $M_\odot$ star, representing a volatile distribution in the TW Hya disk that bears strong similarities to that of the solar system. This is observational evidence for a snow line that moves outward with time in passive disks, with a dry inner disk that results either from gas giant formation or gas dissipation and a significant ice reservoir at large radii. The amount of water present near the snow line is sufficient to potentially catalyze the (further) formation of planetesimals and planets at distances beyond a few AU.

## 2.2 Introduction

Giant planets and planetesimals form in the chemically and dynamically active environments in the inner zone of gas-rich protoplanetary disks (Pollack et al., 1996; Armitage, 2011). Processes taking place during this critical stage in planetary evolution determine many of the parameters of the final planetary system, including the mass distribution of giant planets, as well as the chemical composition of terrestrial planets and moons.

Indeed, some of the most important features of mature planetary systems may be dictated by the behavior of the water content of protoplanetary disks. Such processes include the formation of a strong radial dependence of the ice abundance in planetesimals – the *snow line* (Hayashi, 1981). The deficit of condensible water inside the snow line leads to a need for radial mixing of icy bodies during the later gas-poor stages in the evolution of the planetary system, in particular to explain the existence of water on the Earth (Raymond et al., 2004). Ice mantles on dust beyond the snow line allow grains to stick at higher collisional velocities, allowing for efficient coagulation well beyond the limits of refractory grain growth alone (Blum & Wurm, 2008). The combined mass of the solid component in protoplanetary disks is likely dominated by volatile, but condensible, species, the most abundant of which is water (Lecar et al., 2006).

Thus, core accretion models that rely on the availability of large concentrations of solid material suggest that giant planets will initially be found beyond the snow line, as their formation requires the existence of a massive ice reservoir (Kennedy & Kenyon, 2008; Dodson-Robinson et al., 2009). The added solid density offered by condensible water may also offer a way out of the "meter-barrier" for planetesimal formation (Weidenschilling, 1997), in which centimeter to meter size icy bodies migrate inwards and are lost to the central star on time scales much shorter than those of steady state grain aggregation (Birnstiel et al., 2009): beyond a certain mass density of solids, local concentrations of boulder-sized particles may overcome the effects of turbulence acting to disperse them and will gravitationally contract to form Ceres-mass planetesimals

(Johansen et al., 2007, 2009).

Given the central role that water plays in the formation of planetary systems, its distribution and abundance in protoplanetary disks has been the subject of intense theoretical study (e.g., Ciesla & Cuzzi, 2006; Garaud & Lin, 2007; Kretke & Lin, 2007). Yet, the only source of observational constraints on the initial radial distribution of water in planet-forming regions has been the distribution of ice in the current Solar System (Hayashi, 1981), the remaining bodies of which represent only a small part of the story. Apart from the fact that the solar system water distribution may be unique, theoretical study shows that the initial distribution of ices in protoplanetary disks evolves as does the disk temperature distribution (e.g. Garaud & Lin, 2007), and that in later stages it is confounded by the dynamical interactions between planets and the planetesimal swarm (Gomes et al., 2005). The final distribution of water in a planetary system is thus an obscured tracer of initial conditions, and to understand the role of water and other volatiles in the formation of planets, we should measure their distribution before, during, and after planet(esimal) formation.

The most direct way to trace the water abundance distribution in protoplanetary disks is to image line emission from water vapor. However, due to the strong radial gradient of gas temperature in disks, each line of a given excitation energy will only trace a limited areal extent of the disk. For instance, high-J rovibrational transitions in the mid-infrared waveband are sensitive to the warmer ($\gtrsim 300\,\mathrm{K}$) and inner parts of the disk surface ($\lesssim 10\,\mathrm{AU}$). Far-infrared transitions arise from cooler gas ($\lesssim 300\,\mathrm{K}$) in the outer ($\gtrsim 10\,\mathrm{AU}$) and deeperregions of the disk. In order to measure the total water vapor content in the disk surface, it is necessary to observe lines across states of widely varying excitation energies.

That line emission from water vapor is common in disks is now well established thanks to observations with the *Spitzer* IRS instrument, which has detected a forest of emission lines in the 10–35 $\mu$m range. Carr & Najita (2008) and Salyk et al. (2008) first reported a large number of rotational lines due to warm water in AA Tau, AS 205N, and DR Tau, while Pontoppidan et al. (2010b) report a water emission detection rate of $\sim$50% in their *Spitzer* survey of 46 disks surrounding late-type (M-

G) stars. With upper energy levels of $E_{up} \sim 1000 - 3000\,\mathrm{K}$, these water lines arise from the inner few AU region of the disks. Detailed radiative transfer models show that the surface water vapor abundance may need to be truncated beyond $\sim$1 AU for a typical classical T Tauri star (cTTs) disk in order to match the general line ratios over 10–35 $\mu$m (Meijerink et al., 2009). Follow-up ground-based spectra of the brightest targets have constrained the gas kinematics, and confirmed that the water vapor resides inside the snow-line (Pontoppidan et al., 2010a).

Recently, complementary spectral tracers of water vapor in the *outer* disk have become accessible via *Herschel* Space Observatory PACS and HIFI observations. Riviere-Marichalar et al. (2012) describe the discovery of warm water emission at 63.3 $\mu$m in 8 out of their 68 T Tauri disk sources, and tentative detections of water transitions with similar excitation energies have also been reported for the Herbig Ae/Be star HD 163296 (Meeus et al., 2012; Fedele et al., 2012). The first sensitive search for ground-state emission lines of cold water vapor in DM Tau indicated that the vertically averaged water vapor abundance in the outer disk of this source is extremely low, $< 10^{-10}$ per hydrogen molecule (Bergin et al., 2010). Finally, two ground state water emission lines in TW Hya were detected with HIFI (Hogerheijde et al., 2011). Again, the vertically averaged water vapor abundance is $\lesssim 10^{-10}$ per hydrogen, while the estimated peak water vapor abundance is closer to $\sim 10^{-8} - 10^{-7}$ in the near surface layers of the disk. These are values that can be produced by UV photodesorption from icy dust grains. In this interpretation, the low excitation water lines trace a large, but otherwise unseen, reservoir of ice in the outer disk.

Here we present an observationally-based method for reconstructing the water vapor column density profile in the surface of a protoplanetary disk, based on multi-wavelength, multi-instrument IR/submillimeter spectra, and apply the method to the TW Hya transitional disk. We chose TW Hya because of the availability of deep archival *Spitzer* and *Herschel* water spectroscopy and the existence of detailed structural models. Further, we report on the spectroscopic identification of warm water vapor emission at 20–35 $\mu$m, a detection that permits, in combination with the *Herschel* data, the first localization of the snow line in a transitional disk.

The outline of the paper is as follows: in Section 2.3, we describe the *Spitzer* and *Herschel* data. In §3.5.1, we describe the structural gas/dust model for the TW Hya disk. Section 2.5 applies a two-dimensional line radiative transfer model to the model disk structure to retrieve a radial abundance water profile based on the full spectroscopic dataset. The results are discussed in §4.4.

## 2.3 Data reduction

The *Spitzer* IRS 10−35 $\mu$m high resolution mode (R∼600) spectra of TW Hya were acquired as part of a survey program of transitional disks (PID 30300), with J. Najita as PI. The observations were done in two epochs using different background observation strategies, for an observation log see Najita et al. (2010). In the first epoch, TW Hya was observed on source (AOR 18017792), followed by north and south offset observations (AORs 18018048, 18018304). In the second epoch (AOR 24402944), TW Hya was observed using a fixed cluster-offsets mode, such that the background scans were observed in the same sequence. All of the datasets were extracted from the *Spitzer* archive and reduced using the Caltech High-resolution IRS Pipeline (CHIP) described in Pontoppidan et al. (2010b), which takes full advantage of the existence of redundant background observations. CHIP implements a data reduction scheme similar to that developed by Carr & Najita (2008).

In an extensive analysis of the 10-20 $\mu$m Short-Hi (SH) spectrum, Najita et al. (2010) report the detection of excited OH emission lines and a host of other molecular features from TW Hya, but no water emission above a lower flux limit of ∼10 mJy. As stressed by Najita et al. (2010), the lack of detectable water emission from the highly excited water lines below 20 $\mu$m does not preclude the presence of cooler water vapor, and in a follow-up paper (in prep), these authors interpret the SH and Long-Hi (LH) data together. Our independent reduction of the deep *Spitzer* IRS observations at longer wavelengths displays numerous water emission lines in the 20−35 $\mu$m LH module. The strongest transition at 33 $\mu$m can be clearly seen in all LH epochs. The spectrum from the fixed cluster-offsets AOR has the highest signal-to-noise ratio

(SNR), and our analysis is therefore based on this spectrum (presented in Figure 2.1). The SH spectrum is scaled by a factor of 1.25 to match the flux of LH spectrum and IRAS 12 $\mu$m photometry data.

The *Herschel* HIFI line fluxes for the ground state ortho and para water transitions are taken from Hogerheijde et al. (2011). Somewhat higher excitation lines are probed by the PACS instrument, and narrow-range line spectra of TW Hya from 63−180 $\mu$m were acquired as part of the public *Herschel* Science Demonstration Phase program (observation ID 1342187238). The PACS data were reduced using the *Herschel* interactive processing environment (HIPE v.6.0), up to level 2. After level 1 processing, spectra for the two nod positions were extracted separately from the central spaxel. The spectra of the two nod positions were uniformly rebinned, using an over-sampling factor of 2 and an up-sampling factor of 2, before co-adding to produce the final result. Linear baselines were fitted to the local continua and integrated line fluxes (see Table 2.2) were obtained using Gaussian fits. While no water emission is formally detected with PACS at $3\sigma$, there are indications of water lines consistent with our water abundance model predictions; see Section 2.5 for further discussion.

## 2.4 The TW Hya disk structure

The accuracy of retrieved chemical abundances in protoplanetary disks is coupled to how well the two- or three-dimensional gas kinetic temperature and volume density structures are known. Our model development consists of three stages: first, we construct an axisymmetric model of the dust component of the disk, based on fits to the continuum spectral energy distribution (SED), using the RADMC code(Dullemond & Dominik, 2004). We then assume that the gas density distribution follows that of the small dust grain population — a reasonable assumption, since the small grains carry most of the disk opacity and are dynamically well-coupled to the disk gas. However, we do allow thermal decoupling of the gas from the dust near the disk surface, in the form of a constant temperature offset constrained using the CO rovibrational emission spectrum near 4.7 $\mu$m. Finally, we constrain the water vapor radial column density

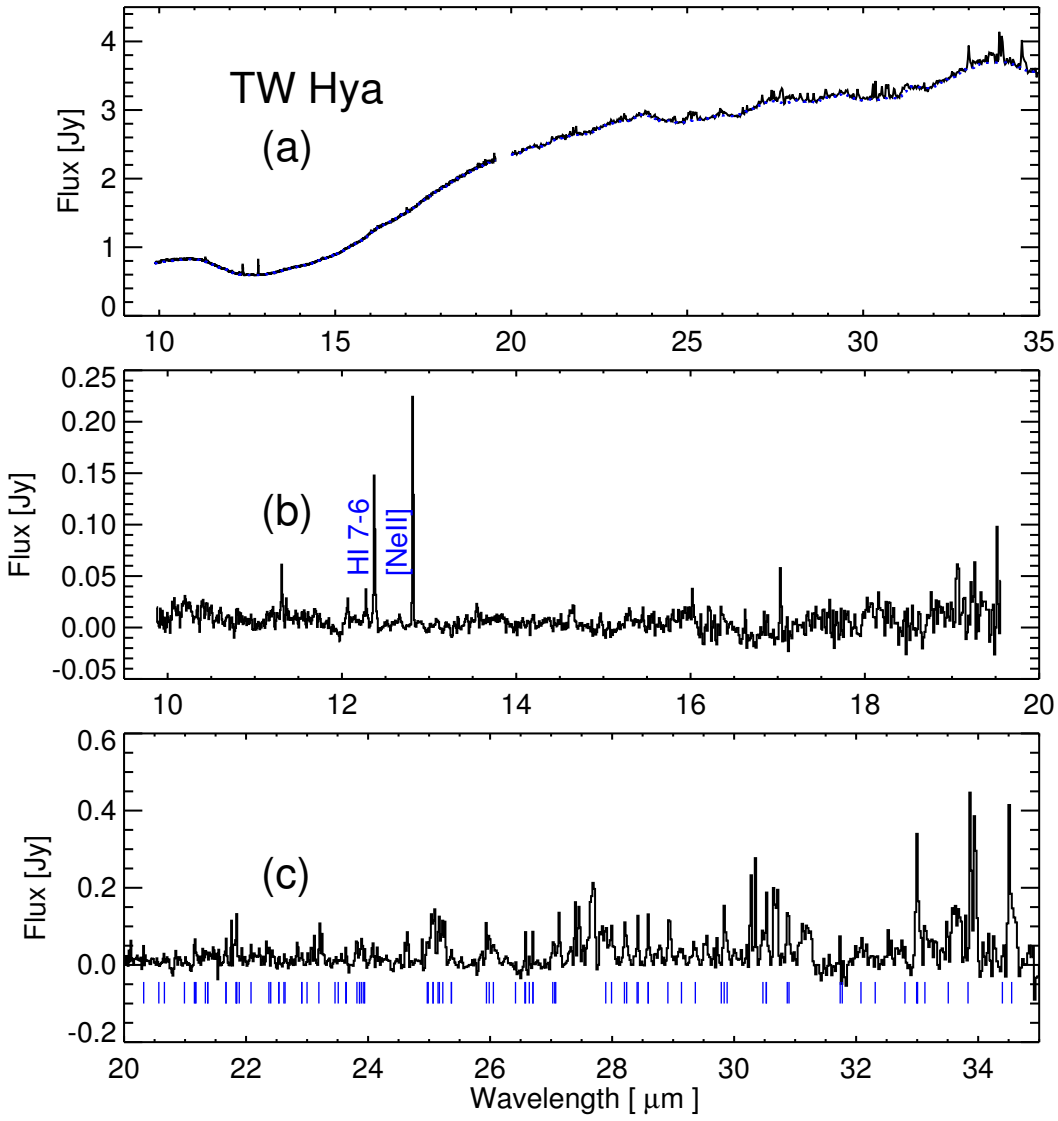


Figure 2.1 (a) The *Spitzer* IRS high resolution (R∼600) spectrum of TW Hya from 10-35 $\mu$m; (b) continuum subtracted spectrum between 10 and 20 $\mu$m; (c) continuum subtracted spectrum between 20 and 35 $\mu$m. No water emission is detected in the 10-20 $\mu$m SH modules (Najita et al., 2010), but the 20-35 $\mu$m LH spectrum shows clear evidence for water vapor. The short vertical ticks indicate water vapor rest wavelengths (HITRAN 2008 database) for lines with intensities $>5\times10^{-22}$ cm$^{-1}$/(molecule cm$^{-2}$).

distribution (and thus abundance) at all disk radii via fits to the multi-wavelength water spectra acquired for TW Hya.

### 2.4.1 The dust temperature and density structure

Dust, as the dominant source of disk continuum opacity, determines the disk SED shape. At a distance of only $\sim 51 \pm 4\,\mathrm{pc}$ (Mamajek, 2005), TW Hya is one of the best studied protoplanetary disks, with extensive photometric data available from UV to cm wavelengths. Calvet et al. (2002) developed a physically self-consistent dust structure model for TW Hya. They found that the disk is vertically optically thin within 4 AU, corresponding to a depletion of small dust grains by orders of magnitude at these radii. This inner zone of dust depletion has been confirmed by subsequent observations (Eisner et al., 2006; Hughes et al., 2007). A small amount of dust in the inner disk is needed to explain the 10–25 $\mu$m amorphous silicate features (Calvet et al., 2002), and accretion onto the star continues. The existence of hot gas in the innermost disk has been further confirmed by the detection of CO $\Delta v$=1 rovibrational emission near 4.7 $\mu$m (Rettig et al., 2004; Salyk et al., 2007, 2009) and via Spectro-Astrometric (SA) observations of these same lines (Pontoppidan et al., 2008). It is not yet clear whether the gas content has been depleted to the same degree as the dust in the inner disk, although Gorti et al. (2011) estimated enhancements of 5-50 in gas/dust in in the inner disk.

We adopt $\mathrm{M}_\star = 0.6\,\mathrm{M}_\odot$, $\mathrm{R} = 1\,\mathrm{R}_\odot$ and $\mathrm{T}_{\mathrm{eff}} = 4000\,\mathrm{K}$ for the stellar mass, stellar radius and effective temperature (Webb et al., 1999). The inclination angle of the disk axis to the line-of-sight is fixed to $i = 7°$ (Qi et al., 2004). The standard gas-to-dust ratio of 100 is used to estimate the total disk mass.

The dust structure model adopted is similar to Andrews et al. (2012): an optically thin inner disk between the sublimation radius ($r_{\mathrm{sub}}$) and the cavity edge ($r_{\mathrm{cav}}$), a cavity "wall" and an optically thick disk. The cavity "wall" component is needed to reproduce the spectral shape of TW Hya from $10-30\,\mu$m (Uchida et al., 2004). The sublimation radius was set to $r_{\mathrm{sub}} = 0.055\,\mathrm{AU}$, which is the location where dust

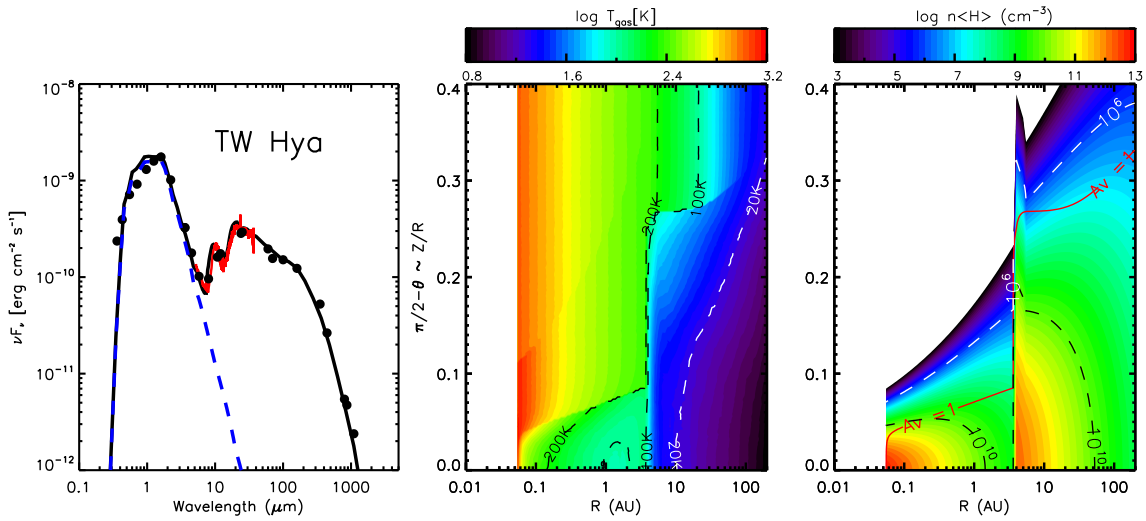


Figure 2.2 Left panel: A 2-D model fit to the TW Hya SED using RADMC and the parameters in Table 2.1. The stellar spectrum (peaking near 1 $\mu$m) is generated from a Kurucz model with $T_{\rm eff}$ = 4000 K. The photometric points are taken from Rucinski & Krautter (1983), 2MASS, Low et al. (2005), and Weintraub et al. (1989), while the 5–35 $\mu$m *Spitzer* IRS spectrum is that displayed in Figure 2.1. Middle panel: Fiducial gas temperature profile. Right panel: Fiducial gas density profile, with the $A_v$=1 height depicted by the solid line.

temperature reaches 1400 K. The cavity radius is fixed as $r_{\rm cav} = 4$ AU, in accord with previous near-IR interferometry (Eisner et al., 2006; Hughes et al., 2007; Akeson et al., 2011). We adopt the power-law density profile of Andrews et al. (2012) for the outer disk, which is based on 870 $\mu$m continuum interferometric imaging. A summary of the dust structure model parameters can be seen in Table 1.

Following Pollack et al. (1994) and D'Alessio et al. (2001), we use a dust mixture of astronomical silicates, organics, and water ice. For the optically thin inner disk, pure glassy silicate is used to match the strong silicate bands at 10 and 18 $\mu$m. The dust size distribution is taken to be $n(a) \propto a^{-s}$ with $s = 3.5$ between $a_{\rm min} = 0.9$ and $a_{\rm max} = 2.0$ $\mu$m (Calvet et al., 2002). In the cavity wall, we use a dust size range between 0.005 and 1 $\mu$m; outside the cavity wall, 95% (by mass) of the dust has a size distribution extending from 0.005 $\mu$m to 1 mm, with the remaining 5% contained in grains from 0.005 – 1 $\mu$m. Total dust masses in the optically thin and thick parts of the disk are $2.77 \times 10^{-9}$ and $4.4 \times 10^{-4}$ $M_\odot$. The SED fit and our fiducial gas

Table 2.1. Disk parameters for the dust model

| Parameter | Inner disk | Cavity wall | Outer disk |
|---|---|---|---|
| $r$ (AU) | 0.055 − 4 | 4 −5 | 5−196 |
| $p$ | 0.8 | 0.0 | 1.0 |
| $\gamma$ | 0.3 | -0.25 | 0.2 |

Note. — Here $\gamma$ is the index that describes the vertical scale height $z_d$: $z_d = z_0(r/r_0)^{1+\gamma}$ where $z_0$ = 0.7 at $r_0$ = 10 AU; $p$ is the index of the surface density distribution: $\Sigma_d = \Sigma_0(r/r_0)^{-p}$.

temperature and density profiles, discussed further below, are presented in Figure 2.2.

### 2.4.2 The gas density and temperature

The gas/dust ratio in disks evolves due to grain growth and transport processes (Birnstiel et al., 2009), and likely has significant radial and vertical structure. For simplicity, the gas density is here assumed to follow that of the dust, with a constant gas/dust mass ratio throughout the disk. For TW Hya, the estimated global gas/dust ratio varies from 2.6 to 100 (Thi et al., 2010; Gorti et al., 2011). The recent detection of the HD J = 1-0 line from TW Hya has offered an independent and robust estimation of the gas mass (Bergin et al., 2013), which indicates a globally averaged gas/dust ratio close to 100, a value we adopt here. Significant dust vertical settling will produce an enhanced gas-to-dust ratio in the upper layers of the disk. Such settling should have little impact on the longest wavelength water transitions studied here, or on the strongest, optically thick lines traced by the Spitzer IRS. By creating a larger column of gas above the $\tau_{dust} = 1$ surface, the absolute fractional abundance of water derived by a well mixed LTE model likely provides an upper bound, but the inferred radial *structure* in the water vapor column density should be fairly robust against changes

to the dust distribution.

Above a certain altitude in the disk, where the environment becomes exposed to the ambient radiation field, the gas can also be thermally decoupled from the dust. The gas will adopt a temperature profile that is a balance among heating processes, such as mechanical heating via accretion or that driven by photodissociation or the photoelectric electric effect, and cooling rates driven by atomic, molecular, and dust grain emission (Glassgold et al., 2004; Kamp & Dullemond, 2004). General gas temperature profiles can be estimated using detailed thermo-chemical models (e.g. Woitke et al., 2009; Najita et al., 2011). However, such profiles can be highly dependent on input assumptions, and interdependencies between model parameters and observables can be obscure. Here, we simplify the process by deriving the vertical gas temperature structure in the inner disks using the rotational ladder from M-band CO P-branch $v = 1 - 0$ emission lines. Due to its (photo)chemical robustness, the abundance of CO is predicted to be fairly constant at $n_{CO}/n_{H_2} \approx 1.2 \times 10^{-4}$ in regions warmer than 20 K (Aikawa et al., 1996). A high CO abundance is expected to persist even for a depleted inner disk, such as that of TW Hya. Indeed, in the chemical model of Najita et al. (2011), the abundance of CO rises to $\sim 10^{-4}$ once the vertical column density of $H_2$ reaches $10^{21}$ cm$^{-2}$ for radii beyond 0.25 AU (physical densities are $>10^9$ cm$^{-3}$).

Since the heating of the inner disk gas is driven by X-ray and FUV photons from the central star and stellar accretion flow (Kamp & Dullemond, 2004; Gorti et al., 2011), we assume that gas and dust temperature become decoupled in regions where the radial optical depth for visible photons is less than unity. That is,

$$T_{\rm gas} = \begin{cases} T_d, & A_v > 1 \\ T_d + \delta T, & A_v \leqslant 1 \end{cases} , \tag{2.1}$$

where $T_d$ is dust temperature in the disk at (r, $\theta$) in spherical coordinates, $A_v$ is the visual extinction along the radial direction $\theta$, and $\delta$T is a free parameter that describes the gas-dust temperature difference, to be determined through fits to observational data.

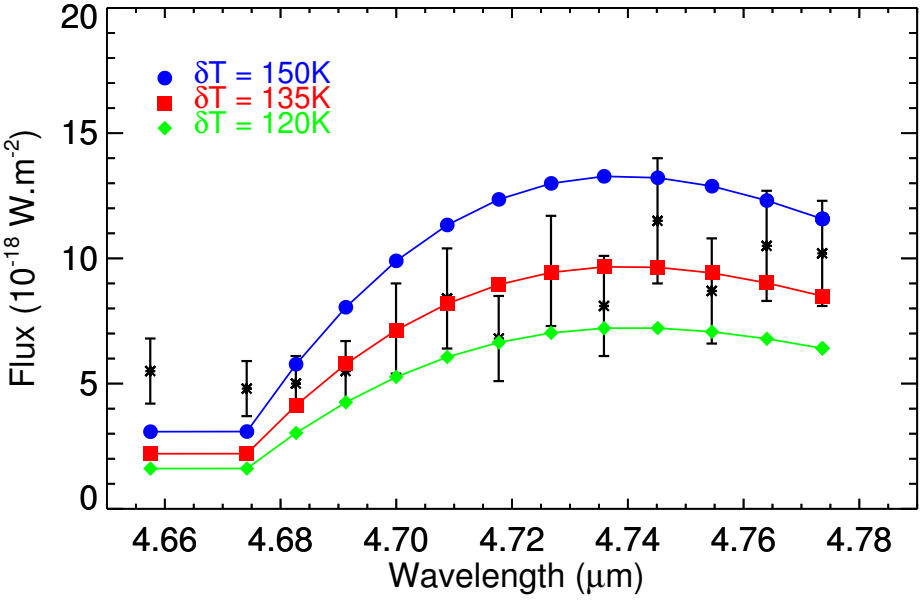


Figure 2.3 Model CO rovibrational fluxes from decoupled gas/dust temperature models compared with the observational data (depicted as crosses with error bars, from Salyk et al. 2007). The models show three different values of $\delta$T, the temperature difference between gas and dust, with values of 120 (diamonds), 135 (squares), and 150 K (circles).

The $v$=1-0 P(1-12) CO line fluxes at 4.7 $\mu$m are taken from Salyk et al. (2007), while the model spectra are generated by the raytracing code RADLite (Pontoppidan et al., 2009). The lines are $\sim$7.5 km/s wide (FWHM) (Pontoppidan et al., 2008), consistent with the nearly face-on orientation of TW Hya. The inner edge of the CO emission in the inner disk is set at $r_{in}$ = 0.11 AU, based on SA imaging of the 4.7 $\mu$m line emission (Pontoppidan et al., 2008). The outer edge of the CO-emitting zone is not well constrained, and is set to 4 AU, the dust transition radius. The model is relatively insensitive to the size of the outer edge, since the majority of the emission is produced at radii $\ll$ 4 AU.

The best fit has $\delta$T=135$\pm$15 K (Figure 2.3). From M-band rotation diagram fits, Salyk et al. (2007) derive $N_{CO} = 2.2 \times 10^{18}$ cm$^{-2}$, corresponding to a vertical total gas column density of $N_H \sim 10^{22}$ cm$^{-2}$. The 135 K gas-to-dust temperature difference is consistent with the detailed gas temperature balance model of Najita et al. (2011), whose treatment yields $\delta$T$\sim$100 K at r=0.25 AU for an integrated column density

of $N_H = 10^{22}\,cm^{-2}$. RADLite simulations predict a line width (prior to instrument profile convolution) of FWHM$\sim$6.8-9.6 km/s for $v_{turb} \sim 0.05\,v_{Kepler}$. This is somewhat larger than observed 7.5 km/s linewidths, but this difference may be accounted for by the difference in disk inclination relative to that ($i = 4°$) derived by Pontoppidan et al. (2008).

The best fit $\delta$T of 135 K applies only to the inner disk radii probed by CO, but similar physics will decouple the gas and dust temperatures near the disk surface at larger radial distances. To model this decoupling, we adopt $T_g = T_d + \delta T \times e^{-r/50\,AU}$ for the gas temperature at large scale heights, a parameterization that matches broadly the models of Thi et al. (2010) for TW Hya. Again, the gas density structure follows that of the dust.

We stress that such gas/dust thermal decoupling should have only a modest impact on a principle molecular mapping result presented here, namely the significant drop in the water vapor column density beyond the snow line. For the highest excitation lines measured by *Herschel* (and *Spitzer*) that trace the photon-dominated, and thus heated, layers in the inner disk and cavity wall, gas densities are at least $\sim 10^9$ $H_2/cm^3$. Under such conditions the simulations of Meijerink et al. (2009) show that the emergent fluxes of the water lines detected here are within factors of two-three of their LTE values. Thus, the water vapor column densities should be reasonably well determined by LTE calculations whose temperature distributions are constrained by the CO M-band observations.

The outer disk is too cold to emit in such high excitation water lines, and as discussed further in Section 4.4, the physical density in the $A_v \sim 1$ layer at radii beyond 5-10 AU is only $\sim 10^7$ $H_2/cm^3$, some 100-1000$\times$ less than the critical densities of the mid- to far-infrared water vapor lines examined here. Only the lowest-excitation water transitions measured by *Herschel* principally trace the outer, deeper disk layers. Here the M-band CO observations are of little use, but the lowest-J pure rotational lines do probe the relevant disk gas. In RADLite simulations of lines up to J = 6-5 we find, in agreement with Qi et al. (2004), that significant CO depletion in the cold disk midplane is needed to match the observed line fluxes. Water can be expected

to deplete in a similar manner, with the bulk of the vapor emission arising from an intermediate layer at densities where LTE calculations offer column density estimates good to within an order-of-magnitude (Hogerheijde et al., 2011).

## 2.5 Retrieving the radial water vapor profile

### 2.5.1 The water line model

Given the gas temperature and density structure for TW Hya, we can now constrain the water vapor content of the TW Hya disk surface as a function of radius. Our goal is not to provide an exacting description of the volatile abundances versus radius and height, but to determine what radial distribution of water vapor is most consistent with the available data.To this end, we construct a step function in water vapor abundance, with one value, $X_{\rm inner}$, in the inner gas-depleted disk within 4 AU, another, $X_{\rm ring}$, in a ring starting at 4 AU and extending to the snow line at $R_{\rm snow}$, and an outer disk abundance $X_{\rm outer}$. That is,

$$X_{\rm H_2O} = \begin{cases} X_{\rm inner}, & R < 4\,{\rm AU} \\ X_{\rm ring}, & 4\,{\rm AU} \leqslant R \leqslant R_{\rm snow} \\ X_{\rm outer}, & R > R_{\rm snow} \end{cases} \tag{2.2}$$

As described below, our calculations assume LTE but do account for line and continuum opacity. The $X_{\rm H_2O}$ values derived thus reflect the water vapor column densities to different depths into the disk. Inside of 4 AU and for the longest wavelength *Herschel* lines sensitive to the outermost radii the dust opacity permits the full vertical extent of the disk to be sampled. For the IRS features and the shorter wavelength PACS lines that sample gas near the transition radius, significant dust opacity limits the fitted column densities, and hence the $X_{\rm H_2O}$ values, to the upper layers of the disk. Freeze-out and dust/line opacity greatly limit access to the midplane beyond 4 AU.

Given the wide span in upper level energies of the lines considered, it is generally

possible to identify subset of lines that co-vary. Consequently, we can explore one model parameter at a time to derive a best-fit model, illustrated in Figure 2.4. As we shall see, the simplest LTE model, namely a constant water abundance throughout the disk, is inconsistent with the data in hand.In Section 4.2.2, we further discuss whether the data support a modification to this basic structure in which the drop in water abundance beyond the snow line instead occurs over some finite, measurable distance.

To render model spectra, we set the level populations to LTE. While the critical densities ($n_{\rm crit} = 10^{10} - 10^{12}$ cm$^{-3}$) of the high energy mid-IR water transitions suggest that a non-LTE treatment is needed, there is currently no robust and fully tested non-LTE framework for the modeling of infrared water lines. That is, a non-LTE calculation is also likely to be inaccurate, given the uncertainty of collisional rates and the complexity of the transition network. Further, previous work suggests that non-LTE effects may alter line fluxes by factors of only a few for the moderate excitation lines detected here (Meijerink et al., 2009; Banzatti et al., 2012), which will preserve the qualitative aspects of our treatment. In setting level populations to LTE, we make it easier to reproduce our results and to evaluate the validity of our retrievals using more detailed models in the future.

We assume a subsonic turbulent velocity broadening of $v_{\rm turb} \sim 0.05\, v_{\rm Kepler}$, and a constant ortho-to-para (O/P) water ratio of 3:1, one that is consistent with the mid- and far-infrared lines (Pontoppidan et al., 2010b). The cold gas seen by HIFI has a lower O/P ratio of 0.7 (Hogerheijde et al., 2011), but the difference does not substantially affect the derived abundance structure. Model spectra are typically rendered with a grid of 0.3 km/s, and then convolved with a Gaussian instrument response function to match the observed spectra. The *Herschel* HIFI spectra are rendered with a finer velocity grid of 0.05 km/s.

Table 2.2. Observed and calculated water line fluxes

| Type | Transition | $\lambda$ ($\mu$m) | $E_{up}$ (K) | A coefficient ($s^{-1}$) | Flux ($10^{-19} W/m^2$) | Model ($10^{-19} W/m^2$) |
|---|---|---|---|---|---|---|
| o-$H_2O$ | $11_{39}$-$10_{010}$ | 17.23 | 2438.8603 | 9.619E-1 | < 163.7 | 37.6 |
| p-$H_2O$ | $11_{29}$-$10_{110}$ | 17.36 | 2432.5234 | 9.493E-1 | < 617.3 | 110.4 |
| o-$H_2O$ | $8_{36}$-$7_{07}$ | 23.82 | 1447.5970 | 6.065E-1 | | |
| p-$H_2O$ | $9_{81}$-$8_{72}$ | 23.86 | 2891.7024 | 3.128E+1 | | |
| o-$H_2O$ | $9_{82}$-$8_{71}$ | 23.86 | 2891.7022 | 3.128E+1 | | |
| o-$H_2O$ | $8_{45}$-$7_{16}$ | 23.90 | 1615.3501 | 1.034 | 4669±364[a] | 3051 |
| o-$H_2O$ | $11_{66}$-$10_{55}$ | 23.93 | 3082.7639 | 1.612E+1 | | |
| p-$H_2O$ | $11_{56}$-$10_{47}$ | 23.94 | 2876.1493 | 9.754 | | |
| p-$H_2O$ | $8_{53}$-$7_{44}$ | 30.47 | 1807.0023 | 8.923 | | |
| p-$H_2O$ | $7_{61}$-$6_{52}$ | 30.53 | 1749.8575 | 1.355E+1 | 3750±317[a] | 4940 |
| o-$H_2O$ | $7_{62}$-$6_{51}$ | 30.53 | 1749.8506 | 1.355E+1 | | |
| o-$H_2O$ | $8_{54}$-$7_{43}$ | 30.87 | 1805.9308 | 8.687 | 1883±287[a] | 3393 |
| o-$H_2O$ | $6_{34}$-$5_{05}$ | 30.90 | 933.7488 | 3.504E-1 | | |
| o-$H_2O$ | $8_{18}$-$7_{07}$ | 63.32 | 1070.7757 | 1.730 | < 123.2 | 84.8 |
| o-$H_2O$ | $7_{07}$-$6_{16}$ | 71.95 | 843.5459 | 1.147 | < 127.2 | 77.0 |
| p-$H_2O$ | $8_{17}$-$8_{08}$ | 72.03 | 1270.3910 | 3.099E-1 | < 35.4 | 11.6 |
| o-$H_2O$ | $4_{23}$-$3_{12}$ | 78.74 | 432.1913 | 4.852E-1 | < 39.1 | 76.3 |
| p-$H_2O$ | $6_{15}$-$5_{24}$ | 78.93 | 781.1873 | 4.501E-1 | < 54.3 | 33.7 |
| p-$H_2O$ | $3_{22}$-$2_{11}$ | 89.99 | 296.8471 | 3.541E-1 | < 60.9 | 45.8 |
| p-$H_2O$ | $4_{13}$-$3_{22}$ | 144.52 | 396.4126 | 3.345E-2 | < 5.9 | 8.5 |
| o-$H_2O$ | $2_{12}$-$1_{01}$ | 179.53 | 114.3874 | 5.617E-2 | < 8.6 | 10.7 |
| p-$H_2O$ | $1_{11}$-$0_{00}$ | 269.27 | 53.4366 | 1.852E-2 | 3.07± 0.19 | 3.24 |
| o-$H_2O$ | $1_{10}$-$1_{01}$ | 539.29 | 60.9686 | 3.477E-3 | 3.46± 0.15 | 1.89 |

Note. — a. Water lines are often blended in the *Spitzer* IRS LH spectrum due to the limited resolution of R∼600. The fluxes are measured by integrating the spectrum over each distinctive feature/region after a linear continuum subtraction.

### 2.5.2 Best-fitting model

The best-fitting radial water column density profile in TW Hya is shown in Figure 2.4, whose spectral predictions are compared to the *Spitzer* LH data in Figure 2.5. We find that the inner optically thin region of TW Hya is *dry*, with upper limits on the vertically integrated fractional water abundance of $X_{\rm inner} < 10^{-6}$. The water detected by *Spitzer* originates in a thin ring near the disk surface, starting at 4 AU and ending at a snow line just beyond this at $R_{\rm snow} \sim 4.2$ AU. At larger radii, the fractional water abundance drops abruptly by *several orders of magnitude*, to $X_{\rm outer}$ values near $3.5{\times}10^{-11}$.

The uniqueness of this solution is illustrated in Figure 2.6, which shows how variations in the water abundance in different regions of the disk affect different lines. This differential sensitivity is the foundation of our method for retrieving the radial column density, and thus abundance, profile, and are the subject of the following discussion.

#### 2.5.2.1 The inner disk

The inner disk of TW Hya – radii within 4 AU – is partially cleared out, leading to integrated vertical column densities that are more than two orders of magnitudes lower than those typical for cTTs. The non-detection of water lines between 10 and 20 $\mu$m, in the *Spitzer* SH range, may be a reflection of this, but even though the column density in the inner disk is dramatically reduced from the extrapolation of the outer disk to smaller radii, the scale height is sufficiently small that the physical densities at the $A_v{\sim}1$ surface exceed $10^9$ $H_2/cm^3$. Thus, non-LTE effects are likely to be fairly unimportant, and we are able to produce meaningful upper limits on the fractional water abundance at $r$ <4 AU.

We investigated the effects on the *Spitzer* and *Herschel* lines when varying the inner disk abundance ratios between $X_{\rm inner} = 10^{-7}$ and $10^{-4}$. Interestingly, we find that inner disk fractional abundances higher than $10^{-6}$ significantly overpredict sev-

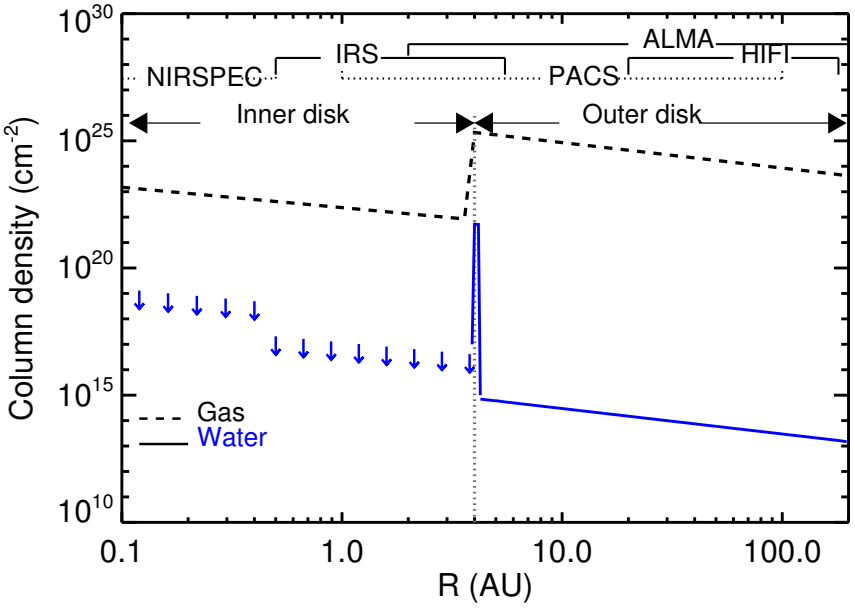


Figure 2.4 The best-fit radial abundance of water vapor in TW Hya, illustrated by the vertically integrated column density profile (solid curve). Within 4 AU, the maximum water abundance is depicted by arrows. The dashed curve is the total gas column density. At the top of the figure, the role of multi-wavelength observations in tracing different radii of the disk are highlighted, along with representative facilities of each wavelength window.

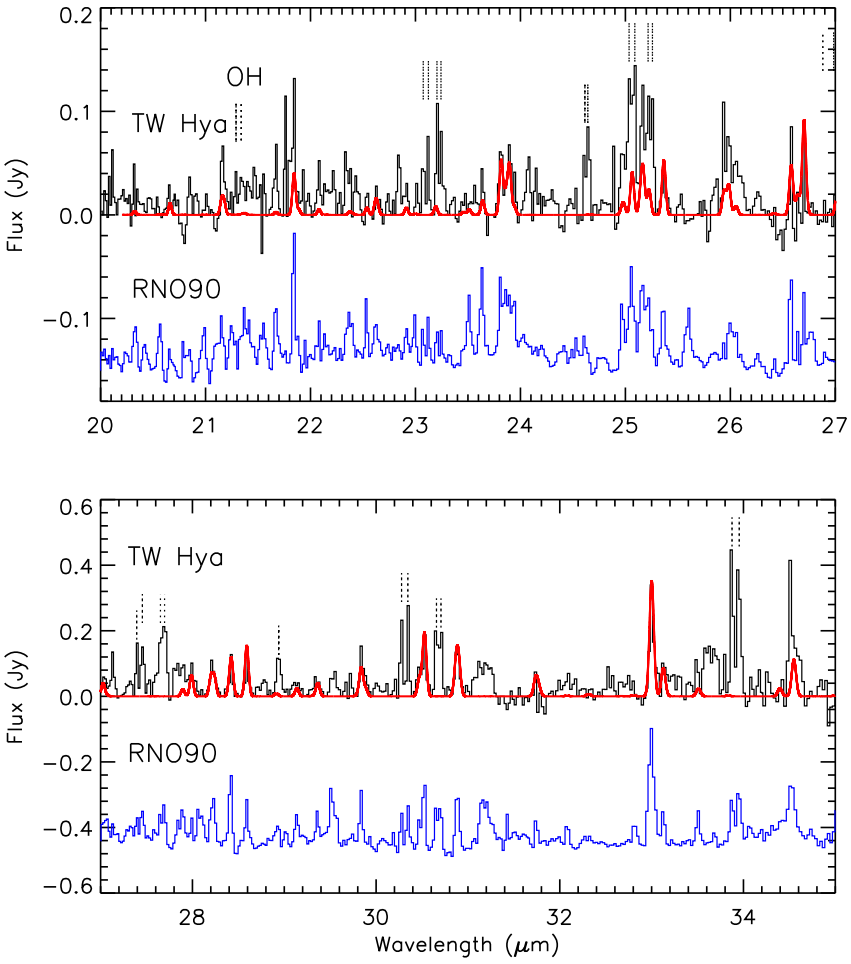


Figure 2.5 Detailed comparisons of the *Spitzer* IRS spectrum (black) with RADLite LTE water models (red). The spectrum of RNO90, one of the strongest water emitters in Pontoppidan et al. (2010b), is plotted at bottom, to guide the eye. The vertical dashed markers show the location of OH lines not discussed in this paper.

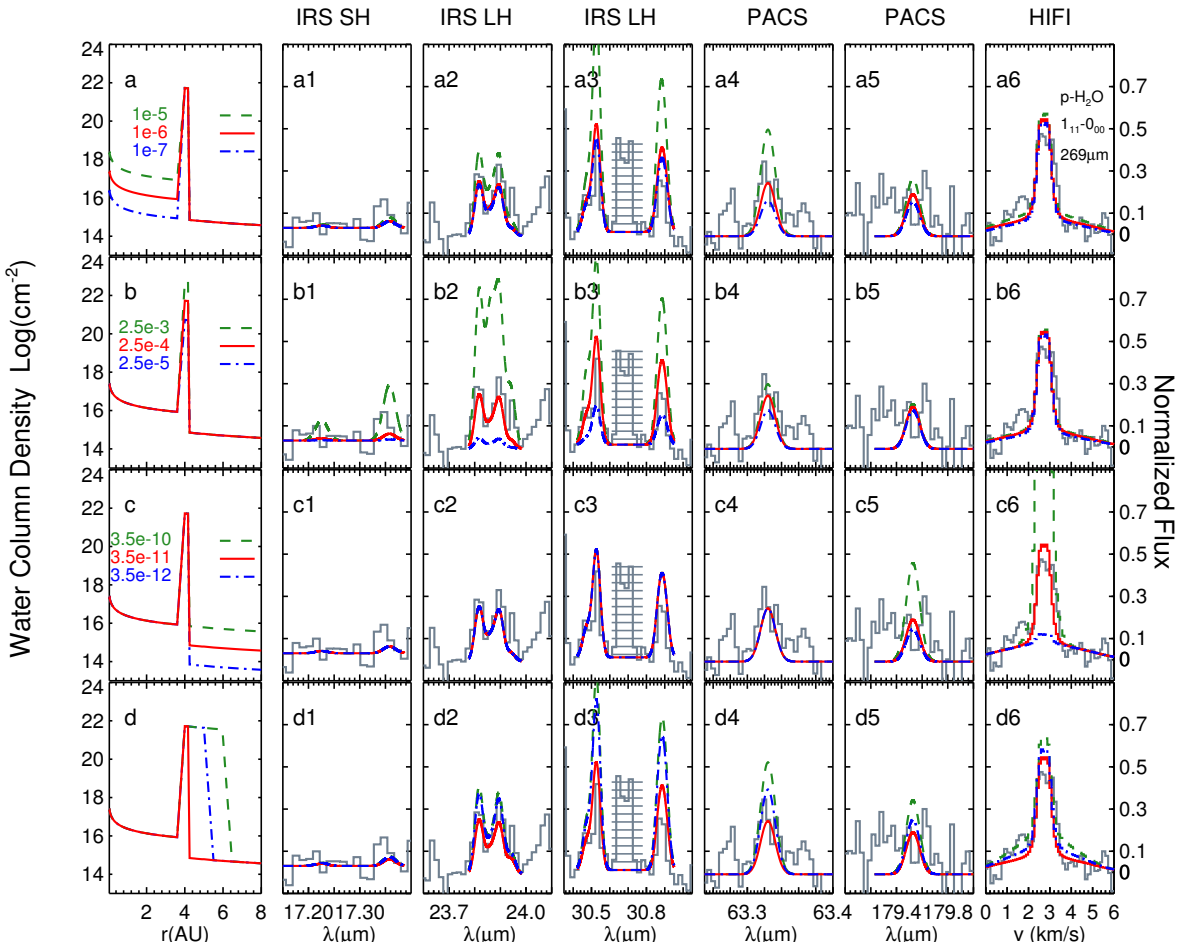


Figure 2.6 The sensitivity of selected water line fluxes to variations in the water vapor column density distribution. The first column shows the model water vapor distributions. The best-fit model is the solid red curve, while the green and blue curves are models calculated to illustrate the sensitivity of the various lines to changes in the water abundance at different disk radii. The numbers in the first column indicate the fractional (per hydrogen molecule) water abundance in (a) the optically thin inner disk, (b) the ring at the transition radius and (c) the outer disk. The final (d) panel shows the sensitivity of the model to the radius of the snow line. The following six columns show model line spectra compared to the observed spectra for TW Hya. The ladder crossed line in the 30 $\mu$m column is OH, which is not discussed in this paper. Please see Fig. 2.5 for additional OH line identifications.

eral water lines in the PACS range, especially the high excitation 63.3 $\mu$m lines, while the *Spitzer* SH lines allow somewhat larger abundances. That is, the *Spitzer* SH spectrum tends to be consistent with a model in which the lack of lines below 20 $\mu$m is explained by the overall low gas mass in the inner disk, and not necessarily a drier disk. It is the addition of the non-detection of PACS lines that require the fractional water abundance to be suppressed in the inner disk.

#### 2.5.2.2 The transition region and the snow line

Next, we consider the origin of the water lines seen at 20-35 $\mu$m. Figure 2.6 shows that the *Spitzer* LH lines detected are uniquely sensitive to variations in the water vapor content around the transition region. It is clear that a high water vapor column density is required to fit the *Spitzer* spectra, with an emitting area close to $\pi\times1$ AU$^2$. Our fiducial dust/gas model yields $X_{\rm ring} \sim 2.5 \times 10^{-4}$ above the $\tau_{\rm dust}$=1 surface (line opacity is also significant). As discussed in §5.2, the required column density/abundance can be traded off against excitation temperature to some extent, with higher excitation temperatures corresponding to slightly smaller radii.

In the context of our transitional disk model, the most likely location for warm water vapor lies at the transition radius, or 4 AU, a prediction that can be tested by measurements of the water (or perhaps OH) emission line profiles using high resolution thermal-infrared spectroscopy. Interestingly, the cavity "wall" structure needed to reproduce the 10-30 $\mu$m SED (with a $z/r$ value of 0.3) has a surface area close to that derived from the water emission for an inclination of seven degrees, further reinforcing the likely radial location of the high water vapor abundance.

Further, the PACS and HIFI lines are sensitive to the location of the snow line (the outer edge of the water-rich ring). Consequently, we varied the location of the snow lines between 4.2-6 AU. In Figure 2.6, it is seen that placing the snow line farther out in the disk over-predicts primarily the PACS lines. Hence, the detection of water lines by *Spitzer* in combination with the non-detection of water lines in PACS waveband provides strong constraints on the location of the surface snow line.

We explored one more aspect of the water abundance profile around the snow line.

Because the water condensation temperature is a function of pressure and because of the strong vertical gradients in the disk, the local water vapor abundance need not precisely be a step function in radius. In particular, can the water lines between 40-150 $\mu$m be used to constrain how rapidly the water abundance, as inferred from the column density structure, drops beyond the snow line with radius?

Specifically, we modify the abundance step function with an exponential drop-off beyond the snow line:

$$\mathrm{X_{H_2O}}(R > R_{\mathrm{snow}}) = (X_{\mathrm{ring}} - X_{\mathrm{outer}})e^{\left(\frac{R_{\mathrm{snow}}-R}{R_{\mathrm{eff}}}\right)} + X_{\mathrm{outer}}, \tag{2.3}$$

where $R_{\mathrm{eff}}$ is the scale length of the abundance change. We consider $R_{\mathrm{eff}}$ = 0.1, 0.5, and 1 AU, and find that models with $R_{\mathrm{eff}} \gtrsim 0.5$ AU produce more flux than is observed by the *Herschel* PACS instrument (Figure 2.7). This supports our original assumption of a step function, and we conclude that the surface snow line in TW Hya is radially narrow; that is, it occurs over a region that is a small fraction of its distance to the star.

#### 2.5.2.3 The outer disk

An extremely low vertically averaged abundance beyond the snow line, $X_{\mathrm{outer}}$=3.5×10$^{-11}$, is required by LTE fits to the HIFI ground state water lines at 267 and 537 $\mu$m. Indeed, the strongest constraint on the outer disk water vapor abundance is provided by the ground-state lines, although significant limits are also provided by slightly higher-lying transitions in the PACS range, in particular the 179.5 $\mu$m transition. The low water vapor content of the outer disk is consistent with the analysis of Hogerheijde et al. (2011) and the HIFI non-detection of water lines in another transitional disk, DM Tau (Bergin et al., 2010). Specifically, our $X_{\mathrm{outer}}$ is comparable to the global disk-averaged value derived by Hogerheijde et al. (2011) – 7.3×10$^{21}$ g of water in a 1.9×10$^{-2}$ M$_\odot$ disk, or $X_{\mathrm{H_2O}}$=2.2×10$^{-11}$ – but as these authors stress there is likely significant vertical structure in the water vapor abundance and a large ice reservoir beyond 4-5 AU.

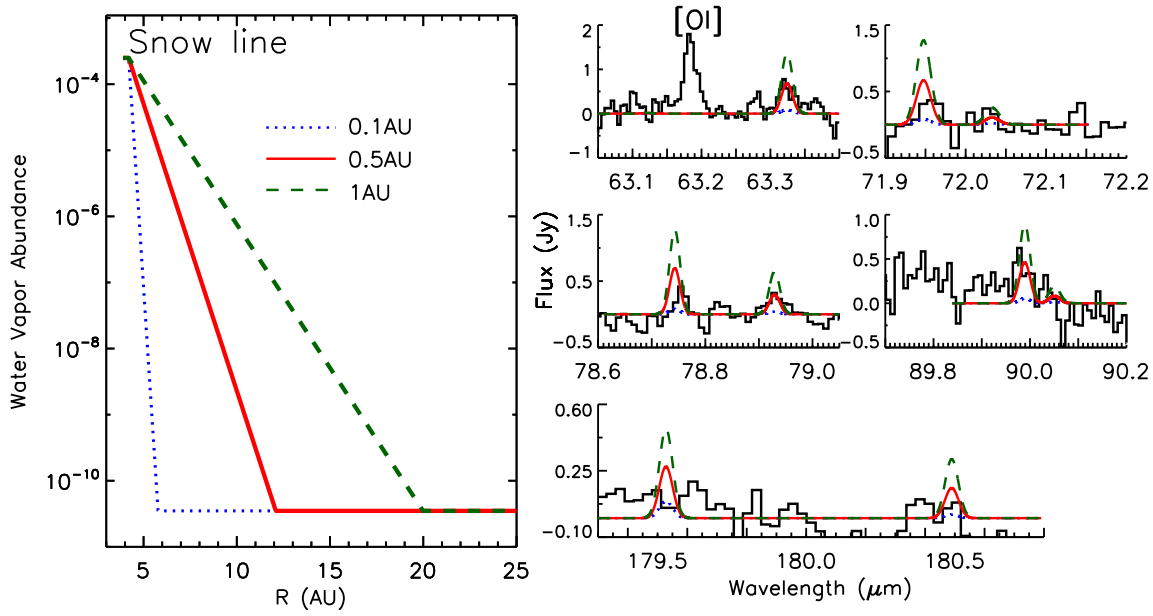


Figure 2.7 Constraints on the sharpness of the snow-line in TW Hya. The left panel shows model water vapor abundance decreases from $X_{H_2O} \sim 2.5 \times 10^{-4}$ to $3.5 \times 10^{-11}$ with three different radial scale lengths: 0.1 AU (dot line), 0.5 AU (solid line) and 1 AU (dash line). The right panel shows the modeled LTE line fluxes over-plotted on *Herschel* PACS spectra. The line styles are the same as in the left panel.

## 2.6 Discussion

From an analysis of the water emission lines from the TW Hya disk over the 10 – 567 $\mu$m interval, both warm (∼220 K) and cold water vapor are found to be present. The warm water emission most likely originates in a narrow ring region between 4–4.2 AU where abundant water vapor carries much of the cosmically available oxygen, $X_{H_2O} \sim 10^{-4}$. Outside of 4.2 AU, the vertically averaged water vapor column density decreases dramatically over a radial distance less than 0.5 AU, marking the location of the disk's surface snow line. Each of the datasets included in this study uniquely constrain one aspect of the distribution profile, and so we demonstrate the importance of the use of multi-wavelength datasets. Here we discuss some implications of our results.

### 2.6.1 The origin of the surface water vapor

How does this study inform the origin of the observed water vapor, and of water in protoplanetary disks in general? There are two potential sources of water: one is in situ gas-phase formation, while the other is grain surface formation in a cold reservoir, which could be the disk itself or the primordial protostellar cloud. In the second case, a mechanism is needed to transport the ice inwards and upwards to a location where it can either thermally evaporate or be photodesorbed and observed in the form of vapor (see, for example, Supulver & Lin, 2000).

In the warm inner disk (r<1AU, z/r<0.2), $H_2O$ can be formed in the gas phase (Glassgold et al., 2009; Bethell & Bergin, 2009), even in the presence of substantial photolyzing radiation. The key is a sufficient supply of $H_2$, which drives the formation of water via successive hydrogenation of atomic oxygen in reactions with significant activation barriers. More precisely, we find that using the photodissociation rate calculated only at Ly$\alpha$ (which dominates the $3\times10^{-3}L_\odot$ FUV continuum flux), and water reaction rates from Baulch, D. L. (1972) – $k_{OH}=3.0\times10^{-14}Te^{-4480/T}$ cm$^3$ molecule$^{-1}$s$^{-1}$ and $k_{H_2O}=3.6\times10^{-11}Te^{-2590/T}$ cm$^3$ molecule$^{-1}$s$^{-1}$ – this simplified chemical model predicts water abundances near $10^{-4}$ when $T_g \gtrsim 200$ K, $n_g>10^9$ cm$^{-3}$. These conditions are satisfied in the inner disk and the cavity wall, but not necessarily in the photon-dominated upper layers of the outer disk.

Thus, production of water via gas-phase reactions can potentially explain the high abundance of ∼220 K water vapor observed inside the TW Hya snow line, even if the initial conditions are atomic, and only until the elemental abundance of oxygen is depleted ($\sim 5\times10^{-4}$ relative to H, Frisch & Slavin, 2003). Indeed, modern thermochemical models (Woitke et al., 2009; Najita et al., 2011; Walsh et al., 2012) predict both that much of the oxygen is locked up in water vapor in the warm inner disk and at large scale heights where the gas is heated by UV and X-ray photons.

The best fit water content just inside the TW Hya snowline is not sufficiently high enough to distinguish between in situ gas-phase formation and evaporating icy bodies, but is consistent with thermo-chemical models. Well inside the transition

radius, the water abundance drops by two orders of magnitude, in conflict with this simple model. However, the models by Woitke et al. and Walsh et al. do not include the depleted inner region of TW Hya, making direct comparisons difficult for the innermost disk.

The warm gas-phase chemistry will not operate in the outer disk. Here, the primordial surface ice chemistry will dominate (Tielens & Hagen, 1982), resulting in a huge reservoir of icy dust and larger bodies from which water molecules must be thermally evaporated or desorbed by high-energy particles and photons. As discussed in Bergin et al. (2010) and Hogerheijde et al. (2011), models of photodesorption from icy grains find that a depletion of icy grains from the outer disk surface, presumably by setting to the midplane, is needed to reproduce the low observed outer disk water vapor abundances. A zeroth-order expectation is that the water vapor abundance across the snow-line can be treated as a step function (Ciesla & Cuzzi, 2006), with high inner disk water vapor abundances created by a mixture of gas-phase reactions and evaporating icy bodies and a low outer disk abundance maintained by desorption.

We find a very low (vertically averaged) outer disk water abundance of a few times $10^{-11}$ per hydrogen, consistent with previous Herschel-HIFI observations, but in conflict with the static thermo-chemical models, which indicate surface abundances of $10^{-7} - 10^{-9}$ per H. We interpret this as further evidence for settling of icy grains in the outer disk of TW Hya.

Another potential test for icy-grain contributions to the observed disk water vapor content would be a measurement of the O/P ratio. For gas phase formation of water at $>200\,\mathrm{K}$, an O/P ratio of 3 is expected, while the O/P ratio for evaporation or sputtering can be considerably less than 3 for grain surface temperatures less than $\sim 40\,\mathrm{K}$. However, for higher temperature ices formed in regions close to the snow line, the O/P ratio may still be near 3. Thus, detailed measurements of the O/P ratio will be needed to trace the origin of the snow-line water vapor, such as could be obtained, for example, with next generation ground-based (VLT-VISIR) or space-based (JWST-MIRI) thermal-IR spectrographs.

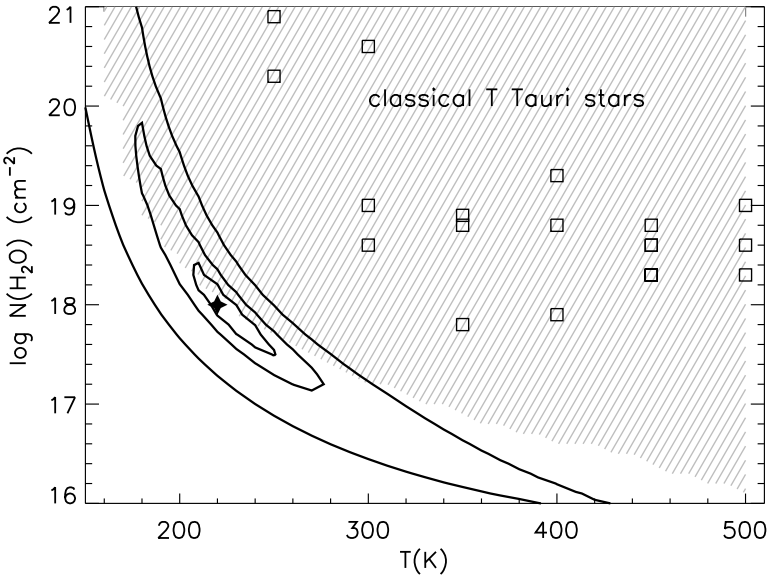


Figure 2.8 The $\chi^2$ surface for LTE slab model water fits for TW Hya as a function of $N$ and $T$, with an effective radius $R$=1.0 AU. The contour plot is based on *Spitzer* IRS LH spectra, with best-fit parameters of $T = 220$ K and $N$=$10^{18}$ cm$^{-2}$. The shadowed area depicts the parameter space that is excluded by the water upper flux limits from the *Spitzer* IRS SH spectrum. Empty squares depict the best LTE slab model fit results for cTTs with water detections in the *Spitzer*-IRS wavelength range (Salyk et al., 2011).

### 2.6.2 The water vapor abundance distribution in transitional disks

The *Spitzer* IRS spectrum reveals that the water vapor emission from TW Hya is different from that of typical, but less evolved, protoplanetary disks around solar-type stars. A comparison of the basic properties of the TW Hya water emission is shown in Figure 2.8, where an LTE slab model (disk-averaged) temperature and column density are compared to those of cTTs disks (Salyk et al., 2011). This is consistent with the detailed radial abundance structure derived for TW Hya.

Although the relative contribution to the observed water vapor in TW Hya from gas-phase reactions and evaporating icy planetesimals is unknown, it may be the ideal target to observe the evaporation process as its relatively small 'hole' size allows the

snow line to reside in the optically thick outer disk. In contrast, many of the known transitional disks have transition radii of 10 AU or greater (Andrews et al., 2011), and the snow-line would be located well inside the optically thin region of the disk. They also typically lie two or three times more distant than TW Hya. Therefore, comparisons with additional transitional disks may need to wait for the availability of more sensitive instruments.

In contrast to the ∼1 AU snow line found by Meijerink et al. (2009) for cTTs disks, the TW Hya snow-line is located at a significantly larger radius, in spite of its lower luminosity as compared to DR Tau and AS 205 N. In the case of transitional disks, however, the exposure of the transition radius to nearly unobstructed stellar light and the 'face on' nature of the cavity wall at the transition radius should heat the disk more readily at large radii and push the snow-line outwards. One interesting consequence of this property is that if giant planets form and clear out a hole in the disk, creating a transitional disk, the subsequent migration of the snow line to larger radii could slow the growth of new planetary cores over a larger range of radii, out to the location of the new snow line.

At the same time, new planetesimal formation may be *catalyzed* near the new snow line due to enrichment of water by a combination the radial cold finger effect of Stevenson & Lunine (1988) and inwards radial migration of icy bodies (Ciesla & Cuzzi, 2006). The observed high abundance of water around 4 AU in TW Hya is supportive of a scenario in which new icy planetesimal formation, and perhaps even giant planet formation, is ongoing at this location.

Another interesting feature of the distribution of water vapor abundance in TW Hya is the relatively dry inner disk. The water vapor abundance in the innermost disk ($< 0.5$ AU) is actually unconstrained by the *Spitzer* data due to beam dilution, but for $r > 0.5$ AU the abundance upper limit is two orders of magnitude below that estimated in cTTs disks, and the lack of water in inner disk can be explained by two possible scenarios.

First, the inner disk really is empty between 0.5-4 AU, a scenario consistent with near-IR interferometric data. Akeson et al. (2011) found that an inner optically thick

ring around 0.5 AU plus an outer optically thick disk starting at 4 AU can match the full suite of near-IR interferometric data and the general SED shape of TW Hya. Recent 8 - 18 $\mu$m speckle imaging, however, has suggested a more continuous dust distribution out to 4 AU and perhaps the presence of a companion (Arnold et al., 2012).

Furthermore, analysis of the ALMA CO $J$=2-1 and 3-2 Science Verification observations of TW Hya has revealed gas signatures down to radii as close as 2 AU (Rosenfeld et al., 2012). Thus, the more likely scenario for the structure of the TW Hya disk is that outlined in Figure 2.4, namely an inner disk in which CO remains abundant, since the kinetic temperature is much higher than that needed for freeze-out ($\sim 20\,\mathrm{K}$).Water in the inner disk can still be subjected to some depletion, or in the case that a companion gates the accretion flow into the inner disk any water-ice rich grains that settle to the (outer disk) mid-plane may be blocked from further inward migration. If this is the case, there should be a large difference in the gas phase C/O ratios between the inner and outer parts of the disk. Thus, the quantity of gas along with its C/O content potentially probes that can distinguish whether a given transition disk has been sculpted by planet formation or other mechanisms (grain growth or photo-evaporation, for example; see Najita et al. 2011 for further discussion of how changes in the C/O ratio can impact disk chemistry).

A final aspect of these observations is the short scale length ($<$0.5 AU) over which the dramatic water vapor decrease occurs, a distance in conflict with scenarios that consider only freeze-out. Such a radial profile may be further evidence for a vertical cold finger effect, in which the surface snow-line location reflects that at the mid-plane, perhaps due to mixing (Meijerink et al., 2009).

### 2.6.3 Molecular mapping with multi-wavelength spectra

We have demonstrated here how multi-wavelength spectroscopic data can be used to reconstruct molecular abundances, even when the observations are spatially (and often spectrally) unresolved.The snow line differences inferred for the tiny sample

observed to date are in accord with the changing physical conditions that passive cTTs disks experience as they evolve. Much more detailed constraints and comparisons to models will become available over the coming years by exploiting the significant infrared database that exists for stars+disks of varying mass and evolutionary state (Pontoppidan et al., 2010b; Salyk et al., 2011) along with new observations at longer wavelengths.

Because protoplanetary disks are complicated structures, the multi-wavelength molecular mapping method should be used with some caution, however. The flux of each line will arise from a range of disk regions, with lines at various wavelengths characterizing different radii and/or vertical depths, and an overview of several of the key water vapor tracers for the best fitting TW Hya model is presented in Fig. 2.9. As demonstrated in this work, it can take considerable effort to build realistic models for an individual source, and efforts herein were aided by a large set of ancillary observations of this well-studied disk. Nevertheless, it is important to stress that relatively fewer uncertainties are introduced in this type of modeling than with the use of full thermal-chemical disk models, in which chemical abundances are sensitive to a wide array of model parameters, including FUV and X-ray fluxes, accretion rate, disk viscosities and transport rates, dust-versus-gas settling geometries, grain-surface reaction rates, and so on (e.g. Heinzeller et al., 2011). Further, studies of large disk samples will require fast, robust models. We therefore advocate for the direct measurement of chemical abundances with relatively few free parameters, such as is described in this work, to be used in conjunction with physical intuition derived from the more complex thermal-chemical models.

It is interesting to note that the precision of derived abundance profiles is primarily determined by the availability of high-quality spectra across a wide range of excitation energies, as well as by the knowledge of the overall disk structure, especially the gas temperature. Thus, more precise measurements can be obtained as spectrographs with higher spectral resolution and sensitivity become available, irrespective of the instrumental spatial resolution (provided the disk structure is reasonably well characterized) – though of course instruments that provide detailed kinematic profiles

of lines with a significant range of excitation energies will provide the most stringent probes. This technique thus provides an ideal means to study chemical structure at the size scales relevant to planet formation.

With a properly chosen spectral suite, we have demonstrated that it is possible to probe molecular abundance distributions on AU scales, and it is worth emphasizing that this method is highly complementary to the capabilities of ALMA. At its longest baselines (16 km), the full ALMA will be able to resolve a nearby disk (140 pc) on AU scales at its shortest operational wavelength, $\sim$400 $\mu$m, in dust emission. However, due to the quantum-limited nature of heterodyne receivers and the available collecting area, it will be a severe challenge even for ALMA to robustly image the warm molecular gas inside of 10 AU – the principle formation region of terrestrial and giant planets according to core accretion theory. Thus, for the foreseeable future, multi-wavelength methods (which can incorporate ALMA spectral data cubes) offer perhaps the best means of deriving the molecular abundance patterns in planet-forming environments. Table 2.3 presents the general selectivity of each wavelength window for disks around Sun-like stars.

Although current observational S/N levels limit chemical abundance studies to a few species, this technique can in principle be applied to the study of any molecule whose transitions cover sufficient excitation space. The gas phase distribution of condensible species provides particularly valuable information on the temperature, density, chemical, and transport patterns in disks; and when used together, observations of a wide variety of molecules are best suited to the isolation and thus understanding of particular disk processes. To combine both infrared and (sub)mm data on the inner/outer disk, polar species with greatly differing sublimation temperatures are preferred. The most obvious candidates, beyond water vapor and OH, are CO and HCN, which are widely detected in surveys of protoplanetary disks. The former provides a fiducial chemical marker that only becomes significantly affected by freeze-out at very low temperatures, while the abundance drop for HCN across the snow line may well be sensitive to the C/O ratio in the gas.

Table 2.3. Volatile line tracers at different disk radii

| Wavelength $\mu$m | Radius AU | Facility |
|---|---|---|
| 2-5 | 0.1 | NIRSPEC, CRIRES |
| 6-10 | 0.1- 1 | SOFIA FORECAST |
| 10-35 | 0.5- 5 | Spitzer IRS |
| 40 - 200 | 1-100 | Herschel PACS |
| 200- 30000 | >50 | HIFI, ALMA |

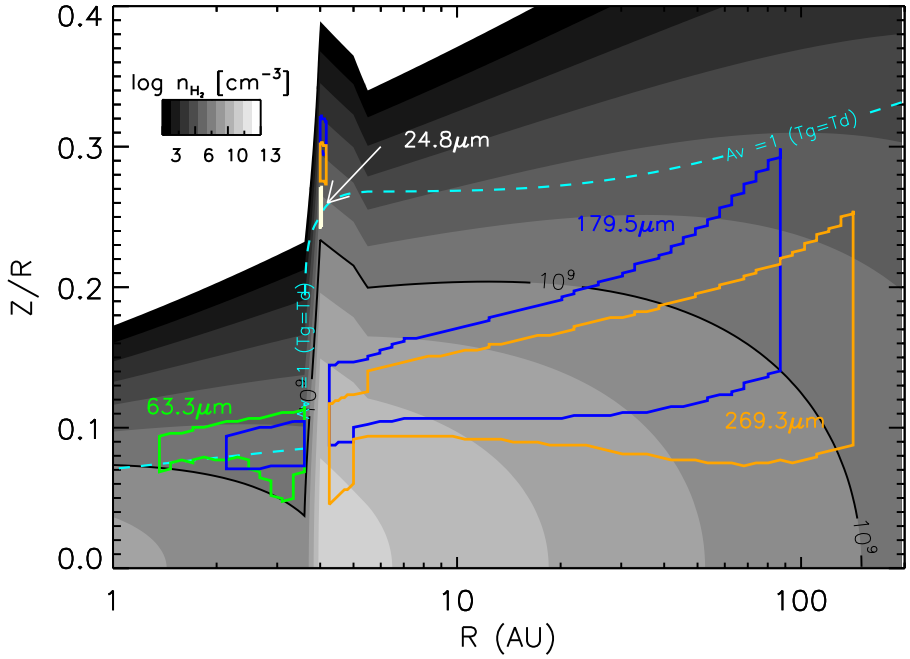


Figure 2.9 The radial and vertical locations bounding water vapor emission from the TW Hya disk. The boxes mark the 15% and 85% cumulative radial line flux limits (vertical lines) and the heights where 15% and 85% of the line flux arises from each vertical column (horizontal lines). The gas density of the disk is shown in greyscale, and the location of the $A_v$~1 gas/dust decoupling transition ($T_g = T_d$) is shown by the dotted line. As a guide to the eye, the $n_{H_2} = 10^9$ cm$^{-3}$ density contours are labeled by the solid line. Excitation and dust/line opacity are principally responsible for the lack of sensitivity to the cold, dense disk midplane (c.f. Figure 2.2).

## 2.7 Conclusions

This paper uses multi-wavelength spectra to probe the water vapor distribution in protoplanetary disks, and demonstrates the first application of this method to investigate the water vapor abundance from 0.5-200 AU in the transitional disk TW Hya. Our modeling shows that there is a narrow region between 4-4.2 AU where water vapor is warm ($\sim$220 K) and optically thick, resulting in a high abundance ($X_{H_2O}\sim10^{-4}$). Outside the snowline, the water vapor column density in the disk atmosphere decreases dramatically over a scale length of less than 0.5 AU due to freeze out, resulting in a vertically integrated vapor abundance of $X_{H_2O}\sim10^{-11}$ at large radii.

Both current and near-term astronomical facilities from the near-IR to radio frequencies can generate a rich molecular data set of the emission lines from protoplanetary disks. We expect the multi-wavelength molecular mapping method will soon be applied to a substantial ensemble of disks and molecular species.

# Chapter 3

# Comparison of the dust and gas radial structure in the transition disk [PZ99] J160421.7-213028

Ke Zhang[1], Andrea Isella[1], John M. Carpenter[1], Geoffrey A. Blake[2]

1. Division of Physics, Mathematics & Astronomy, MC 249-17, California Institute of Technology, Pasadena, CA 91125, USA; kzhang@astro.caltech.edu

2. Division of Geological & Planetary Sciences, MC 150-21, California Institute of Technology, Pasadena, CA 91125, USA

*Keywords:* Stars: pre-main sequence; planetary systems: protoplanetary discs; submillimeter: stars

This chapter, with minor differences, was published in its entirety under the same title in *The Astrophysical Journal*, 2014, Volume 791, pp. 42-52.

## 3.1 Abstract

We present ALMA observations of the 880 $\mu$m continuum and CO $J$= 3-2 line emission from the transition disk around [PZ99] J160421.7-213028, a solar mass star in the Upper Scorpius OB association. Analysis of the continuum data indicates that 80% of the dust mass is concentrated in an annulus extending between 79 and 114 AU in radius. Dust is robustly detected inside the annulus, at a mass surface density 100 times lower than that at 80 AU. The CO emission in the inner disk also shows a significantly decreased mass surface density, but we infer a cavity radius of only 31 AU for the gas. The large separation of the dust and gas cavity edges, as well as the high radial concentration of millimeter-sized dust grains, is qualitatively consistent with the predictions of pressure trap models that include hydrodynamical disk-planet interactions and dust coagulation/fragmentation processes.

## 3.2 Introduction

Planets form in the disks orbiting young stars, but the paths by which the primordial gas and dust accumulate into planetary bodies remain unclear. The capabilities of new optical, infrared, and (sub)-millimeter telescopes can place constraints on the planet formation process by mapping the gas and dust emission of planetary systems in the act of formation. Transition disks, defined by their significantly reduced infrared emission at wavelengths $<8\,\mu$m compared to the median disk emission (Strom et al., 1989; Wolk & Walter, 1996), are of particular interest. The relative lack of infrared emission implies the absence of warm dust in the innermost disk. This dust depletion might be a manifestation of the early stages of planet formation as a result of the dynamic interactions between the disk and forming giant planets (Lin & Papaloizou, 1979; Artymowicz & Lubow, 1994), but other mechanisms can suppress near-infrared dust signatures without the presence of planets, such as a decrease in the dust opacity due to grain growth (e.g., Strom et al., 1989; Dullemond & Dominik, 2005) or disk photoevaporation driven by stellar radiation (e.g., Clarke et al., 2001; Alexander et al., 2006a).

The three mechanisms outlined above can reproduce the infrared Spectral Energy Distributions (SEDs) characteristic of transition disks (Alexander et al., 2006b; Birnstiel et al., 2012; Alexander, 2014), but make different predictions about the relative spatial distributions of the gas and dust. In the planet-disk interaction scenario, the gaseous disk is expected to be truncated near the planet orbital radius. Depending on the viscous properties of the disk, dust grains larger than a few millimeters in size are expected to decouple from the gas and concentrate in a narrow ring with a radius larger than the gas truncation radius (Zhu et al., 2012; Pinilla et al., 2012). In the grain growth scenario, the drop in infrared opacity is due to the coagulation of sub-micron grains into larger bodies, but the gaseous disk should extend inward down to a few stellar radii. Finally, disk photoevaporation preferentially removes the gaseous disk and sub-micron sized grains entrained in the gas flow. The inner edge of the gas disk moves steadily outwards and the strong inward pressure gradient at the

evaporation radius drives all dust grains smaller than a few millimeter size outwards. As a result, the grains are swept up by the moving edge of the gas disk. In this case, the truncation radius of the gaseous and dusty disk components are expected to be similar, and some large grains ($\geq$ cm-sized) might be able to survive inside the gas-free regions if not removed by other means (Alexander & Armitage, 2007).

High spatial resolution images of the gas and dust emission are thus key to investigating the nature of transition disks. Sub-millimeter observations are particularly valuable since the dust continuum traces the distribution of millimeter-sized dust grains while molecular line emission traces that of the gas. Sub-arcsecond continuum images obtained for the brightest transition disks have revealed large cavities and, in some cases, azimuthal asymmetries in the distribution of millimeter-sized grains (Piétu et al., 2007; Brown et al., 2008; Hughes et al., 2009; Isella et al., 2010; Andrews et al., 2011; Isella et al., 2012; Casassus et al., 2013; van der Marel et al., 2013; Isella et al., 2013; Pérez et al., 2014). The CO emission has been imaged at high angular resolution in only a few cases and reveals that molecular gas is present in the dust cavity (Piétu et al., 2007; Isella et al., 2010; Casassus et al., 2013; Pérez et al., 2014; Bruderer et al., 2014). However, the limited sensitivity and angular resolution of existing observations, and the large optical depth of low-$J$ CO transitions, have so far hampered a detailed comparison between the gas and dust spatial distributions.

In this paper, we present 880 $\mu$m ALMA observations of the [PZ99] J160421.7-213028 (henceforth J1604-2130) transition disk that resolve the dust continuum and molecular gas emission on subarcsecond angular scales. J1604-2130 is a member of the Upper Scorpius OB association at a distance of 145 pc (de Zeeuw et al., 1999), with a spectral type of K2, a stellar mass of 1.0 $M_{\odot}$, and an estimated age between 5 and 11 Myr (Preibisch et al., 2002; Pecaut et al., 2012). The disk is the most massive known around K-M type stars in the Upper Scorpius OB association (Mathews et al., 2012; Carpenter et al., 2014) and has one of the largest cavities reported in continuum emission – R$\sim$72 AU, as revealed by 880 $\mu$m SMA observations (Mathews et al., 2012). The SMA observations also suggest that the CO $J$=3-2 distribution that may extend closer to the star than the millimeter-emitting dust. Our ALMA observations achieve

substantially higher signal-to-noise ratios compared to the SMA observations to place stringent constraints on the spatial distributions of gas and dust in J1604-2130.

This paper is organized as follows. The observations and data calibration are presented in Section 5.3. Section 4.4 discusses the morphology of the dust and gas emission. The ALMA data are compared to the predictions of theoretical models for the disk emission in Section 3.5, and the results of the model fitting are presented at the end of the same section. In Section 5.7, we discuss the nature of the J1604-2130 transition disks and a summary of the main results follows in Section 3.7.

## 3.3 Observations

The observations of J1604-2130 were carried out on 28 August 2012 as part of the ALMA cycle 0 project 2011.0.00526.S (Carpenter et al., 2014) with 28 12-meter antennas. The total integration time on J1604-2130 was 315 seconds. Baselines ranged from 21 to 402 m (23-457 k$\lambda$). The spectral setup consists of four windows centered at 345.77, 347.65, 335.65, and 333.77 GHz, respectively, each providing a total bandwidth of 1.875 GHz in 488 kHz (0.42 km s$^{-1}$) channels. The data are Hanning smoothed, so the spectral resolution is twice the individual channel width.

Reduction and calibration of the data were performed using the Common Astronomy Software Application (CASA) version 4.1 (McMullin et al., 2007). Quasar J1625-2527 was observed before and after the on-source integrations for phase calibration. Short-term phase variations were corrected using the on-board water vapor radiometers, and the visibilities were self-calibrated on the continuum emission of the science source to reduce atmospheric decoherence. The bandpass was calibrated with the radio sources J1751+0939 and J1924-292, and the visibility amplitude scale was calibrated from observations of Titan with an estimated uncertainty of $\sim$10%. For each $uv$ point, we fitted the visibilities of each spectral window with a power-law ($F_\nu \propto \nu^\alpha$). We then subtracted the best-fit result from the data, and measured the variance ($\sigma^2$) in the residual; $1/\sigma^2$ is used as the weight of each $uv$ point.

Four lines are detected: CO $J$= 3-2 (345.795 GHz), H$^{13}$CO$^+$ $J$= 4-3 (346.998 GHz),

$H^{13}CN$ $J$= 4-3 (345.339 GHz), and $HN^{13}C$ $J$= 4-3 (348.340 GHz). Continuum emission from J1604-2130 was extracted from the total 7.5 GHz coverage by combining the line-free channels from all four windows after flagging the edge channels. The spectral lines were first continuum-subtracted in the $uv$ domain, and the composite visibilities then Fourier inverted, deconvolved with the CLEAN algorithm using natural weighting, and restored with a synthesized beam of size $0''.73 \times 0''.46$ (106×67 AU at 145 pc). The beam major axis position angle is 105° east of north. Here we focus on an analysis of the dust continuum and CO data because the optically thick CO emission better traces the full radial extent of the gaseous disk.

## 3.4 Results

Figure 3.1 presents the 880 $\mu$m synthesized continuum image of J1604-2130 along with the real and imaginary visibilities. The continuum image shows a resolved "ring" morphology, characterized by a radius of about $0.''6$, or 90 AU at 145 pc. The continuum flux density integrated over a central $4''$ square box is 226±1 mJy (with 10% absolute flux uncertainty). Mathews et al. (2012) reported a lower continuum flux of 165±6 mJy (20% absolute flux uncertainty) from SMA observations by integrating all flux above a $2\sigma$ contour. Using an integration region similar to that in Mathews et al. (2012), we obtained a total flux of 202 mJy, consistent with the SMA result within the absolute flux uncertainties. The high signal-to-noise (S/N) ALMA image allows the inclusion of weaker emission from the outer disk, and is therefore a more accurate measure of the integrated continuum flux density. The synthesized continuum image has an rms noise level of 0.18 mJy beam$^{-1}$, yielding a signal-to-noise ratio of >200.

The radial profile of the real visibilities shows two nulls at 120 $k\lambda$ and 300 $k\lambda$, respectively. The amplitudes of the first and second lobe are about 30% and 13% of the intensity on the shortest baselines, indicating a sharp transition in the radial surface brightness profile. Similar structure is seen in the SMA observations of J1604-2130 but with a lower amplitude, suggesting a smoother radial profile. The difference in morphology between the ALMA and SMA observations is possibly due to the

fact that the higher sensitivity of ALMA observations allowed self-calibration to be applied to the data, reducing the de-correlation caused by atmospheric turbulence.

The radially averaged imaginary visibilities show values consistent with zero up to about 400 $k\lambda$, implying that the continuum emission is symmetric on angular scales as small as $0.''5$. Note that the apparent double-lobed morphology in the continuum map is due to the elliptical shape of the beam, and not to an intrinsic asymmetry in the dust emission. A slight deviation from azimuthal symmetry is observed on the longest baselines, where the imaginary visibilities reach values near 10 mJy, and in the continuum image, where the northern peak is $\sim$10% brighter than its counterpart to the south.

An overview of the CO $J$ = 3-2 data is provided in Figure 3.2. The line channel maps in the first row show clear signatures of rotation, with emission firmly detected ($>5\,\sigma$) over a narrow velocity range between 3.46 and 6 km s$^{-1}$ due to the nearly face on geometry. We measure an integrated intensity of 21.4$\pm$0.2 Jy km s$^{-1}$ over a central $6''$ square box, consistent with CO 3-2 line flux from single dish observations of 21.7$\pm$0.8 Jy km s$^{-1}$ (Mathews et al., 2013) but 4.1$\times$ larger than that reported by the SMA (Mathews et al., 2012), for which the line flux was calculated by summing over only those regions with a signal-to-noise ratio$\geqslant$2. The higher S/N of the ALMA image allowed CO $J$=3-2 emission to be detected over an extended region of the disk which contains a significant fraction of the total flux.

In the second row of Figure. 3.2 we display the CO $J$ = 3-2 zeroth (a) and first (b) moment maps, the deprojected visibility profile (c) and the spatially integrated spectrum (d). Similar to the continuum emission, the CO $J$= 3-2 momentum zero map shows a double-lobed morphology, which indicates an inner cavity in the CO emission, but the peak-to-peak separation in CO (a preliminary indication of the inner ring radius) is noticeably smaller than that of the continuum emission. The CO emission is also more diffuse than the continuum, extending to $\sim$290 AU in radius. Fig. 3.2(c) displays the deprojected CO visibility profile (integrated across the line shape). Compared to the continuum, the null in the visibility profile occurs at a longer baseline length and the side lobes are less prominent, indicating a smoother CO brightness

distribution.

The CO $J$= 3-2 moment zero map shows depressed emission in the inner $\sim$0.″3, which could in principal be explained either by a depleted gas surface density or temperature variations. We argue that temperature variation is unlikely to be the case here. Extremely cold gas inside of 30 AU is physically implausible. For hot gas inside this radius the resulting excitation can indeed produce an optically thin $J$= 3-2 transition, but we do not detect any CO rovibrational emission at 4.7 $\mu$m with Keck NIRSPEC (probing gas temperature $\geqslant$ 300 K, e.g. Salyk et al. 2009). This rules out the possibility of a significant high temperature CO reservoir in the inner disk. Since CO and $H_2$ can survive the intense UV radiation in the cavities of transition disks down to a gas surface density of $10^{-4}$ g cm$^{-2}$ (Bruderer, 2013), we assume CO coexists with $H_2$. We thus consider the most likely case for the depressed CO emission is that the gas is largely depleted inside the cavity.

## 3.5 Modeling Analysis

The goal of this section is to model the continuum and CO emission from the disk around J1604-2130. Because of differences in optical depths, these two tracers probe different regions of the disk. At the typical densities of circumstellar disks, the millimeter-wave dust emission is typically optically thin and therefore traces the dust density and temperature in the disk mid-plane. In contrast, the CO emission is expected to be optically thick and therefore traces the gas temperature at larger scale heights. For this reason, we fit models to the dust and CO observations in separate steps.

First, we construct a disk model that reproduces the broadband SED composed of data from the literature and the ALMA 880 $\mu$m continuum observations. This enables us to constrain the dust mass surface density and, through radiative transfer calculations, the mid-plane temperature. Starting from the best fit model for the dust continuum emission, we then fit the CO emission to constrain the parameters that mostly affect the gas emission, such as the gas temperature and the component

of the gas velocity along the line-of-sight.

### 3.5.1 Dust emission: model description

We adopt a model for the mass surface density of the dusty disk similar to that presented in Mathews et al. (2012), which is briefly summarized here. In order to reproduce the the disk SED and ALMA observations with a minimum number of free parameters, we construct a disk model composed of the three radially distinct regions (see Figure 3.3). The outermost disk region, at $R > R_{cav}$, is described by the similarity solution of a viscous accretion disk (Lynden-Bell & Pringle, 1974), adopting the parameterization of Isella et al. (2009),

$$\Sigma(R) = \Sigma_t \left(\frac{R_t}{R}\right)^{\gamma} \times exp\left\{-\frac{1}{2(2-\gamma)}\left[\left(\frac{R}{R_t}\right)^{2-\gamma} - 1\right]\right\}, \tag{3.1}$$

where $R_t$ is the radius at which the transition between power law and exponential profiles occurs, $\Sigma_t$ is the surface density at $R_t$, and $\gamma$ defines the slope of the surface density profile. At $R_{gap} < R < R_{cav}$, the disk model has a depleted dust region characterized by constant mass surface density $\delta \times \Sigma(R_{cav})$, with $\delta$ <1. Finally, to account for the depressed infrared excess for $\lambda$ <8 $\mu$m, the disk region within $R_{gap}$ is devoid of dust. The dust surface density model is therefore defined as

$$\Sigma_{dust}(R) = \begin{cases} 0, & \text{if } R < R_{gap} \\ \delta \times \Sigma(R_{cav}), & \text{if } R_{gap} \leq R < R_{cav} \\ \Sigma(R), & \text{if } R > R_{cav} \end{cases} \tag{3.2}$$

The vertical dust density profile is a Gaussian

$$\rho(R, Z) = \frac{\Sigma_d(R)}{\sqrt{2\pi}h(R)} e^{-\frac{z^2}{2h^2(R)}}, \tag{3.3}$$

in which the scale height $h(R)$ varies with radius as $h(R) = h_0(R/R_0)^{1+\phi}$. We set the reference radius $R_0$ to 100 AU. We choose to parameterize the scale height instead

of assuming hydrostatic equilibrium because the vertical distribution of millimeter grains and gas may differ due to the settling of large dust grains toward the disk mid-plane (D'Alessio et al., 2001).

We assume a dust population of astronomical silicates and carbonaceous grains, with optical constants as in Draine (2003) and Zubko et al. (1996), respectively, and at relative abundances as in Pollack et al. (1994). Single grain size opacities are calculated using Mie theory under the assumption of spherical grains. The single size grain opacities are then integrated over the grain size distribution $n(a)$ as described in Miyake & Nakagawa (1993). We assume a power-law grain size distribution, $n(a) \propto a^{-3.5}$, from $a_{\rm min}$= 0.005 $\mu$m to a given $a_{\rm max}$.

After defining the properties of the dusty disk, we calculate the dust temperature and the corresponding emission using the 2D Monte Carlo radiative transfer code RADMC (Dullemond & Dominik, 2004), where the stellar radiation field is calculated assuming $T_{\rm eff}$ = 4550 K, $R_\star = 1.41\,R_\odot$, and $M_\star = 1\ M_\odot$ (Preibisch et al., 2002).

In summary, the model for the dust continuum emission has 11 free parameters: three that describe the gap and cavity of the transitional disk $\{R_{gap}, R_{cav}, \delta\ \}$, three that define the surface density in the outer disk $\{\Sigma_t,\ R_t,\ \gamma\}$, two that characterize the vertical density distribution $\{h_0, \phi\}$, two that define the orientation of the disk on the sky, i.e., inclination and position angle $\{i,$ PA$\}$, and one ($a_{\rm max}$) that defines the maximum dust grain size.

### 3.5.2 Dust emission: fitting procedure and results

Obtaining the best fit model by exploring an 11-D parameter space is computationally challenging. Instead, we reduce the dimensionality of the problem by taking into account the fact that the disk SED and the spatially resolved 880 $\mu$m dust continuum observations probe two nearly independent sub-sets of model parameters.

The disk infrared emission is optically thick and mainly probes the disk temperature, which depends on the vertical profile of the disk through the parameters $h_0$, $\phi$, and $R_{gap}$ (e.g., D'Alessio et al., 2006). At (sub-)millimeter wavelengths, the disk

emission is optically thin and its spectral slope depends on the dust opacity, which, in our model, is controlled by the maximum grain size $a_{max}$ (see, e.g., Testi et al., 2014). In particular, the optically thin 880 $\mu$m emission profile probes the surface density of millimeter-sized grains, as defined by the parameters $\Sigma_t$, $R_t$, $\gamma$, $R_{cav}$, and $\delta$. Finally, observations of the molecular line emission are the best tracer of the disk orientation. We therefore assume a disk inclination of 6° and a position angle of 77°, as derived from the analysis of the CO emission presented in Section 3.5.4.

To find the disk model that best reproduces the dust emission observations, we first use the slope of the millimeter SED to constrain the maximum grain size $a_{max}$. In the optically thin case, the slope of the dust opacity $\beta$ is related to the slope of the flux, $\alpha$, by the relation $\alpha = \beta + 2$. In the case of J1604-2130, $\alpha = 3.2 \pm 0.2$, leading to $\beta = 1.2$ (Mathews et al., 2012). This corresponds to a maximum grain size of about 0.05 mm for the dust composition and grain size distribution discussed above. The dust opacity at 880 $\mu$m is 7.26 cm$^2$ g$^{-1}$.

We then use the Levenberg-Marquardt $\chi^2$ minimization algorithm (LM) to search for the optimum values of $h_0$, $\phi$, and $R_{gap}$ by comparing the synthetic disk emission with the measured SED between 1-200 $\mu$m. We note that the IRAC photometric data for J1604-2130 are discrepant from its IRS spectra and the WISE photometry results between 3 and 16 $\mu$m (Carpenter et al., 2006; Dahm & Carpenter, 2009; Luhman & Mamajek, 2012). This discrepancy might suggest variability in the IR disk emission as observed, e.g., in the case of LLRL 31 (Muzerolle et al., 2009). Taken at face value, the near-IR excess suggested by the WISE photometry is well fit with an optically thick ring of dust at the temperature of 1500 K extending from 0.043 AU to 0.049 AU, where the former radius is the dust evaporation radius for a star with the properties of J1604-2130 (Isella et al., 2006). Such a warm dust component so close to the star would be distinct from the cool outer disk, whose dust emission peaks at 100 $\mu$m. Thus, fitting the IRAC data only, as was done in Mathews et al. 2012, should have little effect on other disk parameters except $R_{gap}$.

In either case and as discussed above, the infrared SED is insensitive to the exact value of the disk surface density provided the disk is optically thick to stellar radiation.

In this step we therefore assume the surface density used by Mathews et al. (2012). We show the best fit model for the SED in Figure 3.4, for which $R_{gap} = 14.6 \pm 2.5$ AU, $\phi = 0.6 \pm 0.1$, and $h_{100\mathrm{AU}} = 4.0 \pm 0.2$ AU. Fitting the WISE photometry with an optically thick blackbody component results in a larger $R_{gap} = 26.5 \pm 2.8$ AU, closer to that derived from CO (discussed in Section 4.4).

As second step, we compare synthetic 880 $\mu$m images to the ALMA observations to constrain $\Sigma_t$, $R_t$, $\gamma$, $R_{cav}$, and $\delta$. To make a fair comparison with previous work on transition disks, we adopt $\gamma = 1$ (Andrews & Williams, 2007; Andrews et al., 2011).

We will discuss the effect that this choice has on the results in § 3.5.5.

The model fitting is performed in the Fourier domain adopting the procedure discussed in Isella et al. (2009). In brief, the synthetic image is Fourier transformed to calculate the synthetic visibilities on a regular $uv$ grid, which are then interpolated at the $uv$ coordinates sampled by the ALMA observations. The $\chi^2$, defined as

$$\chi^2 = \sum_i [(\mathrm{Re}_i^o - \mathrm{Re}_i^m)^2 + (\mathrm{Im}_i^o - \mathrm{Im}_i^m)^2] \cdot w_i^o, \tag{3.4}$$

is used as the likelihood estimator. In Equation 3.4, Re and Im are the real and imaginary part of the complex visibilities; the upper-case "o" means observation and "m" stands for model. The weight $w$ is calculated as described in §2.

We adopt a hybrid method of Levenberg-Marquardt $\chi^2$ minimization algorithm (LM) and Markov chain Monte Carlo (MCMC) approach (Piétu et al., 2007; Isella et al., 2009). The LM algorithm is first used to search for the best fit values, from which the MCMC code is used to obtain probability distributions around the LM best fit parameters. In practice, we launch 150 independent LM algorithms with random initial values to avoid local minima. Most searches end up with very similar values. Then, we carry out 10 independent MCMC calculations starting at the medium value of the best fit LM searches. A total number of $5 \times 10^4$ models were run.

Table 3.1 lists the best fit values for the dust continuum model, which is compared to the ALMA 880 $\mu$m continuum data in Figure 3.5. Panel (a) shows the azimuthally averaged visibilities, while panels (b - d) display the continuum image, model, and

Table 3.1. Disk parameters

| Dust disk parameters | reduced $\chi^2 = 2.02$ | |
|---|---|---|
| Cavity radius | $R_{cav}$ (AU) | 78.8±0.1 |
| Depletion factor | $\log(\delta)$ | -1.86±0.03 |
| Surface density | $\Sigma$ ($R_{cav}$) (g cm$^{-2}$) | (9.4±0.1)×10$^{-2}$ |
| Transition radius | $R_t$ (AU) | 10.6±0.2 |
| CO parameters | reduced $\chi^2 = 1.02$ | |
| Cavity radius | $R_{CO}$ (AU) | 31.2±0.3 |
| Turbulence factor | $\xi$ | 0.25±0.01 |
| Temperature at 100AU | $T_0$ (K) | 45.8±0.2 |
| Temperature index | $q$ | -0.64±0.01 |
| Position angle | PA (°) | 76.8±0.5 |

Note. — The errors are $1\sigma$ uncertainty.

residual. The residual image is produced by subtracting the model visibilities from those observed, and then imaging the results following the same procedure used for the observations. Low level residuals ($\sim 5\,\sigma$) exist on the west side of the disk and suggest an azimuthal variation in the dust density or temperature of $\lesssim 10\%$.

We find that the dust cavity radius is about 79 AU. Within this radius the dust is depleted by almost two orders of magnitude. The surface density at the cavity edge corresponds to an optical depth of 0.7, and the total mass in dust is $0.16\,M_{Jup}$. The transition radius, $R_t$ (see Eq. 3.1), is much smaller than the cavity radius, implying that the dust surface density at the position of the ring decreases nearly exponentially with radius. As a result, the dusty ring is very narrow, with approximately 80% of the mass contained between 79 AU and 114 AU.

### 3.5.3 CO emission: model description

The model used to analyze the ALMA $^{12}$CO $J$= 3-2 spectral line observations is similar to that presented in Isella et al. (2007). At the typical densities of protoplanetary disks, the rotational transitions of CO are optically thick and therefore trace the temperature of the layer characterized by $\tau_{\rm CO} \sim 1$ (Beckwith & Sargent, 1991, 1993; Dutrey et al., 1996; Isella et al., 2007). Chemical models of disks and direct observations suggest that the optically thick CO layer is located far above the mid-plane, where the gas density is low and the collisions between dust grains and CO molecules are rare (Woitke et al., 2009; Walsh et al., 2012). Thus, a proper calculation of the gas temperature requires a fully coupled chemical and line radiative transfer model (e.g. Kamp & Dullemond 2004; Woitke et al. 2009; Walsh et al. 2012). Since this is beyond the scope of this paper, we parametrize the CO temperature as a power law, that is, $T_{\rm CO}(R) = T_0 \times (R/100{\rm AU})^q$. Although this choice is arbitrary, it enables us to describe the CO temperature independently from that of the dust with a minimum number of free parameters.

The low-$J$ CO lines generally provide poor constraints on the CO column density, and thus on the overall gas content. We therefore fix the gas-to-dust mass ratio and assume the gas and dust are well mixed. More precisely, the gas density is obtained by multiplying the dust density of the best fit model for the continuum emission by a constant gas-to-dust mass ratio of 100. The CO number density at each grid point of the disk is then calculated by assuming a constant CO/$H_2$ abundance ratio of $5\times10^{-5}$ (Aikawa et al., 1996). The critical density of the CO 3-2 transition is $\sim 10^4\,{\rm cm}^{-3}$ from 5-2000 K (Yang et al. 2010), a value reached in our disk model only in regions at least five scale heights above the mid-plane. We can thus safely assume the CO is in Local Thermodynamic Equilibrium (LTE).

We allow for distinct gas and dust truncation radii as the CO moment zero map reveals that the gas disk extends inside the cavity observed via the dust. We set an outer edge of the CO disk as that radius where the CO temperature reaches 17 K – the condensation temperature of CO onto dust grains (Aikawa et al., 1996).

For each line-of-sight in the disk, the observed CO line width has contributions from the different rotational velocities and thermal plus turbulent broadening. The thermal broadening is calculated as $V_{\rm thermal}=\sqrt{2k_bT_{\rm CO}/m_{\rm CO}}$, where $k_b$ is the Boltzmann constant and $m_{\rm CO} = 28\,{\rm m_H}$ is the CO molecular mass. The turbulent velocity is assumed to be equal to a fraction of the local sound speed, that is, $V_{turb} = \xi c_s$, where $\xi$ is a free parameter. Finally, the gaseous disk is assumed to rotate at the Keplerian velocity corresponding to a stellar mass of 1 $\rm M_\odot$, and the component along the line-of-sight is calculated by assuming a disk inclination angle of 6° as measured by Mathews et al. (2012).

In summary, the model for the CO emission has five free parameters: the CO temperature at 100 AU $\{T_0\}$, the radial slope of the CO temperature $\{q\}$, the turbulence velocity parameter $\{\xi\}$, the inner radius of the CO disk $\{\rm R_{CO}\}$, and the position angle of the disk {PA}.

### 3.5.4 CO emission: fitting procedure and results

For any set of free parameters $\{T_0,\ q,\ \xi,\ \rm R_{CO},\ PA\}$ we calculate the synthetic CO $J$= 3-2 line emission using the ray-tracing code RADLite (Pontoppidan et al., 2009) under LTE assumption. The model cube is convolved to the velocity resolution of the observations and re-sampled at the velocity grid of the channel maps. As with the dust continuum emission model, the synthetic CO channel maps are Fourier transformed to calculate the theoretical visibilities at the *uv* coordinates sampled by the data. A minimization on the $\chi^2$ surface (Equation 3.4) is then performed to find the best fit model.

Following the dust modeling, we start with 150 independent LM runs and random initial values in the search. However, the computational time required to generate synthetic CO data cubes precludes an efficient sampling of the four dimensional $\chi^2$ surface using a MCMC procedure. Instead, we use the Hessian matrix to derive the the uncertainties on the model free parameters following the method presented in Piétu et al. (2007).

The best fit values for the model parameters are listed in Table 3.1, while the comparison between the synthetic and observed channel maps is presented in Figure 3.6. We find that the CO disk is truncated at an inner radius of 31 AU, larger than the gap radius ($R_{gap}$) inferred for the dusty disk from the SED modeling but half that of the partially dust depleted cavity ($R_{cav}$) derived from the spatially resolved 880 $\mu$m continuum observations. Our analysis suggests that the temperature of the CO layer decreases with radius as $r^{-0.64}$ starting from a temperature of $\sim$100 K at 31 AU. The CO emission becomes optically thin around 350 AU, which sets the outer radius of the observable CO disk. Between 80 to 200 AU the temperature of the CO layer is 20-30 K higher than the mid-plane dust temperature, which is consistent with our initial assumption that the CO $J$= 3-2 emission mainly arises from a warm molecular layer above the mid-plane.

The residual maps presented in Figure 3.6 reveal that our model reproduces the main kinematic features of the CO emission. Thus, the observations are consistent with Keplerian rotation. We derive a turbulent velocity equal to $\sim$25% of the local sound speed, which is within the range predicted by MHD turbulence models (Simon et al., 2011a). Finally, we measure a disk position angle of 77°, a value consistent within errors with that derived from SMA 880 $\mu$m continuum and 1.6 $\mu$m polarized intensity images (Mathews et al., 2012; Mayama et al., 2012).

### 3.5.5 Uncertainties from the choice of $\gamma$

The results obtained so far assume that the disk surface density has a radial profile characterized by $\gamma = 1$. We relax this assumption here to assess its impact on the resulting disk structure. To this end, we repeated the dust continuum modeling assuming $\gamma = 0.5$ and $\gamma = 1.5$. The best fit models for $\gamma$ =0.5, 1, and 1.5 are listed in Table 3.2, while Figure 3.7 shows the comparison with data along with the corresponding surface density profiles and cumulative mass distributions.

All three models provide similar quality fits to the 880 $\mu$m visibilities. As expected, we find that $\gamma$ and $R_t$ are degenerate. Varying $\gamma$ also contributes additional

Table 3.2. Continuum model parameters for different $\gamma$

| $\gamma$ | $R_{cav}$ [ AU ] | log$\delta$ | $\Sigma(R_{cav})$ [ g cm$^{-2}$ ] | $R_t$ [ AU ] | $\chi^2_r$ |
|---|---|---|---|---|---|
| 0.5 | 78.2 | -1.79 | $7.8 \times 10^{-2}$ | 22.5 | 2.029 |
| 1.0 | 78.8 | -1.86 | $9.4 \times 10^{-2}$ | 10.6 | 2.024 |
| 1.5 | 78.0 | -1.90 | $8.8 \times 10^{-2}$ | 1.6 | 2.025 |

uncertainty to the cavity size and depletion factor estimates. Even so, the cavity size remains well constrained under the assumption of a sharp truncation at the cavity edge, with an uncertainty of ∼1 AU. The depletion factor varies from 0.013 to 0.018.

More generally, the parameters vary with $\gamma$ by more than the formal uncertainties derived by the MCMC probability distribution sampling discussed above. Thus the uncertainties in Table 3.1 should be used with caution. Nevertheless, the cumulative mass distributions of the three best fit models suggest that 80% of the dust mass traced by the ALMA data is concentrated in an annulus extending from ∼ 80 AU to 120 AU, a result that is independent of the exact disk mass surface density profile.

## 3.6 Discussion

### 3.6.1 Comparing J1604-2130 with other transition disks

The ALMA observations reveal that J1604-2130 disk has a large dust cavity with most of its dust mass concentrated in an narrow annulus (∼35 AU wide) beyond the dust truncation radius. Here we compare the mass distribution of J1604-2130 with other transition disks.

We define a characteristic width, $\Delta W$, by

$$\int_{R_{cav}}^{R_{cav}+\Delta W} \Sigma(r) \times 2\pi r dr = 0.8 \times \int_{R_{cav}}^{+\infty} \Sigma(r) \times 2\pi r dr \tag{3.5}$$

The average radius of the annulus holding 80% of disk mass is then $\overline{R}$=$R_{cav}$ +

$\Delta W/2$. The $\Delta W/\overline{R}$ ratio can be used as an tracer of the compactness of the mass distribution. In Figure 3.8(b), we compare $\Delta W/\overline{R}$ for J1604-2130 with that for the transition disks studied in Andrews et al. (2011). The surface density in all 13 disks was determined by analyzing resolved 880 $\mu$m continuum visibilities using similarity solution with $\gamma$ fixed at 1. Thus, all of the results are expected to represent the mass distributions of dust grains over similar sizes. Interestingly, J1604-2130 has the largest dust cavity among the thirteen disks but is also the most compact as measured via $\Delta W/\overline{R}$. It is worth mentioning that some of the transition disks might actually be more compact than they appeared since their SMA observations could be affected by decorrelation that will spread the dust emission.

This high concentration of dust and the large cavity radius is difficult to understand from viscous evolution alone because an expanding disk should produce a more diffuse mass distribution, unless a very large cavity can be opened early in the life time of the disk, $\sim 10^5$ yr (Isella et al., 2009). On the other hand, transition disks are clearly going through significant changes, so mechanisms other than viscosity are likely to be important in shaping the mass surface density at this particular evolutionary stage. We discuss possible scenarios for the evolution of the J1604-2130 transition disk next.

### 3.6.2 Formation of the J1604-2130 transition disk

The main result from the model fits to the dust continuum and CO emission is that the radius of the gas cavity (31 AU) is roughly half that of the dust (79 AU). Similar results are found in the transition disk IRS 48, where CO shows a 20 AU cavity while the dust is truncated at $\sim$45 AU (Bruderer et al., 2014).

Such differences in the gas and dust distributions have implications for the formation mechanisms of transitions disks. It is known that gas exists inside the dust cavity in some transition disks. Salyk et al. (2009) detected rovibrational CO lines near 4.7 $\mu$m in nine out of fourteen transitional disks, suggesting that high temperature gas often exists inside the cavity. Several transition disks show rotational CO

emission inside dust cavity, indicating that cool gas is present (e.g. Piétu et al. 2006; Isella et al. 2010; Tang et al. 2012; Casassus et al. 2013; Pérez et al. 2014). However, these observations were unable to determine if there is a cavity/gap in gas. Only in the case of GM Tau was CO inferred to be depleted within 20 AU based on the lack of high velocity wings in the rotational transitions of CO isotopologues (Dutrey et al., 2008).

We discuss here the possible formation mechanisms for the J1604-2130 transition disk, using the separate truncation edges in the dust and gas along with other observational properties as constraints. We consider (1) grain growth inside the cavity (D'Alessio et al., 2006), (2) mass-loss in a wind driven by photoevaporation or magneto-rotational instability (MRI) (Alexander et al., 2006a,b; Suzuki & Inutsuka, 2009), and (3) tidal interactions with companions (Bryden et al., 1999; Crida et al., 2006).

*Grain growth.* For J1604-2130, the clear detection of a large gas cavity indicates that grain growth is unlikely to be the dominant clearing mechanism, because even small amounts of gas containing CO are expected to survive inside a cavity where dust grains have grown to large size (Bruderer, 2013). Thus, the lack of CO emission inside of $\sim 31$ AU cannot be caused by pure grain growth.

*Photoevaporation.* Another possible mechanism for gas and dust removal is a wind driven by photoevaporation. However, two observational properties of J1604-2130 are inconsistent with the predictions of current photoevaporation models.

The first problem is the large separation between the gas and dust truncation radii. Disk photoevaporation preferentially removes the gaseous disk and sub-micron sized grains entrained in the gas flow. The inner edge of the gas disk moves steadily outwards and the strong inward pressure gradient at the evaporation radius sweeps up all dust grains smaller than a few millimeters in size. Only very large grains ($\geq$ cm-sized) might be able to survive inside the gas-free regions if not removed by other means. In this case, the gaseous and dusty disk components are both truncated at the inner rim of the outer disk (Alexander & Armitage, 2007). Thus, for either the grain growth or photoevaporation scenarios it is difficult to produce the large separation

between the characteristic gas and mm-sized dust radii in J1604-2130.

The second difficulty concerns the high mass surface density of J1604-2130. Photoevaporation winds continuously remove material from the disk surface. When a gap as large as tens of AU is opened, the surface density of the outer disk is expected to be less than $0.1\,\mathrm{g\ cm^{-2}}$ (Alexander et al., 2006b; Alexander & Armitage, 2007; Gorti et al., 2009). The gas surface density of J1604-2130 at the truncation edge is $\sim$10 g cm$^{-2}$ (assuming a gas-to-dust ratio of 100), far too massive to be explained by photoevaporation.

Tidal interactions with low mass companions. Here, interactions between brown dwarf companions and the disk are unlikely to be the cause of the J1604-2130 cavity. Kraus et al. (2008) have ruled out the presence of a close companion with aperture masking interferometry ($0.06\,\mathrm{M_\odot}$ down to $\sim$2 AU, and $0.01\,\mathrm{M_\odot}$ down to $\sim$9 AU), while Ireland et al. (2011) have placed upper limits on companion masses of 0.07-0.005 $\mathrm{M_\odot}$ at separations from 60-300 AU using adaptive optics. We thus compare the CO and dust radial structure with the predictions of disk tidal interactions with planets.

The disk-planet interaction scenario can naturally explain the large morphological differences in the gas and dust emission in J1604-2130. Recent disk-planet dynamical models (e.g. Pinilla et al. 2012; Zhu et al. 2012) have begun to incorporate dust coagulation and fragmentation processes in hydrodynamical simulations. One of the key features of these new models is that the difference between the planet orbital radius and the peak of surface density of mm-sized particles may be as large as tens of AU if the planet is sufficiently massive. A giant planet not only opens a gap in the disk, but also produces a local pressure maximum where dust particles within some size range can be trapped. The planet orbit and local pressure maximum separation depends on the mass of the planet – the more massive the planet, the larger the separation. For example, Pinilla et al. (2012) showed that the local pressure maximum can be located at more than twice the planet orbital radius for a $9\,\mathrm{M_{Jup}}$ planet.

A planet-induced disk pressure trap is also consistent with the high concentration of mm-sized dust in J1604-2130. Because the efficiency of dust trapping is size-dependent, the general observable outcome would be that the large grains are trapped

into the local pressure maximum while small grains and gas should persist in a more diffuse distribution (de Juan Ovelar et al., 2013). As shown in Figure 3.8, J1604-2130 has most of its mm-sized dust mass concentrated in a highly radially confined ring. Further, Mayama et al. (2012) reported that the 1.6 $\mu$m polarized intensity images (tracing micron-sized particles) that peak at $\sim$63 AU, which is 15 AU closer to the central star than the 880 $\mu$m emission. The 1.6 $\mu$m data also show that scattered light extends inwards to $\sim$40 AU (smaller separations lie within their saturation radius).

### 3.6.3 Pressure trap and evolution

In the ALMA 880 $\mu$m continuum and CO $J$=3-2 emission maps, J1604-2130 appears to be regular and largely azimuthally symmetric, but with the dust highly concentrated in a narrow ring. A similar morphology has recently been reported in the evolved circumbinary disk around V4046 Sgr (Rosenfeld et al., 2013a). In contrast, large azimuthal asymmetry features have been observed in several transitional disks (Brown et al., 2009; Regaly et al., 2012; Isella et al., 2013; van der Marel et al., 2013; Pérez et al., 2014), possibly caused by extended vortices created by planet-disk tidal forces or large viscosity gradients. Intriguingly, the two types of dust morphologies (azimuthal asymmetry and symmetry) are both consistent with the idea of a pressure trap, but are expected at different evolutionary stages.

Fu et al. (2014), for example, show that the emergence and lifetime of the vortices created by planets strongly depend on the disk viscosity – with vortices typically diffusing into a ring-like structures at later stages –while simulations of vortices caused by large viscosity gradients demonstrate that the vortices and rings appear alternately (see Figure 3 in Regaly et al. 2012). To make any further statement about the nature of these dust concentrations in disks, other manifestations of pressure trap must be observed, such as the expected radial variation of the dust-to-gas mass ratio, as well as disks at different evolutionary stages.

### 3.6.4 Dust inside the cavity

Transitional disks were first identified through the dip in their infrared SED, suggesting that warm dust near the central star is substantially depleted (Skrutskie et al., 1990). Since the infrared dust emission is usually optically thick, only lower limits to dust mass can be derived from the SED (Andrews et al., 2011). In contrast, the millimeter wavelength dust emission probes much larger column densities, but spatially resolved millimeter images have so far lacked the sensitivity to constrain the dust density inside the cavity. There is one case, LkCa 15, in which a small amount of 870 $\mu$m continuum emission has been detected inside the dust cavity, leading to an estimated surface density $\sim$5 times lower than the regions immediately beyond the dust cavity (Andrews et al., 2011). Our observation of J1604-2130 also shows detectable emission (at $\sim 10\sigma$) inside the cavity with a surface density of mm-sized particles nearly $\sim$100 times lower than that of the disk beyond the dust cavity. In both cases, the depletions estimated from sub-mm images are significantly higher than the $10^{-6}$– $10^{-5}$ typical lower limit from the transition disk SED analysis (Andrews et al., 2011). We stress, however, that the two depletion factors are difficult to quantitatively compare because the IR emission mostly arises from small dust grains ($\sim \mu$m size) in the disk atmosphere while the sub-mm emission is mainly from large grains ($\sim$mm-sized) close to the mid-plane of the disk.

### 3.6.5 Outer disk radius

The CO $J$=3-2 emission of J1604-2130 appears to extend to a radial distance much larger than the associated 880 $\mu$m continuum (see Figures 3.1 and 3.2). Similarly large discrepancies between continuum and gas emission have been observed in several other protoplanetary disks (Piétu et al., 2005; Isella et al., 2007; Panic et al., 2009; Andrews et al., 2012; Rosenfeld et al., 2013b). It has being debated whether the apparent size discrepancy reflects actual differences in the outer radii of dust and gas in these disks. Hughes et al. (2008) suggested that the apparent discrepancy may be due to optical depth effects, and demonstrated that models with a tapered exponential edge

in the surface density profile could better reproduce the dust and gas observations. There are some cases, however, where tapered surface density profiles are unable to simultaneously reproduce the CO and dust observations (Panic et al., 2009; Andrews et al., 2012; Rosenfeld et al., 2013b). In such cases, a radially varying gas-to-dust mass ratio is required to explain the observations. For the case of J1604-2130, we find that a tapered surface density profile and radially invariant gas-to-dust ratio is consistent with the current CO and continuum observations. Future high spatial resolution observation of optically thin transitions (e.g. CO isotopologue lines) are necessary to distinguish if the outer edge of gas and dust in J1604-2130 are truncated at different radii.

## 3.7 Summary

In this paper, we have studied the radial structure of the transitional disk J1604-2130 with sensitive ALMA data of the 880 $\mu$m continuum and CO $J$ = 3-2 line emission. The key conclusion of our analysis are:

- Both the dust continuum and CO gas show central cavities in the synthesized images but the gas truncation radius is about half that of the dust ($R_{CO} = 31$ AU vs. $R_{cav} = 79$ AU). The presence of a large gas cavity rules out the possibility of dust growth as the main mechanism for the central depletion. A large separation in the edges of gas and dust is not predicted by photoevaporation models, but is expected for massive planet-disk interactions.

- Dust inside the cavity is detected in the 880 $\mu$m continuum, but with a surface density 100 times lower than that just beyond the dust truncation radius. The estimated dust mass inside the dust cavity is $\sim 1.1 M_{\oplus}$.

- 80% of the dust mass is concentrated in an annulus extending between 79 and 114 AU in radius. This morphology is qualitatively consistent with the accumulation of dust grains in a local pressure bump such as that generated by the dynamical interaction between a gas giant planet and the disk.

## 3.8 Acknowledgments

We thank Crystal Brogan and Steve Myers for their assistance with the data reduction. The National Radio Astronomy Observatory is a facility of the National Science Foundation operated under cooperative agreement by Associated Universities, Inc. This paper makes use of the following ALMA data: ADS/JAO.ALMA#2011.0.00526.S. ALMA is a partnership of ESO (representing its member states), NSF (USA) and NINS (Japan), together with NRC (Canada) and NSC and ASIAA (Taiwan), in cooperation with the Republic of Chile. The Joint ALMA Observatory is operated by ESO, AUI/NRAO and NAOJ. A.I. and J.M.C. acknowledge support from NSF awards AST-1109334 and AST-1140063. K.Z. and G.A.B. gratefully acknowledge funding provided by NSF award AST-1109857 and NASA grant NNX11AK86G.

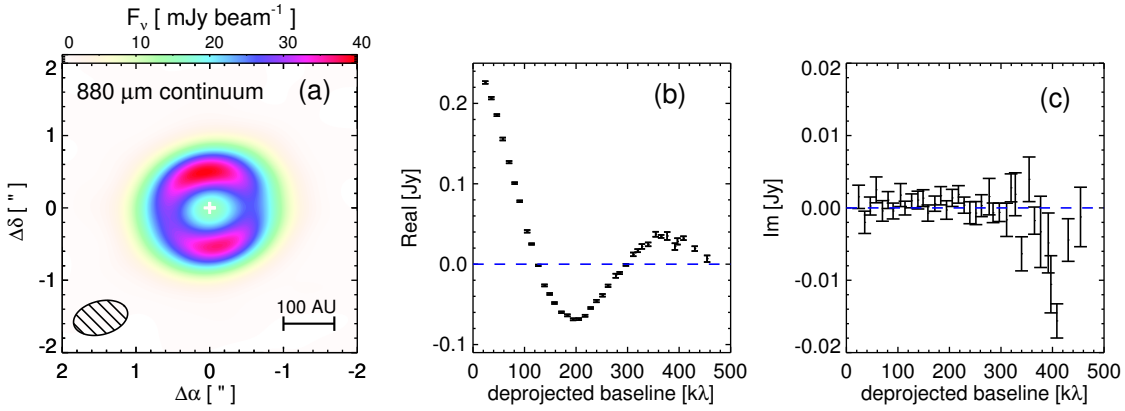


Figure 3.1 (a) 880 $\mu$m continuum map of J1604-2130. The synthesized beam, shown at lower left, has a FWHM of $0.''73 \times 0.''46$, while the wedge marks the conversion from color to surface brightness. The rms noise level is 0.18 mJy beam$^{-1}$. (b) Azimuthally averaged real part of the correlated flux as a function of deprojected baseline length, calculated by assuming a disk inclination of 6° and a position angle of -13°(Mathews et al., 2012). (c) Azimuthally averaged imaginary part of the correlated flux as a function of deprojected baseline length.

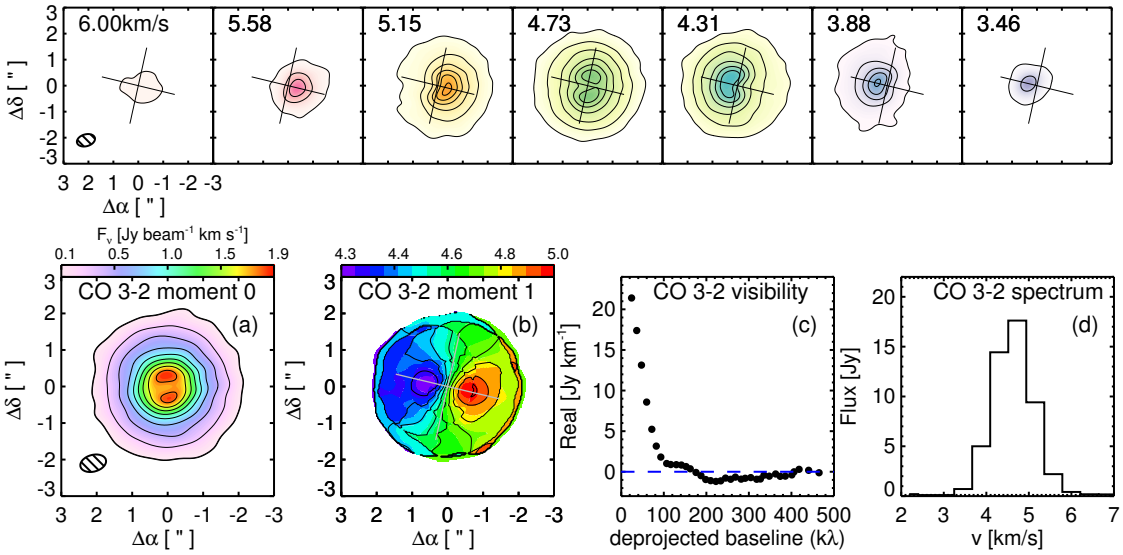


Figure 3.2 Top row: channel maps of the CO $J$ = 3-2 emission from J1604-2130. The contours begin at $3\sigma$ (45 mJy beam$^{-1}$) in each 0.42 km s$^{-1}$ wide channel and are spaced by $10\sigma$. The cross indicates the direction of the disk major and minor axes. Bottom row: The moment 0 and moment 1 maps of CO $J$ = 3-2 emission are shown in (a) and (b). Contours on the moment 0 map start at the $3\sigma$ level and increase by $10\sigma$; those on the moment 1 map are spaced by 0.08 km s$^{-1}$. (c) Azimuthally averaged CO $J$ = 3-2 emission visibilities as a function of deprojected baseline length, integrated over the seven channels plotted in the upper row. (d) CO $J$ = 3-2 spectrum of J1604-2130 integrated over a central $6''\times6''$box.

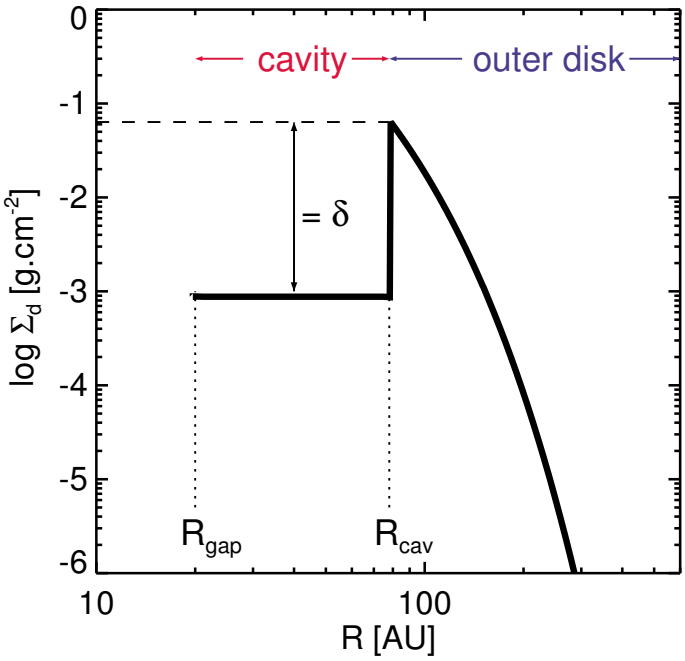


Figure 3.3 Dust surface density model. The disk is divided into three regions: the outer disk (R> $R_{cav}$) follows a similarity solution, while the surface densities inside the cavity ( $R_{gap} < R < R_{cav}$), are scaled down by a factor of $\delta$ compared to the outer disk. The innermost region of the disk ( $R < R_{gap}$) is empty.

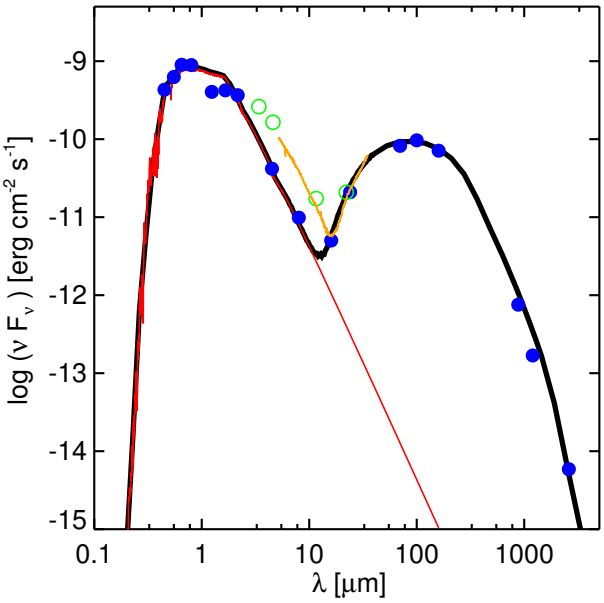


Figure 3.4 Spectral energy distribution and model (see text) for J1604-2130. The red line shows a Kurucz model atmosphere normalized to the optical and near-IR photometry. The circles are photometric data as follows: the B and R photometry are from USNO-A2.0 (Monet, 1998), V photometry is from NOMAD (Zacharias et al., 2005), and I photometry is taken from the DENIS catalogue (DENIS Consortium, 2005). The BVRI data have been de-reddened with $A_v = 0.66$ (Carpenter et al., 2014). The $2MASS$ $J, H, K$ measurements are from Cutri et al. (2003); *Spitzer* 4.5, 8 and 16 $\mu$m photometry is published in Carpenter et al. (2006). The green open circles are photometry data from WISE catalog. The discrepancy between the WISE and IRAC photometry is discussed in the text. The IRS spectra (Orange) is taken from Dahm & Carpenter (2009). The MIPS 24 $\mu$m photometry is from Carpenter et al. (2009) while the PACS 70, 100 and 160 $\mu$m data are from Mathews et al. (2013). The 880 $\mu$m data point is based on this work. The 1.2 mm point and 2.6 mm fluxes are from Mathews et al. (2012). The solid black line is the best fit model to the star+disk system.

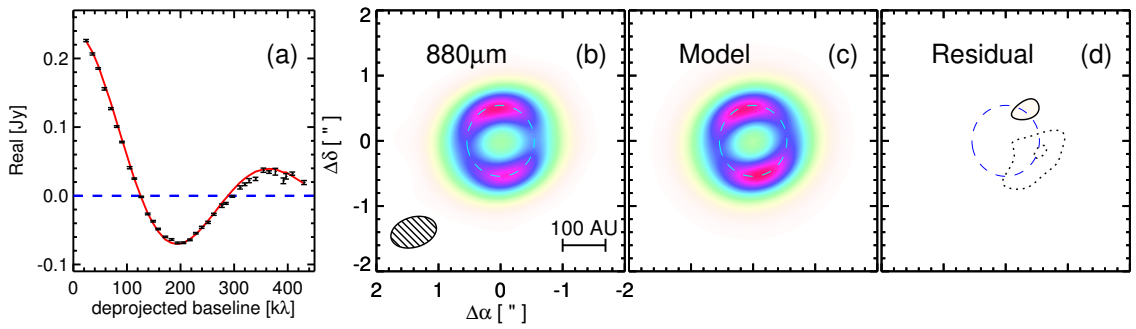


Figure 3.5 (a) Comparison of the ALMA 880 $\mu$m continuum visibility profile (black) with the synthetic model (red line) summarized in Table 3.1. (b) 880 $\mu$m continuum map of J1604-2130. The cyan dashed circle indicates the truncation radius of dust cavity ($R_{cav}$). (c) 880 $\mu$m continuum model image. (d) 880 $\mu$m continuum residual map with contours indicating 5 and 10 $\sigma$ residuals (solid contours for positive residuals and dotted contours for negative residuals).

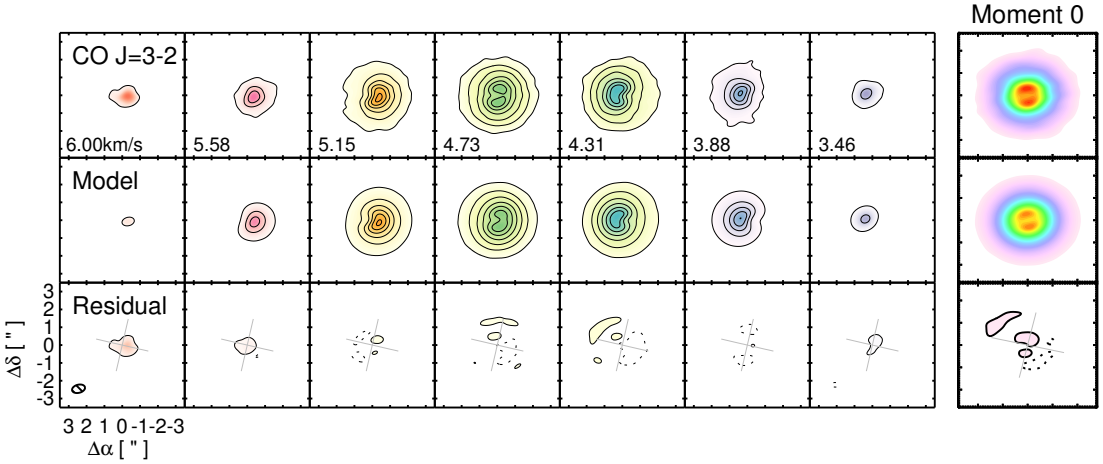


Figure 3.6 Comparison of the observed CO $J$ =3-2 channel and moment zero maps with synthetic data from the CO model. The solid contours start at 3$\sigma$ (45 mJy beam$^{-1}$) and increase at 10$\sigma$ intervals. Dashed contours indicate the -3$\sigma$ level. The color scale of the moment zero maps is the same as that in Figure 3.2 (a).

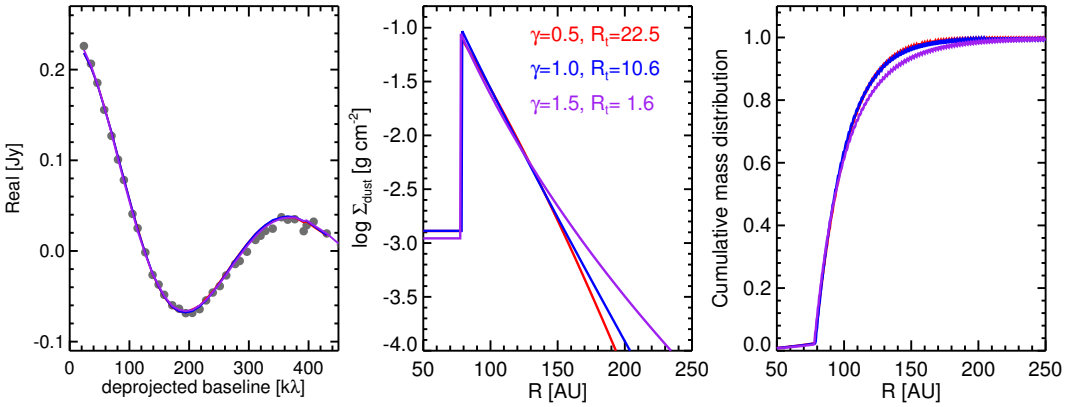


Figure 3.7 Left: Comparison of models with $\gamma = 0.5$, 1.0 and 1.5 (Table. 3.2) to the 880 $\mu$m continuum visibility profile (filled grey circles). All three models clearly produce similar fit to the data. Middle and Right: Surface mass density and normalized cumulative mass distributions of the models with the three different $\gamma$ assumed.

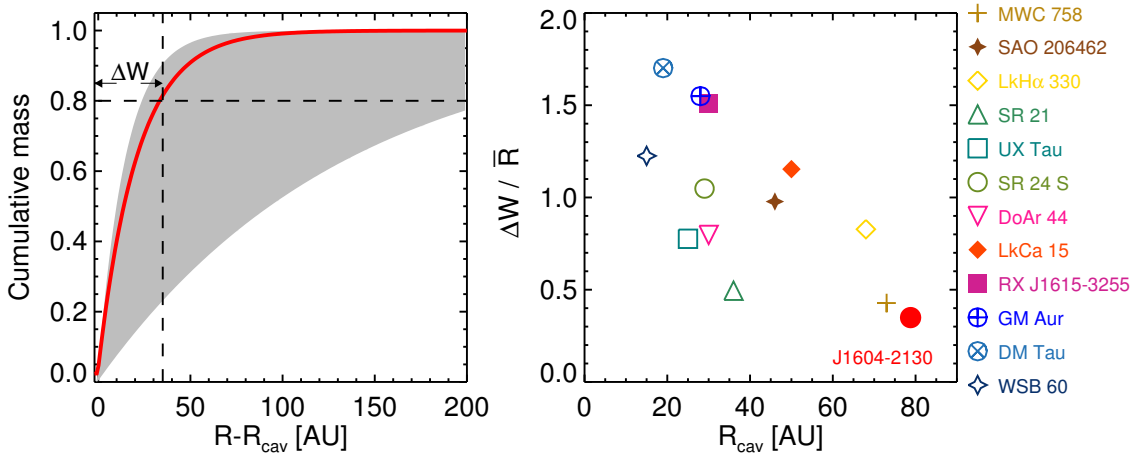


Figure 3.8 Left: The normalized cumulative mass distribution profile of J1604-2130 (red solid line) as compared to the range of distributions observed in twelve transition disks by Andrews et al. (2011) (shaded region). It can be seen that J1604-2130 has a high mass concentration beyond its dust cavity. We also illustrate the characteristic width $\Delta W$ as the width of the annulus including 80% of the disk mass. Right: Comparison of dust cavity sizes with the compactness of the dust ring in the thirteen transition disks plotted at left. The compactness of the dust ring is defined as the ratio between the width of the annulus, including 80% of the dust mass and the mean radius of the dust ring, i.e., $\Delta W/\overline{R}$. J1604-2130 has the largest dust cavity among the thirteen disks, while its mass distribution is among the most compact.

# Chapter 4

# Dimming and CO absorption toward the AA Tau protoplanetary disk: An infalling flow caused by disk instability?

Ke Zhang[1], Nathan Crockett[2], Colette Salyk[3], Klaus Pontoppidan[4], Neal J. Turner[5], John M. Carpenter[1], Geoffrey A. Blake[2]

1. Division of Physics, Mathematics & Astronomy, MC 249-17, California Institute of Technology, Pasadena, CA 91125, USA; kzhang@astro.caltech.edu

2. Division of Geological & Planetary Sciences, MC 150-21, California Institute of Technology, Pasadena, CA 91125, USA

3. National Optical Astronomy Observatory, 950 North Cherry Avenue, Tucson, AZ 85719

4. Space Telescope Science Institute, 3700 San Martin Drive, Baltimore, MD 21218, USA

5. Jet Propulsion Laboratory, California Institute of Technology, Pasadena, CA 91109, USA

*Keywords:* protoplanetary disks –stars: individual (AA Tau)–stars: pre-main sequence – stars: variables: T Tauri, Herbig Ae/Be

This chapter, with minor differences, was published in its entirety under the same title in *The Astrophysical Journal*, 2015, Volumn 805, pp. 55-61.

## 4.1 Abstract

AA Tau, a classical T Tauri star in the Taurus cloud, has been the subject of intensive photometric monitoring for more than two decades due to its quasi-cyclic variation in optical brightness. Beginning in 2011, AA Tau showed another peculiar variation – its median optical though near-IR flux dimmed significantly, a drop consistent with a 4-mag increase in visual extinction. It has stayed in the faint state since. Here we present 4.7 $\mu$m CO rovibrational spectra of AA Tau over eight epochs, covering an eleven-year time span, that reveal enhanced $^{12}$CO and $^{13}$CO absorption features in the $J_{\rm low} \leqslant 13$ transitions after the dimming. These newly appeared absorptions require molecular gas along the line of sight with T$\sim$500 K and a column density of log ($N_{^{12}CO}$) $\sim$18.5 cm$^{-2}$, with line centers that show a constant 6 km s$^{-1}$ redshift. The properties of the molecular gas confirm an origin in the circumstellar material. We suggest that the dimming and absorption are caused by gas and dust lifted to large heights by a magnetic buoyancy instability. This material is now propagating inward, and on reaching the star within a few years will be observed as an accretion outburst.

## 4.2 Introduction

Sun-like stars are born surrounded by disks which regulate the angular momentum redistribution required for accretion. It is also in these disks that planets form. Understanding the angular momentum transport and accretion processes in circumstellar disks is thus critical for our understanding of star and planet formation (Turner et al., 2014). Photometric and spectroscopic monitoring of young stars and their accretion disks is an important way to study the dynamics at play.

The classical T Tauri star AA Tau has provided many clues to the magnetospheric accretion process that channels material from the inner edge of the disk onto the central star (Bouvier et al., 1999). AA Tau shows a quasi-cyclic variation with a period of 8.5 days in its optical photometry with an amplitude of 1.4 mag in the $BVRI$ bands (Bouvier et al., 1999, 2003, 2007; Ménard et al., 2003; Grankin et al., 2007). This peculiar behavior is interpreted as a result of periodic occultations of the star by a non-axisymmetric inner disk warp, perhaps driven by a misalignment between the stellar magnetic dipole and rotation axes (Bouvier et al., 1999, 2003; Terquem & Papaloizou, 2000; O'Sullivan et al., 2005; Donati et al., 2010; Esau et al., 2014). Such occultations require that the AA Tau disk has a nearly edge-on ($i \sim 71 - 75°$) orientation, which has indeed been seen in optical scattered light images (Cox et al., 2013).

Recently, another peculiar variation was discovered (Bouvier et al., 2013). In 2011, AA Tau dimmed $\sim$ 2 - 4 mag in the $V$ band after maintaining a $V$-band magnitude between 12.3 and 14.3 mag for more than two decades (1987-2010, Grankin et al. 2007, see Figure 4.1). Its visual extinction increased by 4 mag based on the $JHK$ color changes, and AA Tau has remained in the faint state since (September 2014, current $V$-band mag=14-17, Bouvier et al. 2013, and Grankin, priv. commun.). Surprisingly, no significant change was found in the mass accretion rate onto the central star by comparing accretion tracers observed before and one year after the dimming started (based on H$\alpha$, H$\beta$ and [HeI] line fluxes, Bouvier et al., 2013). This is in contrast to other observations of disk variability, which are usually accompanied by

accretion rate changes (Sitko et al., 2012). Bouvier et al. (2013) concluded that the sudden dimming is due to additional circumstellar extinction along the line of sight and suggested that the extra extinction is possibly produced by a non-axisymmetric overdense region in the outer disk which recently moved into the line of sight via disk Keplerian rotation. Despite the importance of discovering the origin of the enhanced extinction, photometric data alone provide limited insight into the physical and dynamical properties of the extra material along the line of sight, so we turn to spectroscopy to measure gas kinematics and temperature.

Here we present new observational constraints on the origin of the dimming of AA Tau in the form of eight epochs of CO 4.7 $\mu$m spectra taken over an eleven-year time span. Significantly enhanced $^{12}$CO and $^{13}$CO absorption components are seen in the spectra taken after the dimming started, at a velocity redshifted with respect to the star. The spectra can be used to measure the properties of the absorbing gas, providing new constraints to the origin of both the dimming and absorption. Indeed, since the optical extinction and CO absorption appear at similar times, and have persisted since, the absorbing gas and obscuring dust most likely arise from the same event(s). We argue that a non-axisymmetric region in the Keplerian disk is unlikely to account for the extra absorption and velocity shift, and suggest that the enhanced extinction and extra absorption may be produced by a disk instability-driven infalling flow.

## 4.3 Observations

We carried out high resolution spectroscopic observations of AA Tau at eight different epochs between November 2003 and September 2014. Figure 1 shows the dates of the $M$-band observations, overlaid on the $V$-band photometry time series of AA Tau over the last decade. A detailed observation log is provided in Table 4.1. Most of our spectra were taken with NIRSPEC (McLean et al., 1998), a high resolution spectrometer (R$\sim$25,000) at the Keck II telescope, as part of a large NIRSPEC survey of protoplanetary disks (Blake & Boogert, 2004; Salyk et al., 2009), in both the

native seeing and adaptive optics (AO) modes. The $M$-band (4.7 $\mu$m) echelle spectra were observed with a $0.''43\times24''$ slit (native seeing observations) or a $0.''041 \times 2.''26$ slit (with AO). Two spectral settings were used, covering wavelengths between 4.65 and 5.15 $\mu$m, with gaps between orders. The total wavelength range covers a large portion of the $v$ = (1-0) fundamental rovibrational band of $^{12}$CO, i.e., the first two R-branch lines (the total angular momentum quantum number of the lower energy state $J_{\rm low}$=0,1) and the low/mid P-branch ($J_{\rm low}$=1-12 and $J_{\rm low}$=30-40), as well as an accretion tracer, the HI Pf$\beta$ transition. The AA Tau $M$-band spectrum of October 2007 is obtained from archival VLT CRIRES data, taken as part of a large survey on protostars and protoplanetary disks (Pontoppidan et al., 2011; Brown et al., 2013). The CRIRES spectrum covers a wavelength range between 4.65 and 4.77 $\mu$m at a spectral resolution of $\sim$95,000.

Objects were observed in nod pairs, with subsequent pairs subtracted from one another to remove telluric emission features. The differenced images were flat field corrected and then averaged to increase the signal-to-noise ratio. We extracted 1-D spectra from the 2-D averaged images using the optimal extraction (Horne, 1986). The wavelength calibration was derived by fitting a fourth order polynomial to the telluric emission lines within the same echelle order. Telluric absorption features were removed by dividing the AA Tau spectra by that of HR 1620 (A7 spectral type), taken close in time and airmass. To investigate the continuum flux variation with time, we compared the raw photon counts of AA Tau with those of HR 1620 in the continuum around 4.7 $\mu$m at different epochs. We found the flux ratio varied less than 30% from the midpoint of all values obtained over the past eleven years, with no apparent correlation between the continuum flux and CO emission line intensities. We thus assumed the 4.7 $\mu$m continuum is constant and flux calibrated the 1-D spectra by normalizing the continuum to the interpolated IRAC fluxes between 3.6 $\mu$m (352 mJy) and 4.5 $\mu$m (332 mJy)(Luhman et al., 2006). It is worth noting that we do not expect to detect continuum variability caused by the enhanced extinction, because an $A_V$ of 2-4 mag produces a flux change of less than 10% at 4.7 $\mu$m using a Mathis extinction law (Mathis, 1990).

Table 4.1. AA Tau Observation Log

| Obs. Date (UT) | Spectral Range ( $\mu$m) | Int. time (min) | Instrument | AO[a] |
|---|---|---|---|---|
| 2003-11-03 | 4.65-4.72, 4.95-5.03 | 12 | NIRSPEC | N |
| 2004-12-27 | 4.65-4.72, 4.95-5.03 | 12 | NIRSPEC | N |
| 2004-12-30 | 4.70-4.78, 5.02-5.09 | 8 | NIRSPEC | N |
| 2007-10-12 | 4.65-4.77 | 24[b] | CRIRES | Y |
| 2010-12-15 | 4.70-4.78, 5.02-5.09 | 64 | NIRSPEC | Y |
| 2012-12-31 | 4.65-4.72, 4.95-5.03 | 32 | NIRSPEC | Y |
| 2013-01-01 | 4.70-4.78, 5.02-5.09 | 24 | NIRSPEC | Y |
| 2013-10-19 | 4.65-4.72, 4.95-5.03 | 24 | NIRSPEC | Y |
| 2013-12-23 | 4.65-4.72, 4.95-5.03 | 24 | NIRSPEC | Y |
| 2014-09-06 | 4.65-4.72, 4.95-5.03 | 47 | NIRSPEC | N |

Note. — a: Observations with adaptive optics; b: The final spectrum combines observations with two partially overlapping spectral settings with 10 and 14 min. of integration time, respectively.

## 4.4 Results

Figure 4.2 displays our CO $M$-band spectra of AA Tau taken between November 2003 and September 2014 (data obtained within three days were consistent and merged into a single spectrum). Readily detectable $v$ = (1-0) fundamental rovibrational $^{12}$CO emission lines are seen in all eight epochs. The $^{12}$CO emission components appear to be double-peaked and spectrally resolved with an average FWHM of $\sim$130 km s$^{-1}$. The double-peaked line shape is expected for emission from a highly inclined, Keplerian disk. By fitting the CO line profile, Salyk et al. (2011) suggested the molecular emission arises from $\sim$0.1 AU. Our AO data show no CO spectro-astrometric signatures along the disk major axis to a 3$\sigma$ limit of 0.19 AU, consistent with the previous result. In five of the eight epochs, the lines were asymmetric, with the blue-shifted peak stronger than the red-shifted peak (Figure 4.3). The line-to-continuum ratio also varied significantly, from 0.15 to 0.38, but there is no apparent link between the

emission line variability and the $V$-band extinction change.

The most striking discovery is the emergence of deep, low- to moderate-$J$ $^{12}$CO ($J_{\rm low}\leq$13) and $^{13}$CO absorption below the continuum in spectra taken after the optical dimming (see Figure 4.2 and 4.3). The CO absorption components have a FWHM$\sim$14.2 km s$^{-1}$, a value close to the width of the nominal instrumental profile (FWHM$\sim$12 km s$^{-1}$). The mid-$J$ CO lines between 4.95-5.09 $\mu$m (of lower state excitation energies $E_{\rm low}$ $\sim$2000 K), however, did not show enhanced absorption after the dimming, suggesting the absorbing gas cannot be hotter than $\sim$1000 K. For all the spectra taken before the dimming, the center of the double-peaked emission line profile aligned well with the stellar velocity (heliocentric velocity $V_\star$ = 16.1$\pm$2 km s$^{-1}$, Hartmann et al. 1986). In contrast, the absorption line centers from 2011 and after show a clear and constant redshift of $\sim$6$\pm$1 km s$^{-1}$.

Because the goal of this paper is to shed light on the origin of the dimming and absorption towards AA Tau, we focus here on the properties of CO absorption lines. The varying CO emission of AA Tau will be discussed in a separate paper which investigates the variation and asymmetry of $M$-band CO emission in a large sample of disk sources (Crockett et al. 2015, in prep). We have taken additional L-band NIRSPEC observations before and after the dimming to search for additional molecules such as water in the disk gas; but the complex photospheric structure present at these wavelengths means that only very deep absorption lines would be recognized, and no such features have been found.

### 4.4.1 The physical properties of the absorbing gas

The line profiles of the absorption components are possibly varying (see Figure 4.3), but variations in the Earth's atmosphere can also mimic the line profile change since both the telluric and AA Tau features are marginally resolved, at best. Nevertheless, the line fluxes are less affected and the rotational ladder of CO $v$ = (1-0) lines provides abundant information on the physical properties of the absorbing gas. Under the assumption of a Boltzmann distribution for the rotational states, the line flux

ratios provide a direct constraint to the excitation temperature of the gas. Once the excitation temperature is known, the total column density of the absorbing gas can be derived from the absolute strengths of the absorption components.

This assumption of local thermodynamic equilibrium is reasonable in this case because the CO $v = 0, J \leqslant 13$ states are expected to be thermalized due to their moderate critical densities of $\leqslant 10^7$ cm$^{-3}$. Given the lack of constraints on the geometry of the absorbing gas, we make the simplest assumptions, i.e. the gas is isothermal and has a constant number density along the line of sight. Our model thus has three free parameters: the gas temperature $T$, the column density $N$ along the line of sight, and the intrinsic line width $\sigma$ (needed because the $^{12}$CO and $^{13}$CO absorption lines are largely spectrally unresolved at R=25,000). The line width is an upper limit to the local turbulence velocity since the absorbing gas may exist over a range of radial distances and azimuthal angles. The differential projected radial velocity from gas at different locations can broaden the line profile.

We measured the equivalent width ($W$) of each absorption line as $W = \int (I_{\rm cont} - I(v))/I_{\rm cont}\ dv$. The $^{12}$CO equivalent line widths provide a particular challenge since the absorption is built on top of emission lines. Because our goal is the study of the additional absorption that appears after the dimming, we measured the equivalent widths of the $^{12}$CO absorption from the difference between spectra, specifically those from December 2004 and January 2013, because they cover the largest wavelength range and thus provide the best constraints on the excitation temperature. Each absorption component in the residual is then fit with a Gaussian function rather than directly integrating over the line profile since certain velocities are missing in regions that overlap with saturated atmospheric lines. The gaussian fits are then divided by the continuum flux to calculate the $^{12}$CO equivalent widths, while those for $^{13}$CO were measured directly from continuum subtracted January 2013 spectra.

The theoretical equivalent width of a given transition is calculated using $I_v = I_{cont} exp(-sN_J\phi_v)$, where $N_J$ is the CO column density of a rotational state $J$, $\phi_v$ is

the intrinsic line profile, and $s$ is the integrated cross section ($\mathrm{cm^2\ s^{-1}}$), or

$$s = \frac{A_{ul}c^2}{8\pi\nu^2}\frac{g_u}{g_l}[1 - e^{-\frac{h\nu}{kT}}] \tag{4.1}$$

The spontaneous decay rate, $A_{ul}$ is taken from HITRAN (Rothman 2005), while a Voigt function is used for $\phi_v$. The Doppler width of Voigt function, $\Delta\nu_D = \sqrt{2}\sigma$, contains $\sigma$ as the third free parameter. We used an average ISM value of $^{12}$CO/$^{13}$CO number ratio of 69 to scale the column densities of $^{12}$CO to those of $^{13}$CO (Wilson, 1999).

The fit results are summarized in Figure 4.4. Our best fit has $\mathrm{T} = 494^{+192}_{-96}$ K, with a total column density of $^{12}$CO along the light of sight of $\log(\mathrm{N_{^{12}CO}}) = 18.5\pm0.1\,\mathrm{cm^{-2}}$ and an intrinsic width $\sigma$ of $2.2\pm0.1\,\mathrm{km\,s^{-1}}$. We stress that this result is not very sensitive to the input isotopic ratio; changing the $^{12}$CO/ $^{13}$CO value from 69 to 30 would result in $\mathrm{T} = 427\,\mathrm{K}$, $\log(\mathrm{N_{^{12}CO}}) = 18.1$, and $\sigma = 2.6$. The best-fit column density decreases in this case because the $^{12}$CO absorption lines are saturated and only the optically thin $^{13}$CO lines provide the main constraints on the column density. A smaller $^{12}$CO/ $^{13}$CO ratio thus produces a smaller N($^{12}$CO).

For the remaining epochs, we did not fit the three parameters ($T$, $N$, and $\sigma$) simultaneously because the available data often cover a smaller wavelength range, with many absorption lines that are heavily contaminated by saturated atmospheric absorption due to unfavorable Earth-induced Doppler shifts. Since the gas column density is most sensitive to the $^{13}$CO line strengths, we derived the CO gas column density in these epochs by fixing the $T$ and $\sigma$ parameters with the best-fit values from January 2013. In the three 2013 spectra the derived column densities of the absorbing gas vary by $\leq$30%. For the September 2014 epoch, the column density decreased to $\log(\mathrm{N^{12}CO}) = 18.2\pm0.1\,\mathrm{cm^{-2}}$, about a half of that in 2013. In the pre-dimming epochs, the October 2007 spectrum provides the most stringent column density upper limits, suggesting $\log(\mathrm{N^{12}CO}) < 17.5\,\mathrm{cm^{-2}}$ at 99% confidence ($T$ and $\sigma$ are fixed). Because the $^{13}$CO lines are optically thin, these column density changes can be directly seen in Figure 4.3.

The contemporary existence of the absorbing gas and the obscuring dust suggests that they are likely to arise from the same event(s). Assuming the gas and dust are co-spatial, we can derive an average gas-to-dust mass ratio in the absorbing material along the line of sight, by combining the $^{12}$CO column density with the increase in visual extinction associated with the dimming. Assuming a maximum fractional abundance of $n_{\rm CO}/n_{\rm H}$=$10^{-4}$ in protoplanetary disks, the total column density of absorbing gas is at least $3.2\times10^{22}$ cm$^{-2}$, resulting in a $N_{\rm H}/A_V$ $\geq$$8\times10^{21}$ cm$^{-2}$ mag$^{-1}$ – about a factor of 4 larger than the average ratio measured in nearby molecular clouds (Vuong et al 2003), suggesting a gas-to-dust ratio of $\sim$400 in the absorbing gas. Such an increased gas-to-dust mass ratio is expected if the absorbing gas at large disk heights has experienced significant dust grain growth and/or settling towards the mid-plane. The slope of the spectral energy distribution of AA Tau in (sub)mm wavelength range is consistent with the expectation of significant dust growth (Andrews & Williams, 2007).

## 4.5 The origin of the absorbing gas

The fairly sudden emergence of enhanced extinction and absorption indicates that some obscuring material recently appeared or moved into our line of sight. We argue that this new material is unlikely to be a foreground source. First, the absorbing gas is too warm ($\sim$ 500 K) compared to the typical interstellar diffuse cloud excitation temperatures of 10-100 K (Snow & McCall, 2006). Second, Bouvier et al. (2013) found that the enhanced extinction was restricted to AA Tau since three field stars nearby (projected distance between 26″and 53″) did not exhibit any luminosity variation. This projected distance is much smaller than that of a typical gas clump in molecular clouds at 140 pc. For example, the *Jeans length* of gas with T of 500 K and $N_{H_2}$ of $10^4$ cm$^{-3}$ is 1.3 pc, i.e., a projected distance of 1915″.

The absorbing gas is also unlikely to be in circumstellar envelope surrounding AA Tau because various evolutionary indicators suggest that AA Tau is a Class II object, i.e., a disk with little or no envelope (Robitaille et al., 2007). Moreover, gas in a

circumstellar envelope should be much cooler than 500 K (van Dishoeck et al., 2013).

The final possibility is that the absorbing material lies in the disk. We can place some constraints on its location based on the gas temperature of ∼500 K. Utilizing existing thermo-chemical models in the literature which are constructed for classical T Tauri disks similar to AA Tau, we can use this temperature to estimate the vertical and radial location of the absorbing gas. In the vertical direction, due to the high inclination of the disk and the optical depth of the infrared CO transitions observed, the absorbing gas must be high in the disk atmosphere but deep enough that sufficient CO column density is present in order to shield itself from photodissociation by high-energy stellar photons (Visser et al., 2009). The dominant heating sources for this warm molecular layer are X-ray and UV radiation (e.g. Glassgold et al. 2004; Gorti et al. 2011). The X-ray luminosity of AA Tau is $\sim 10^{30}$ erg s$^{-1}$ in quiescence and $\sim 10^{31}$ erg s$^{-1}$ during brief flares (Schmitt & Robrade, 2007; Grosso et al., 2007), all within the typical X-ray luminosity of classical T Tauri stars (Feigelson et al., 2005). Najita et al. (2011) computed a thermo-chemical model for classical T Tauri stars with an $L_X$ of $10^{30}$ erg s$^{-1}$. Their model shows that CO starts to survive beyond a vertical column density of $N_H \sim 10^{21}$ cm$^{-2}$. At such columns, a temperature of 500 K requires a radius that is less than 10 AU distant from the central star. Walsh et al. (2010, 2012), for example, used the X-ray, UV continuum and Ly$\alpha$ spectra of TW Hya in their thermal chemical model, and their calculations predict that the high altitude CO molecular layer inside ∼10 AU is warmer than 500 K. In summary, the warm temperature of the absorbing gas suggests a location of $\leqslant$10 AU in radius.

We conclude with a discussion of the possible origins of the suddenly enhanced extinction and CO absorptions in the AA Tau disk:

(1) *A non-axisymmetric overdense region in the disk*

Bouvier et al. (2013) suggested that the enhanced extinction is caused by a non-axisymmetric structure that recently moved into our line of sight due to Keplerian rotation. However, we argue that this scenario becomes less likely considering the CO absorption components presented here. Because the $M$-band continuum and the CO emission both arise from very small regions (R$\leq$0.5 AU), only gas and dust

located inside a small solid angle can produce the enhanced extinction and absorption. Therefore, the absorption lines should be centered at the stellar velocity. However, the CO absorption lines display a constant redshift of $\sim$6 km s$^{-1}$ over the past two years. This redshift cannot be explained by the uncertainty of the stellar velocity of AA Tau as all previous measurements of the stellar velocity are consistent within 2 km s$^{-1}$ (Hartmann et al. 1986 of 16.1$\pm$2 km s$^{-1}$, Bouvier et al. 2003 of 17.1$\pm$0.9 km s$^{-1}$ and Donati et al. 2010 of 17.2$\pm$0.1 km s$^{-1}$). A highly eccentric orbit might be able to explain the redshift, but the CO emission lines are well centered at the stellar velocity – suggesting at least the disk gas in the CO emitting region is in circular motion. If the non-axisymmetric structure rotates at Keplerian speeds, its orbital period is then at least 27 years, the total time span of AA Tau in the bright state and the duration of the dimming. Thus the structure must lie beyond $\geq$8.4 AU (assuming M$_\star$=0.8 $M_\odot$, Bouvier et al. 1999).

(2) *Inward flow driven by disk instability*

Another possibility is the absorbing material has been newly lifted to large heights due to an instability of the disk's magnetic fields, leading to an accretion outburst involving the inward transport of gas and dust. The buoyant rise of the magnetic fields generated in magneto-rotational turbulence has been demonstrated in stratified isothermal shearing-box magnetohydrodynmic calculations (Miller & Stone, 2000) and in calculations including the stabilizing effect of the external starlight heating (Hirose & Turner, 2011). In all cases, the magnetic fields dominate the pressure above about two density scale heights. The fields are erratic, with stronger activity coming in bursts, if the magnetic diffusivity is near the threshold for switching off the magneto-rotational dynamo (Turner et al. 2007, Simon et al. 2011b).

As such material propagates inward, an accretion outburst can potentially result (Zhu et al., 2010). Episodic accretion outbursts have been observed in some pre-main sequence low-mass stars (e.g. see a review by Audard et al. 2014). Well-known examples include FU Orionis objects (with typical accretion rates during an outburst of $10^{-4}$ M$_\odot$ yr$^{-1}$ and a decay timescale of $\sim$100 years) and EX Lupi objects (smaller

but more frequent outbursts with a typical outburst accretion rate of $10^{-7}$ $M_\odot$ $yr^{-1}$). Could AA Tau be a pre-FUor/EXor? AA Tau has a quiescent accretion rate between $10^{-9}$ and $10^{-8}$ $M_\odot$ $yr^{-1}$, and has shown no significant accretion rate increase since the dimming (Bouvier et al., 2013). Similarly, we did not detect significant changes in the accretion tracer HI Pf$\beta$ around 4.65 $\mu$m before and after the absorption appeared. In Section 3.1, we measured a column density in the extra gas component of $3.2\times10^{22}$ $cm^{-2}$. Assuming this gas is present in a wall at 10 AU with a scale height of 1 AU, and that this material will fall onto the star within three years, the accretion rate would rise to $\sim1.3\times10^{-7}$ $M_\odot$ $yr^{-1}$. Based on the evolutionary stage of AA Tau and our estimate of the accretion rate of the current outburst, we suggest AA Tau is unlikely to be a pre-FUor object but could be a pre-EXor candidate.

There is one additional hint that suggests episodic outbursts have previously occurred in AA Tau, in that Cox et al. (2013) found a chain of Herbig-Haro knots above the AA Tau disk in [SII] images. Such Herbig-Haro objects are usually associated with elevated accretion activity in young stars (Reipurth & Bally, 2001). The spacing of Herbig-Haro knots in the AA Tau [SII] images, together with the inferred speed of knots >200 km $s^{-1}$, suggests a time between ejections of at most a few years, which appears consistent with the smaller and more frequent outbursts in the EX Lupi type.

The observed redshift in the absorption suggests the molecular gas is propagating inward. The magnitude of the speed is, however, puzzling: 6 km $s^{-1}$ is too high for a viscous disk but too low for a free-fall velocity. With a central star of 0.8 $M_\odot$, the free-fall velocity $\sqrt{2GM_\star/r}$ is 38 km $s^{-1}$ at 1 AU. A disk with viscosity $\nu$ will evolve at radius $r$ on a timescale of $t_\nu \sim r^2/\nu$. We adopt the usual parameterization of the viscosity as $\nu = \alpha c_s^2/\Omega$ ($c_s$ is the sound speed, $\Omega$ the Keplerian angular velocity) and use the $\alpha \sim 0.1$ found in FU Ori outburst (Zhu et al., 2007) to estimate a viscous disk timescale. The radial velocity so obtained is $r/t_\nu \sim \frac{\alpha kT}{\mu m_H}\sqrt{r/GM_\star}$=$0.07\times\frac{\alpha}{0.1}\frac{T}{500\,K}(\frac{r}{AU})^{1/2}(\frac{M_\star}{0.8M_\odot})^{-1/2}$ km $s^{-1}$.

The instability driven inward flow scenario is speculative since certain critical disk physical parameters, such as the magnetic field and viscosity, are largely unknown. Monitoring the physical properties of the absorption components and the accretion

rate over the next few years will provide crucial constraints on the origin of the optical dimming. With a radial velocity of 6 km $s^{-1}$, matter within 10 AU from the central star (T$\sim$500 K) should drive an accretion rate increase over the next few years if the absorption lines are caused by infalling gas. Any subsequent outburst's accretion rate and duration combined would yield the amount of material involved, while the duration of the absorption would suggest a location for the triggering instability. Furthermore, assuming the inflowing material rotates at near-Keplerian velocities, the duration of the absorption constrains the azimuthal extent of the absorber. For example, at a distance of 5 AU, the three-year ongoing absorption suggests an angular extent of at least 90 degrees. In short, the dimming and absorption observed in AA Tau may contain important clues into the transport processes in disks.

## 4.6 Acknowledgments

We thank Jerome Bouvier and Konstantin Grankin for sharing their AA Tau photometric data. KZ, NC, and GAB gratefully acknowledge support from the NSF AAG and NASA Origins of Solar Systems programs. CS acknowledges the financial support of the NOAO Leo Goldberg Fellowship program. NJT's contributions were made at the Jet Propulsion Laboratory, California Institute of Technology, under contract with NASA and with support from Origins of Solar Systems Program grant 13-OSS13-0114. JMC acknowledges support from NSF award AST-1140063. The spectra presented herein were obtained at the W. M. Keck Observatory, which is operated as a scientific partnership among the California Institute of Technology, the University of California, and NASA. The Observatory was made possible by the generous financial support of the W. M. Keck Foundation. The VLT data presented were acquired under program ID 179.C-0151. Finally, the authors wish to acknowledge the significant cultural role of the summit of Mauna Kea.

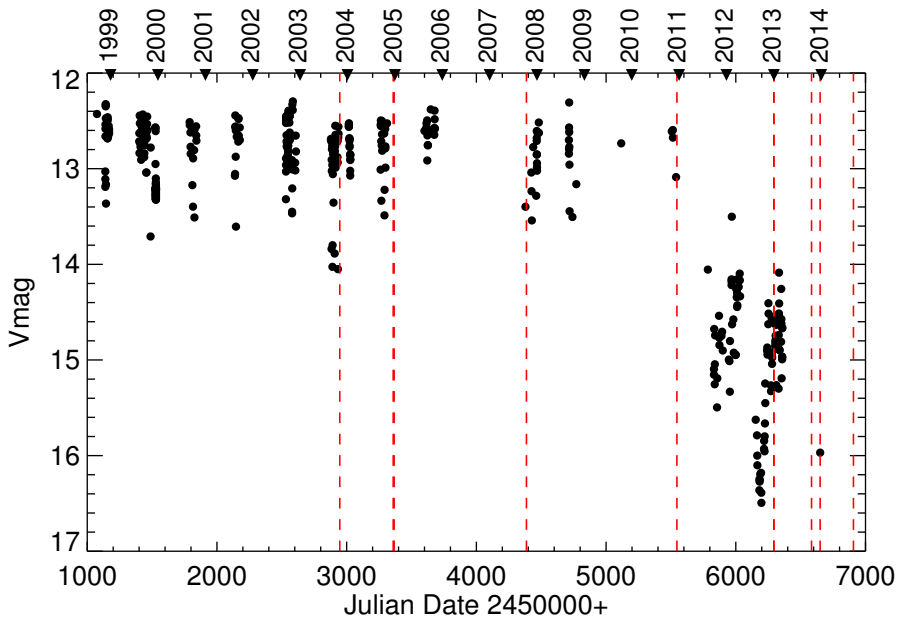


Figure 4.1 $V$-band photometry time series of AA Tau (Bouvier et al., 2013) overlapped with observational dates of CO $M$ band spectra (red vertical dash lines). The 2013 December photometry data are from Grankin and Bouvier (priv. commun.).

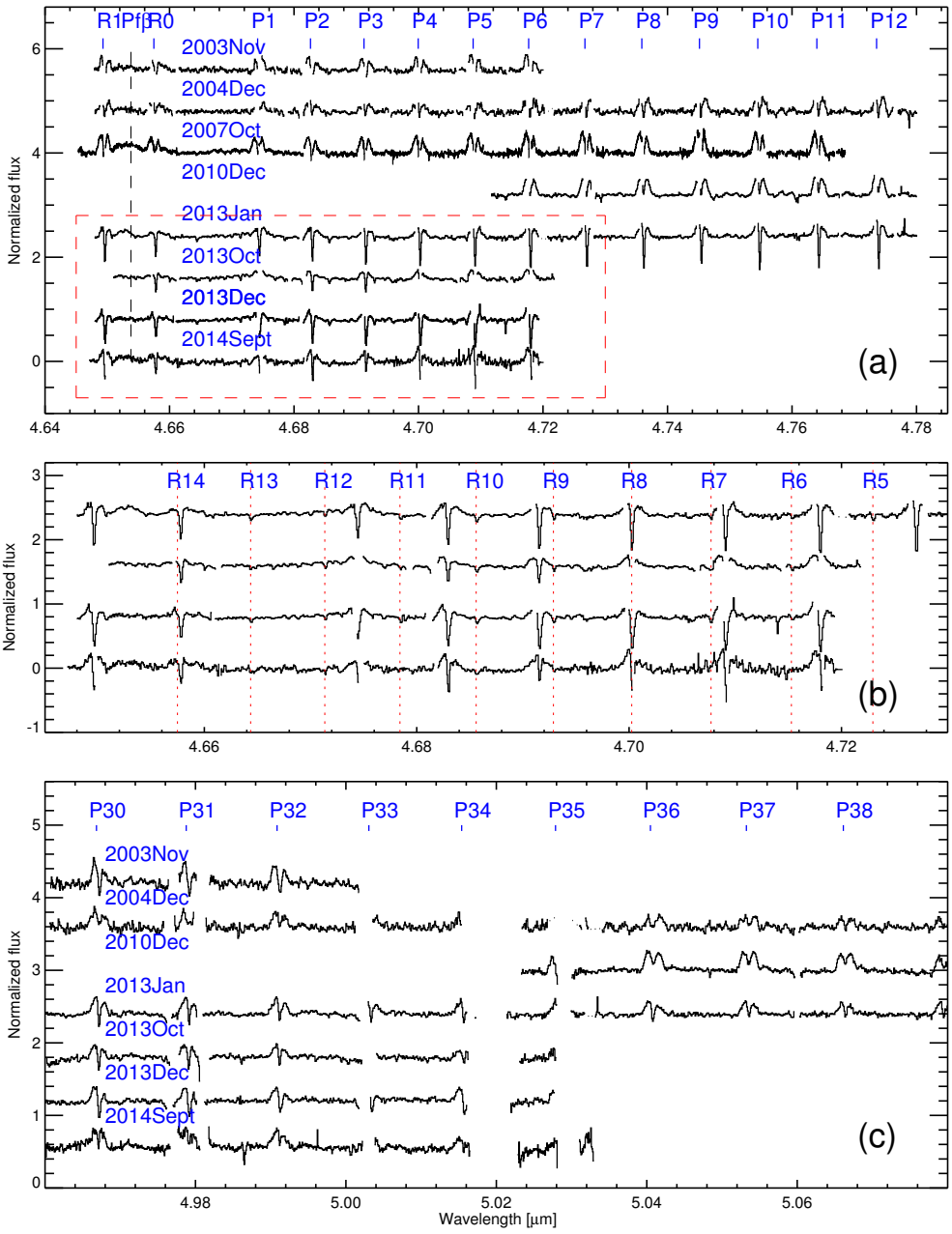


Figure 4.2 CO $M$-band spectra of AA Tau before and after the 2011 $V$-band dimming. (a) CO rovibrational spectra between 4.64 and 4.78 $\mu$m. The blank regions represent regions with telluric transmission <25%, which we have masked out due to high noise levels. The rest wavelengths of the $^{12}$CO transitions are marked as small vertical lines at the top of the panel. The region highlighted by the dashed box is enlarged in panel (b). (b) A close up of the 4.64-4.73 $\mu$m region, highlighting the $^{13}$CO absorption lines that appear after 2011. Rest wavelengths of the $^{13}$CO $v$= 1-0 lines are marked with dashed lines. (c) High-$J$ CO spectra between 4.95 and 5.09 $\mu$m.

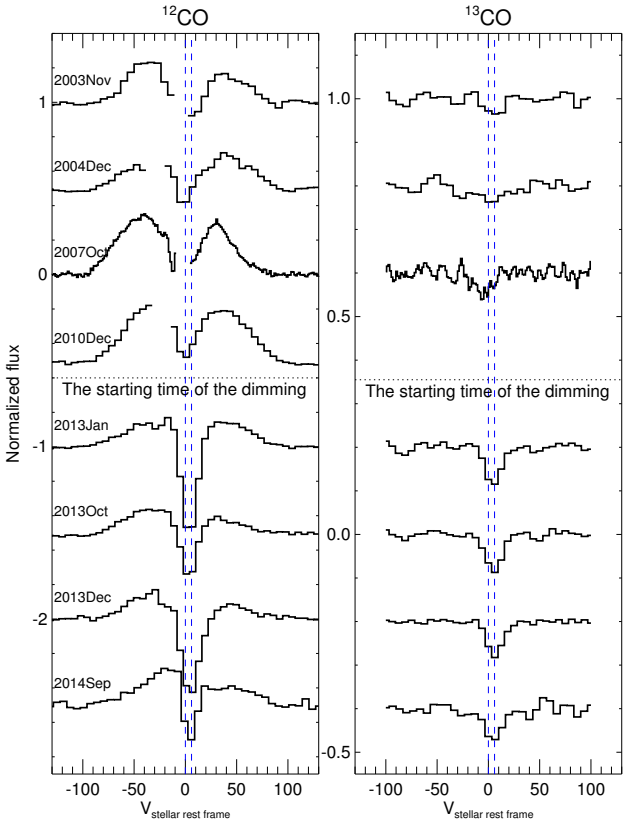


Figure 4.3 Time variation in the low-$J$ $^{12}$CO and $^{13}$CO line shape(s). The average $^{12}$CO line shape of each epoch combines the $^{12}$CO $v$ =(1,0) $J_{\rm low}$ $\leqslant$12 lines, that for $^{13}$CO averages the isolated from $^{13}$CO R12 and 13 lines. There is no $^{13}$CO line profile for December 2010 epoch because the spectra do not include the two $^{13}$CO transitions. All of the lines are normalized to the continuum flux. The two vertical dashed lines indicate the locations of stellar velocity and a red shift of 6 km s$^{-1}$. The horizontal dotted lines denote the onset of dimming in 2011.

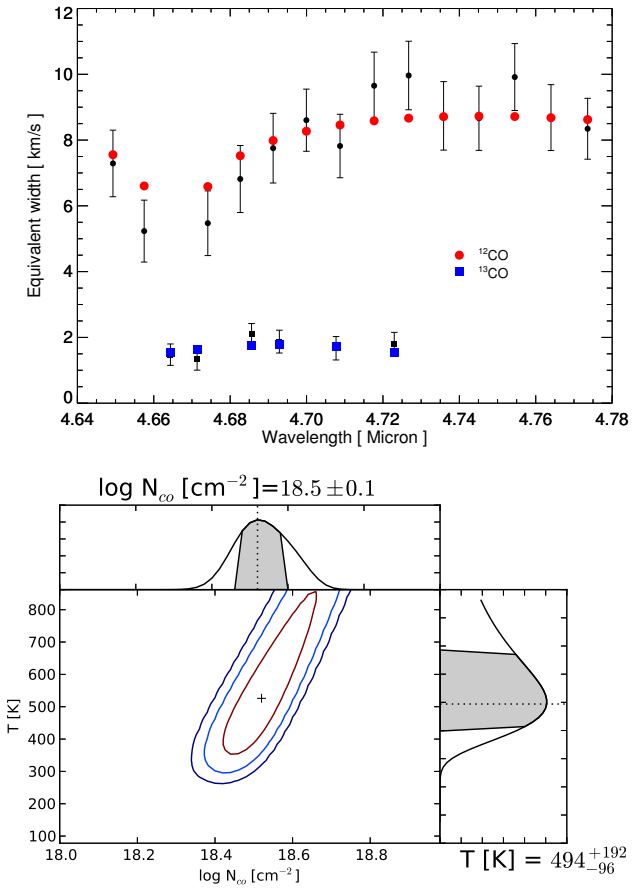


Figure 4.4 *Top:* Best model of the equivalent widths of the $^{12}$CO and $^{13}$CO absorption components in January 2013. Error bars indicate the $1\,\sigma$ uncertainties, filled circles $^{12}$CO (black ones are data points and red circles are best model fitting results), filled squares $^{13}$CO (the data points are in black while the model results are in blue). *Bottom:* Probability distribution surface contours of T and $N_{^{12}CO}$, at 68%, 95%, 99% confidence levels. Marginalized one dimensional posteriors are shown on each side. The shaded regions depict the 68% confidence areas.

# Chapter 5

# Evidence of fast pebble growth near condensation fronts in the HL Tau protoplanetary disk

Ke Zhang[1], Geoffrey A. Blake[2], Edwin A. Bergin[3]

1. Division of Physics, Mathematics & Astronomy, MC 249-17, California Institute of Technology, Pasadena, CA 91125, USA; kzhang@astro.caltech.edu

2. Division of Geological & Planetary Sciences, MC 150-21, California Institute of Technology, Pasadena, CA 91125, USA

3. Department of Astronomy, University of Michigan, 500 Church Street, Ann Arbor, Michigan 48109, USA

*Keywords:* astrochemistry – stars: premain-sequence – stars: individual (HL Tau) – protoplanetary disks – planets and satellites: composition

This chapter, with minor differences, has been accepted for publication in *The Astrophysical Journal Letters* in its entirety under the same title.

## 5.1 Abstract

Water and simple organic molecular ices dominate the mass of solid materials available for planetesimal and planet formation beyond the water snow line. Here we analyze ALMA long baseline 2.9, 1.3, and 0.87 mm continuum images of the young star HL Tau, and suggest that the emission dips observed are due to rapid pebble growth around the condensation fronts of abundant volatile species. Specifically, we show that the prominent innermost dip at 13 AU is spatially resolved in the 0.87 mm image, and its center radius is coincident with the expected mid-plane condensation front of water ice. In addition, two other prominent dips, at distances of 32 and 63 AU, cover the mid-plane condensation fronts of pure ammonia or ammonia hydrates and clathrate hydrates (especially with CO and $N_2$) formed from amorphous water ice. The spectral index map of HL Tau between 1.3 and 0.87 mm shows that the flux ratios inside the dips are statistically larger than those of nearby regions in the disk. This variation can be explained by a model with two dust populations, where most of solid mass resides in a component that has grown into decimeter size scales inside the dips. Such growth is in accord with recent numerical simulations of volatile condensation, dust coagulation, and settling.

## 5.2 Introduction

The frost lines of abundant ices have long been thought to be important for planet formation, in part because the extra material provided by condensation can significantly enhance the local mass surface density of solids in the disk (Hayashi, 1981; Stevenson & Lunine, 1988; Desch, 2007). This in turn significantly shortens the time scale needed to form protoplanets in core-accretion models (Pollack et al., 1996). Furthermore, the bulk composition of terrestrial planets and the cores of gas or ice giants is determined by that of the planetesimals from which they are built. Because volatility is highly species specific, it is the condensation fronts of the principal solid-vapor reservoirs in the mid-plane of protoplanetary disks that set the rough boundaries of planetesimals with different compositions (Öberg et al., 2011).

Recent experiments and numerical simulations of dust coagulation and settling suggest that condensation fronts may play a crucial role in planetesimal formation via two aspects: first, the growth efficiency of dust grains is composition dependent. Lab experiments show that icy aggregates are significantly more 'sticky', and resistant to compaction than silicate aggregates (Güttler et al., 2010; Seizinger & Kley, 2013; Kelling et al., 2014). The second, perhaps more important, aspect is that the enhanced local surface mass density near snow lines may produce pressure bumps, high dust-to-gas mass ratios, or viscosity gradients, thus triggering instabilities that form planetesimals (Kretke & Lin, 2007; Ros & Johansen, 2013; Bitsch et al., 2014; Drążkowska & Dullemond, 2014).

Despite the wealth of theoretical predictions concerning condensation fronts in disks, no direct observations of fast dust growth near such fronts have been carried out. The small angular separation and emitting areas of such zones, even in the nearest protoplanetary disks, make such observations challenging. ALMA, with its unprecedented spatial resolution and sensitivity, is changing this situation dramatically. Young, actively accreting objects are good initial targets because their luminosities and disk temperature profiles move the condensation fronts out to larger, resolvable, distances (Kennedy & Kenyon, 2008; Blake & Bergin, 2015).

HL Tau, a young star in the Taurus molecular cloud ($\sim 10^5$ yr), was recently observed by ALMA at 2.9, 1.3, and 0.87 mm with a spatial resolution as good as 3 AU (Partnership et al. 2015, APR henceforth). Here we propose that the dark concentric rings observed in the (sub)mm interferometry of HL Tau are due to fast pebble growth near condensation fronts. We first characterize the location and width of surface brightness dips in the ALMA images before comparing their location with the expected condensation fronts in the mid-plane of the disk. We then examine the dust properties in the dips to determine if they are consistent with pebble growth.

## 5.3 Observations

The ALMA Band 3, 6, and 7 (or wavelengths of 2.9, 1.3 and 0.87 mm, respectively) HL Tau observations were carried out in 2014, as part of its long-baseline commissioning and science verification (SV) program. With longest baselines of 15.2 km, the HL Tau observations achieved exceptional spatial resolution, with beam sizes of 11.9×8.6 AU, 4.9×3.1 AU and 4.2×2.7 AU at 2.9, 1.3 and 0.87 mm (for an adopted distance of 140 pc). More detailed descriptions of the data and calibration can be found in APR, who demonstrated the HL Tau continuum images are ∼axisymmetric and well fit with a series of elliptic rings. Therefore, a first order approximation of the HL Tau surface brightness is a single parameter function of the distance from the star.

For our purposes, it is much easier to work on deprojected, circular images. We thus start with the calibrated measurements, and use CASA v4.3 (McMullin et al., 2007) to deproject the visibility data and generate synthesized images for all three bands. Assuming the peak continuum emission represents the location of the central star, we first shift the phase center of each band to that of HL Tau (by $\Delta_\alpha = -14$ mas, $\Delta_\delta = 196$ mas). We then deproject the visibility data using the best-fit inclination angle $i = 46.72°$ and PA = 138.02° from APR.

From the deprojected visibility data in bands 6 and 7 we have also generated a spectral index ($\alpha$, where $I_\nu \propto \nu^\alpha$) map. This result is computed using the CLEAN task with nterms=2, based on the multi-frequency deconvolution algorithm developed

by Rau & Cornwell (2011).

## 5.4 Charactering the emission dips

We measure the surface brightness versus radial distance in steps of 0.5 AU, and present the azimuthally averaged radial brightness distributions in Figure 5.1. The most consistent features in all the bands are three emission depressions, or dips, around ∼13, 32 and 63 AU. We note that there are many subtle bumps in the surface brightness distribution, and we refer interested readers to a more detailed description by APR. Here we focus on the three most prominent, ∼radially-symmetric dips.

In order to constrain the dip widths and depths, a smooth fit to the surface brightness distribution is needed. We use a simple vertically isothermal model,

$$I_\nu(r) = \cos i \times B_\nu(T_r)(1 - e^{-\Sigma(r)\kappa_\nu \sec i}) \quad (5.1)$$

$$T_r = T_0(r/[1\mathrm{AU}])^q \quad (5.2)$$

$$\Sigma(r) = \Sigma_c(r/r_c)^{-\gamma}\exp[-(r/r_c)^{2-\gamma}] \quad (5.3)$$

where $I_\nu$ is the surface brightness (Jy arcsec$^{-2}$), $i$ the inclination angle, $\kappa_\nu$ the continuum opacity in cm$^2$ g$^{-1}$, and $\Sigma(r)$ the dust+gas mass surface density distribution for a steady accretion disk (Pringle, 1981; Andrews et al., 2009). The $\cos i$ factor in eq. (1) accounts for the effects of the deprojection on the synthesized beam.

Since our goal is to produce a smooth fit to the surface brightness distribution rather than a realistic physical model, we use $\kappa_\nu = 0.01\,\mathrm{cm}^2\,\mathrm{g}^{-1}(\nu/230[\mathrm{GHz}])$ throughout the disk (Ossenkopf & Henning, 1994).

The results of the best-fit models are plotted as dashed lines in Figure 5.1. We then divide the observed $I_\nu(r)$ with the best-fit model in each band to constrain the shape of the dips, see Figure 5.1 (b). The locations are consistent with those of the dark rings reported in APR. The 13 AU and 32 AU intensity dips appear to be highly symmetric. Gaussian fits to the normalized radial brightness profile are listed in Table 5.1. The 63 AU dip is asymmetric, so we only list the radius of the minimum

Table 5.1. Parameters of the dips, normalized to the local continuum

| band | ind | Center [AU] | FWHM [AU] | Amplitude |
|---|---|---|---|---|
| band 7 | 1 | 12.6±0.1 | 7.2±0.3 | 0.56±0.02 |
| 3.0×5.5 AU | 2 | 32.2±0.4 | 5.3±1.0 | 0.26±0.05 |
| | 3 | 63.5 | 17.7 | 0.44 |
| band 6 | 1 | 12.7±0.2 | 7.4±0.3 | 0.66±0.03 |
| 3.3×6.6 AU | 2 | 32.2±0.3 | 6.9±0.6 | 0.41±0.04 |
| | 3 | 64.0 | 18.0 | 0.52 |
| band 3 | 1 | 13.6±0.3 | 10.4±0.4 | 0.39±0.03 |
| 9.1×15.1 AU | 2 | 32.4±0.6 | 11.1±1.5 | 0.22±0.03 |
| | 3 | 66.0 | 16.8 | 0.45 |

and the dip FWHM. The FWHM of the 13 and 32 AU dips are $5-7$ AU, about $2\times$ the minor axis of the synthesized beams at 1.3 and 0.87 mm, indicating that the dips are spatially resolved. The 63 AU dip is resolved at all bands, with a FWHM of 17-18 AU. The minimum surface intensity of the dips range from 37% to 78% that of the smooth continuum from the best-fit models.

## 5.5 Condensation fronts of major volatiles in protoplanetary disks

To check if the dark rings/dips in the ALMA HL Tau images are correlated with condensation fronts, we calculate the condensation temperatures of major ice species under realistic pressure ranges and compare them with the expected disk mid-plane temperature distribution.

Here we consider the major condensible carriers of these elements based on the composition of comets, which are believed to be the best representatives of primordial icy materials in the Solar Nebula (Mumma & Charnley, 2011). We include $N_2$, one of the major carriers of N as predicted by chemical models of disks (Schwarz & Bergin, 2014). As a homonuclear diatomic, $N_2$ cannot be directly measured in cometary

comae.

For "pure"(single component) ices we define the condensation temperature of species $i$ as that where the thermal desorption and accretion rates are equal, i.e.,

$$n^i_{\rm ice} \times k^i_{\rm desorp} = n^i_{\rm gas} \times k^i_{\rm accr} \quad , \tag{5.4}$$

where $k^i_{\rm desorp}$ and $k^i_{\rm accr}$ are calculated using the treatment outlined in Woitke et al. (2009) and Walsh et al. (2010).

Besides pure ices, we also consider clathrate hydrates, special forms of (water) ice found in large quantities on the Earth and that have been postulated to be important in the outer Solar System. These are crystalline water-ice compounds in which gaseous molecules can be trapped inside the lattice cages of the ice. At typical mid-plane disk pressures, abundant volatiles such as methane, $H_2S$, CO and $N_2$ are expected to be trapped in the form of clathrate hydrates before they condense as pure ice species, given a sufficiently large water ice surface area to which the vapor has access (Lunine & Stevenson, 1985). This interesting feature of clathrate hydrates has been employed to explain the low N/O elemental ratio observed in comets as compared to that of the Sun's photosphere (Iro et al., 2003), and the existence of methane in Titan's atmosphere (Lewis, 1971).

A summary of the condensation temperatures of pure ice species from such calculations is shown in Table 5.2, along with the condensation temperatures of clathrate hydrates from Lunine & Stevenson (1985) and Iro et al. (2003). Our condensation temperatures are consistent with the results of Pollack et al. (1991) over the same pressure range. Table 5.2 shows that most of the clathrate hydrates can be created at higher temperatures than their pure ice condensates. The exceptions are $NH_3$, which has a very similar temperature for its hydrate and pure ice forms, and $CO_2$, which condenses as a pure frost at higher temperatures than for which the clathrate is stable.

In Figure 5.2 we compare the dip radii with the expected disk condensation front locations. In this figure we plot the observed brightness profile, which provides a

Table 5.2. Condensation temperatures of the major volatiles in disks

| Species | $T^{a}_{cond}$ (K) | $E_b$ (K) | Cometary Abundance % of $H_2O$ | Ref |
|---|---|---|---|---|
| $H_2O$ | 128 - 155 | 5165 | 100 | 1, 5 |
| CO | 23 - 28 | 890 | 0.4 - 30 | 1, 5 |
| $CO_2$ | 60 - 72 | 2605 | 2 - 30 | 1, 5 |
| $CH_4$ | 26 - 32 | 1000 | 0.4 - 1.6 | 2, 5 |
| $CH_3OH$ | 94 - 110 | 4355 | 0.2 - 7 | 1, 5 |
| $N_2$ | 12 - 15 | 520 | ··· | 2, 5 |
| $NH_3$ | 74 - 86 | 2965 | 0.2 - 1.4 | 1, 5 |
| HCN | 100 - 120 | 4170 | 0.1 - 0.6 | 3, 5 |
| $H_2S$ | 45 - 52 | 1800 | 0.1 - 0.6 | 4, 5 |
| $NH_3{\cdot}H_2O$ | 78 - 81 | ··· | ··· | 6 |
| $H_2S^{\star}$ | 77 - 80 | ··· | ··· | 6 |
| $CH_4^{\star}$ | 55 - 56 (69-72) | ··· | ··· | 6,7 |
| $CO^{\star}$ | 45 - 46 (58-61) | ··· | ··· | 6,7 |
| $N_2{}^{\star}$ | 41 - 43 (55-57) | ··· | ··· | 6 |

Note. — a. Condensation temperature ranges for ices corresponding to gas number densities of $10^{10}$- $10^{13}$cm$^{-3}$, suitable for disk mid-planes. * Condensation temperatures of clathrate hydrate formed from hexagonal ice or hydrate under gas number densities of $10^{12}$- $10^{13}$cm$^{-3}$. The values in parentheses are for clathrates formed from amorphous ice.

References: (1) Martín-Doménech et al. (2014), (2) Luna et al. (2014), (3) Sandford & Allamandola (1993), (4) Hasegawa & Herbst (1993), (5) Mumma & Charnley (2011), (6) Iro et al. (2003), (7) Lunine & Stevenson (1985)

rigorous lower bound to the dust temperature. The actual physical temperature in this embedded disk can be larger in the case of either optically thin dust emission (likely in the outer disk) or significant grain coagulation. As a more detailed estimate of the HL Tau mid-plane temperature structure we follow Men'shchikov et al. (1999) (MFH henceforth), who used two-dimensional radiative transfer models to quantitatively match the available spectral energy distribution, intensity, and linear polarization data on HL Tau from near IR to (sub)mm wavelengths. Their best-fit model results in $T_{mid} = 665\ (r/\mathrm{AU})^{-0.6}\,\mathrm{K}$ for the mid-plane temperature distribution. This is greater than that estimated from the observed brightness distribution in the ALMA image, at all radii. Interestingly, as Figure 5.2 shows the dips overlap nicely with the condensation fronts of the most abundant volatiles using the MFH profile: pure water condenses around the 13 AU dip, while pure $NH_3$ or ammonia (and hydrogen sulfide) hydrates condense around the 32 AU dip. At further distances, the condensation front of pure $CO_2$ and the onset of the CO and $N_2$ clathrate hydrate stability fields, from an amorphous water ice seed occurring near the 63 AU dip.

## 5.6 Dust properties inside the dips

We have shown above that the most prominent dips in the HL Tau images are remarkably close to the expected condensation fronts of abundant volatiles. We now investigate the dust properties across these radii.

At (sub)mm wavelengths, the spectral index $\alpha$ of the surface brightness (where $I_\nu \propto \nu^\alpha$) is a widely-used observable to characterize dust properties in protoplanetary disks (Natta et al., 2007). For optically thin dust emission, $\alpha$ can be expressed as $\alpha$=2+$\beta$, where $\kappa_\nu \propto (\nu/\nu_0)^\beta$. The value of $\beta$ is sensitive to the maximum dust size, $a_{\mathrm{max}}$, for a given a size distribution, $n(a) \propto a^q$. If the emission is optically thick, however, $\alpha$=2 (the blackbody limit) and information on the dust size is lost.

APR provided a cross-cut of $\alpha$ along the major axis of the as-observed image; but it is not clear if this cross-cut is representative of the full disk. In Figure 5.3, we show the radial distribution of $\alpha$, measured between 1.3 and 0.87 mm, in crosscuts

at $\theta$ = 0, 45, 90 and 135° (starting from west) along with the azimuthally averaged $\alpha(r)$. Despite large azimuthal variations, there is a clear general pattern: inside of 48 AU $\alpha\sim2$, except for increases to values of $\sim$2.6 and $\sim$2.4 at the 13 AU and 32 AU dips, respectively. Outside 48 AU, $\alpha$ gradually increases from 2 to 2.7 and then becomes relatively flat, except for two shallow decreases around 70 and 80 AU near local maxima in the surface brightness.

One way to explain $\alpha\sim2$ invokes optically thick dust emission in the inner disk, while that in first two dips is optically thin with $\alpha=\beta+2$. This explanation faces two difficulties. First, a massive disk is needed to create optically thick mm-continuum with modest grain growth. Given a typical continuum opacity of $\kappa_\nu$=0.01 cm$^2$ g$^{-1}$($\nu$/[230GHz]), a surface density of $\Sigma_{\rm gas}$=100 g cm$^{-2}$ at 48 AU is needed to reach $\tau_{1.3\,\rm mm}$ = 1 – a value 20× larger than that for the MMSN (Hayashi, 1981). The second issue is the large discrepancy between the temperature derived from SED fits (the MFH model) and the observed brightness temperature (Figure 5.2). These should be nearly equal if the mm-dust emission is optically thick.

An alternative explanation for $\alpha\sim2$ that mitigates these difficulties is a scenario where the dust emission for $R \lesssim$48 AU is effectively optically thin, but with $\beta\sim$ 0. This can occur when dust grains grow to sizes ($a$) larger than the observational wavelength ($\lambda$). Under such conditions, the absorption cross section simply equals the particle geometric cross section – and is thus independent of wavelength. Such significant dust growth is likely in the dense inner disk, considering that grains beyond 48 AU have grown to $\geq$mm sizes ($\alpha$=2.77±0.13 (APR)). This dust growth scenario, however, also faces a problem: for a single dust size-distribution, $\alpha > 2$ within the 13/32 AU dips demands smaller dust (and reduced mass surface densities) at these radii. It is difficult to understand why the disk inside of and, particularly beyond, the 13 and 32 AU dips should have experienced more extensive dust growth than the dense inner regions of the disk.

We suggest the apparent contradiction in the dust growth scenario can be solved by a model with two dust populations. This model differs from the commonly invoked power law size distribution but is commonly encountered in numerical simulations of

dust growth (e.g. Dullemond & Dominik 2005, Drążkowska & Dullemond 2014). Our first dust population has intermediate growth and a dust opacity of $\kappa_{\rm dust1,\nu}$, while the second population has grown to an average size for which $a \gg \lambda$. Thus:

$$\kappa_{\rm dust1,\nu} = \kappa_1 (\frac{\nu}{\nu_0})^{\beta_1} \quad (5.5)$$

$$\kappa_{\rm dust2,\nu} = \frac{\pi \bar{a}^2}{4/3 \pi \rho \bar{a}^2} = \frac{3}{4\rho}\frac{1}{\bar{a}} \quad (5.6)$$

$$\kappa_{\rm dust,\nu} = (1-f)\kappa_{\rm dust1,\nu} + f\kappa_{\rm dust2,\nu} \quad (5.7)$$

where $\bar{a}$ and $f$ are the average dust size and mass fraction of the second dust population, and $\rho$ is the physical density of the dust.

A plausible order of magnitude estimate can be found if we assume $\kappa_{\rm dust1,\nu} = 1$ cm$^2$ g$^{-1}(\nu/[230{\rm GHz}])$, or dust grain growth to mm size. For the second population, we assume $\rho$=1 g cm$^{-3}$, that is, ice dominated grains, and $\kappa_{\rm dust2,\nu}$ =0.75$(\bar{a}/[{\rm cm}])^{-1}$ cm$^2$ g$^{-1}$. We further adopt $f$=0.9, i.e., 90% of the dust mass in the second dust population. For modest optical depths in the first population, the overall value of $\alpha$ between 1.3 and 0.87 mm changes with $\bar{a}$ (Figure 5.3 f). For $\bar{a}$ near 1 cm, the cm-sized dust dominates the opacity and leads to $\alpha\sim$ 2. When $\bar{a}$ grows to decimeter-size, the mm-sized grains (population 1) dominate the mass specific dust opacity, even though they contain a small fraction of the dust+ice mass, and $\alpha$ becomes significantly greater than 2.

Thus, with significant dust aggregation in the second population, the flux and $\alpha$ behavior in the dips can be explained. With modest mass surface densities, the fractional area of a given column of the disk covered by the dust becomes <unity, and the brightness temperature drops below the physical temperature even though individual dust aggregates are optically thick. Further (sub)mm to cm high resolution continuum images can distinguish between these two dust/disk structure scenarios through more accurate constraints on the $\alpha(r)$ distribution, as can direct measurements of the vertical and radial gas temperature distributions via molecular emission.

## 5.7 Discussion

The analysis presented above demonstrates that the location of the three most prominent dips in the HL Tau (sub)mm interferometric images are coincident with the expected condensation fronts of the main volatiles, using the mid-plane temperature distribution derived from observations. Further, the spectral index variation inside the dips can be explained by a bimodal dust size distribution model without the need to invoke significant surface mass density depletions.

From our simple order of magnitude model, we infer that most of the dust mass needs to reside in a population that has grown to decimeter size scales inside the 13 and 32 AU dips. Ros & Johansen (2013) showed that near the water condensation front dust growth from millimeter to at least decimeter-sized pebbles is possible on a time scale of only 1000 years. This rapid growth is consistent with young age of HL Tau, between 0.1 and 1 Myr (Beckwith et al., 1990; Robitaille et al., 2007).

To date, the numerical simulations for dust growth around condensation fronts have considered only water. It is unclear if pebble growth is sufficiently rapid around other condensation fronts to explain the HL Tau results. The extra solid material delivered by clathrate hydrates cannot significantly enhance the solid mass surface density as does $H_2O$ at the water snowline, since each host molecule needs $\sim$ six water molecules to form the cage structure. The condensation fronts of pure $CO_2$ and CO are potentially more important for enhancing mass surface density since they account for $\sim$30% of water abundance in comets. Nevertheless, the model used by Ros & Johansen (2013) can in principle to be applied to other condensation fronts. Clathrate hydrate formation, perhaps driven by the transient warming of amorphous ice (Blake et al. 1991) via accretion bursts, can alter the ice rheology. Changes to the sticking efficiency, porosity and compaction of dust+ice aggregates may thus be central to triggering rapid pebble growth in the outer disk.

Once a critical decimeter-sized pebble population is formed, streaming instabilities can drive the creation of >km-sized planetesimals (Johansen et al., 2014). If fast pebble growth does preferentially occur around the condensation fronts of abun-

dant volatiles, this would suggest that snow lines regulate the formation and chemical composition of 1-100 km planetesimals, and ultimately the formation and bulk composition of planets.

As the disk evolves the location of condensation fronts will shift inward, perhaps countered by the effects of episodic accretion. How this might affect dust evolution is uncertain (Hubbard & Ebel, 2014). Nonetheless, the possibility that disks such as that encircling HL Tau might be seeded with pebbles suggests that planetesimal formation might occur during early evolutionary stages. This is consistent with the cosmochemical record in our Solar system which shows that large and differentiated bodies had already begun to form $\lesssim$1 Myr after the condensation of calcium-aluminum-rich inclusions (CAIs), the oldest minerals in the Solar system (Qin et al., 2008; Kleine et al., 2009; Kruijer et al., 2014).

## 5.8 Acknowledgement

This paper makes use of the following ALMA data sets:
ADS/JAO.ALMA#2011.0.00015.SV. ALMA is a partnership of ESO (representing its member states), NSF (USA) and NINS (Japan), together with NRC (Canada) and NSC and ASIAA (Taiwan) and KASI (Republic of Korea), in cooperation with the Republic of Chile. The Joint ALMA Observatory is operated by ESO, AUI/NRAO and NAOJ. The authors acknowledge support provided by the NASA Origins of Solar Systems, NSF Astronomy & Astrophysics and NSF INSPIRE (AST-1344133) grants programs.

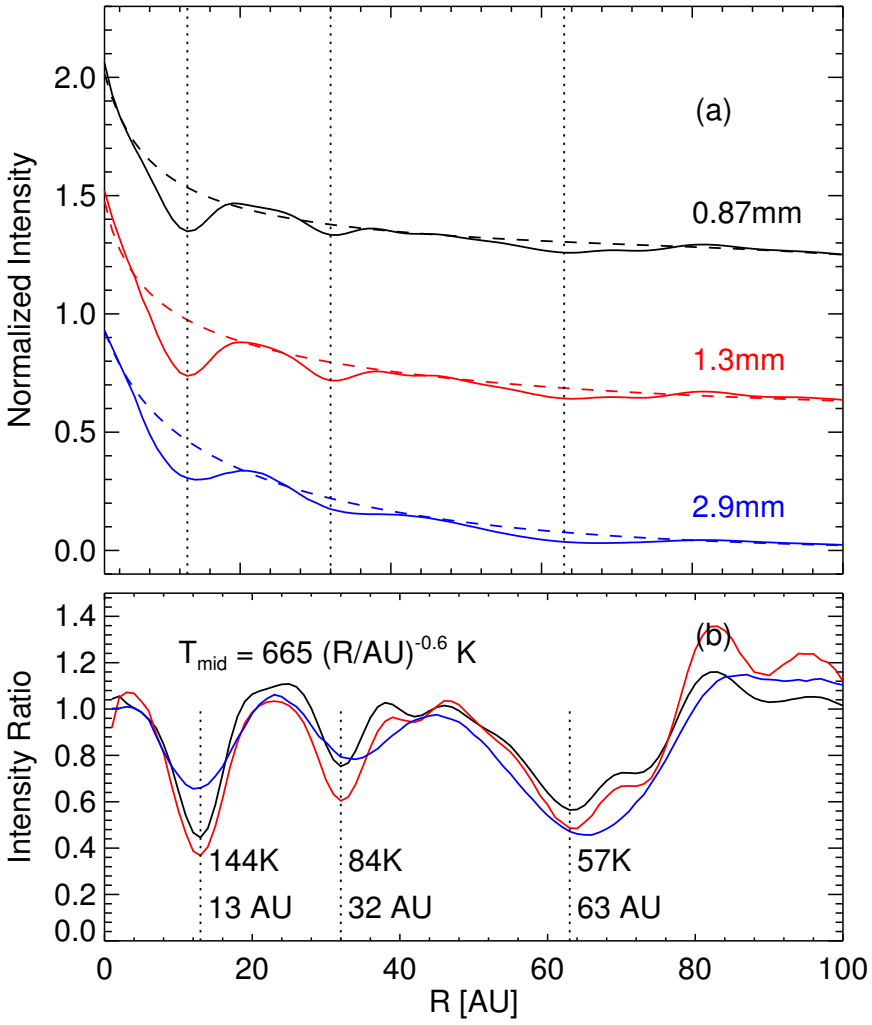


Figure 5.1 (a) Normalized radial surface brightness distributions of HL Tau at 0.87 (blue), 1.3 (red), and 2.9 mm (black). The solid lines depict the observations, dashed lines the best-fit models (described in §3). (b) The observation-to-model surface brightness ratio. The three dotted vertical lines indicate the dip minima.

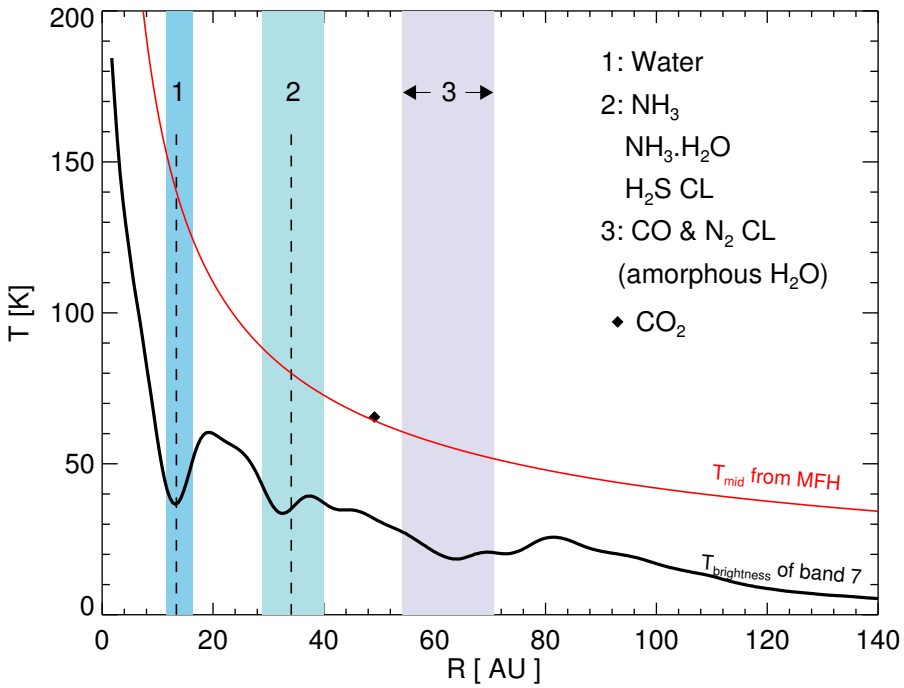


Figure 5.2 The expected condensation fronts in the disk mid-plane of HL Tau. The shaded areas show the clathrate-hydrate (abbreviated as CL in the legend) condensation temperature ranges given in Table 5.2, the vertical lines the mean condensation front radii. The thick solid curve is the brightness temperature distribution of the 0.87 mm image, the thin curve the mid-plane temperature from MFH. A black diamond denotes the condensation temperature of pure $CO_2$ frost, which is close to edge of the 63 AU dip.

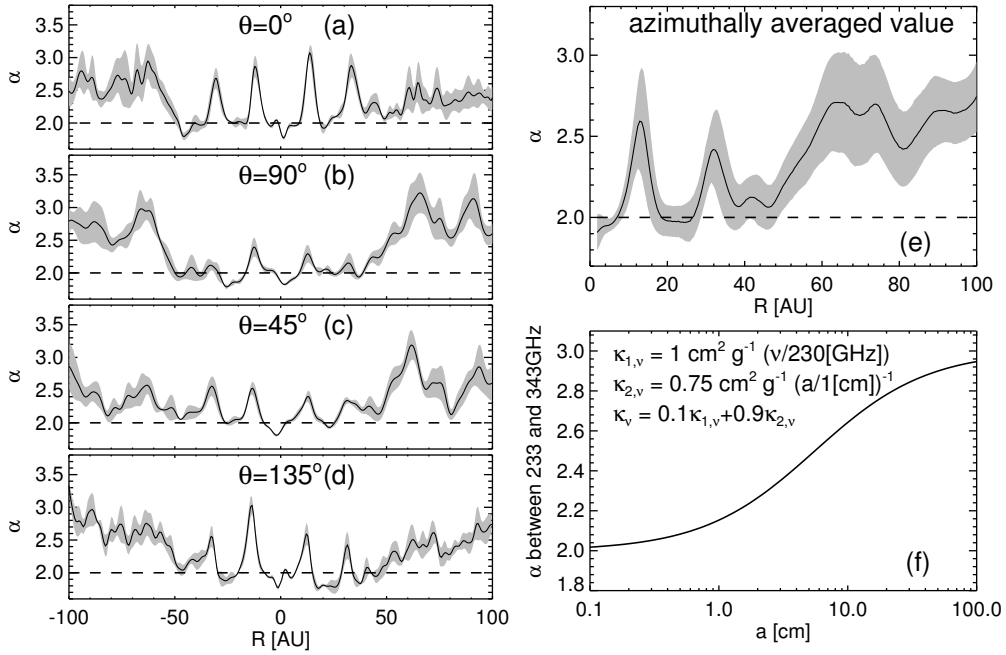


Figure 5.3 Panels (a)-(d): crosscuts of the spectral index $\alpha$, measured between bands 6 and 7, at four angles ($\theta$ starts from the west). The grey regions depict $1\sigma$ uncertainty intervals. Panel (e): An azimuthal average of the continuum spectral index $\alpha$. The grey region again shows the $1\,\sigma$ uncertainty range. Panel (f): Spectral index $\alpha$ as a function of average dust size, $\bar{a}$, in the large dust aggregate population.

# Chapter 6

# Conclusions and Future Directions

## 6.1 Summary of this thesis

Planets are born in disks rotating around young stars. Gas, dust and ice in disks provide raw materials for planetesimal and planet formation. Therefore their mass distribution and composition largely regulate the final demography and habitability of a planetary system.

Among molecular species in disks, volatiles play a key role in planet formation. Beyond water condensation front, water and organic ices dominate the available solid mass for planetesimal and planet formation. Condensation can significantly enhance the local mass surface density of solids in the disk (Hayashi 1981, Stevenson & Lunine 1988), which in turn greatly shortens the time scale needed to form protoplanets in core-accretion models (Pollack et al. 1996). Furthermore, snow lines of the principal solid-vapor reservoirs set the rough boundaries of planetesimals with different elemental compositions, which further determine the bulk composition of terrestrial planets and cores of gas or ice giants (Öberg et al. 2011).

The goal of this thesis is to advance our knowledge of volatiles in protoplanetary disks. In particular, I seek questions to two important questions.

- How are volatiles distributed throughout a disk?
- How do we use volatile emissions to probe dust growth and dynamics in a planet-forming disk?

The works of this thesis are summarized as following:

In Chapter 2, I constrained the radial water vapor content near the surface of the TW Hya transitional protoplanetary disk using multi-wavelength spectra from *Spitzer* and *Herschel* space telescopes. This multi-wavelength mapping method was novel and this study provides the first observational detection of water snowline in a protoplanetary disk beyond the Solar System.

In Chapter 3, I analyzed the high spatial resolution ALMA images of CO and 880 $\mu$m dust emissions in the transition disk J1604-2130. I found that the CO gas and mm-sized dust are truncated at distinctive inner radii, and the dust emission is confined in a narrow ring region. These peculiar morphologies of dust and gas are consistent with the predictions of pressure trapping models that include hydrodynamical disk-planet interactions and dust coagulation/fragmentation processes. These observations are one of the first pieces of evidence for pressure trapping in disks.

In Chapter 4, I presented a case study of using spectroscopic monitoring of young stars and their accretion disks to understand dynamics at play. The classical T Tauri star AA Tau recently showed enhanced CO absorption features along with a significant dimming in its optical brightness. These newly appeared absorptions provide constraints on temperature and column density on the absorbing gas along the line of sight. We suggest that the dimming and absorption are caused by gas and dust lifted to large heights by a magnetic buoyancy instability. This material is now propagating inward, and on reaching the star within a few years will be observed as an accretion outburst.

In Chapter 5, I provided the first observational evidence of fast pebble growth near condensation fronts in protoplanetary disks. Analyzing the ALMA long-baseline science demonstration observations of the HL Tau protoplanetary disk at 2.9, 1.3 and 0.87 mm continuum, I found that the prominent dark rings in the disk are remarkably close to the expected mid-plane condensation front of abundant volatiles ($H_2O$, $NH_3$, CO and $N_2$), and the dust properties inside the rings are consistent with the expectation of pebble growth. Such growth is in accord with recent numerical simulations of volatile condensation, dust coagulation and settling.

The works of this thesis show that we are starting to observationally constrain the initial distribution of chemical compounds in planet-forming disks, and volatiles emission maps provide a powerful probe to understand on-going processes in disks.

## 6.2 Future directions

The next a couple of years represent tremendous opportunities to study planetesimal and planet formation. As ALMA has entered into a phase where science observations dominate activities and started its long-baseline operation, spatially resolved gas/dust emission at planet-forming distance from young stars will soon be available for a large number of sources. These observations will reveal remarkably detailed physical and chemical structures in planet-forming disks (e.g. Partnership et al. 2015). Furthermore, complex organic molecules are starting to be detected in disks thanks to the great sensitivity of ALMA (Öberg et al., 2015). All of these observations will thus for the first time provide abundant constraints to chemical and dynamical models of protoplanetary disks.

### 6.2.1 Opportunities from ALMA

One particular exciting opportunity is that ALMA will reveal if planet preferentially form in some regions in a planet-forming disk.

Regions near snowlines have long been thought to be preferential sites for planet(esimal) formation in the disks around young stars (Hayashi, 1981; Stevenson & Lunine, 1988; Kennedy & Kenyon, 2008). Recent experimental and numerical simulations of dust growth further confirm that snow lines may play a crucial role in planetesimal formation. The first reason is that the growth efficiency of dust grains are likely to be composition dependent. Lab experiments show that icy aggregates are significantly more 'sticky', and resistant to compaction than bare silicate aggregates. And, enhanced local surface mass densities near the condensation fronts may produce pressure pumps or high dust-to-gas mass ratios that can trigger various instabilities that

form planetesimals (Kretke & Lin, 2007; Drążkowska & Dullemond, 2014). Coagulation simulations have consistently shown that fast dust growth can occur around the water condensation front – millimeter-sized particles can grow to decimeter-sized pebbles on a time scale of 1000s of years (Ros & Johansen, 2013). Once a critical decimeter-sized pebble population is formed, streaming instabilities can readily drive the creation of km-sized or larger planetsimals in the mid-plane of protoplanetary disks (Johansen et al., 2014). If fast pebble growth does preferentially occur around the condensation fronts of abundant volatiles, this would suggest snow lines largely regulate the formation and chemical composition of planetesimals, and ultimately the formation of planets and their bulk composition.

With the advent of ALMA long baseline capabilities, it is now possible to directly image angular scales of snowlines in the closest star-forming molecular clouds. Young, actively accreting objects are good initial targets because their luminosities and disk temperature profiles move the condensation fronts out to larger distances (Kennedy & Kenyon, 2008). It is remarkable to see the coincidence between dark rings in the continuum images of the HL Tau disk and its expected mid-plane snowlines (see Figure 6.1, Blake & Bergin 2015, Zhang et al. 2015). These observations might have provided the first hint of preferential formation of planet(esimal) around snowlines.

By taking spatially resolved images of optically thin emission from rare isotopologue molecules, ALMA can probe the temperature structure deep in disks and thus directly constrain the location of mid-plane snowlines.

### 6.2.2 Combining multi-wavelength observations

However, even an amazing facility like ALMA cannot directly detect gas at/inside of the water snow line in most low accretion rate classical T Tauri stars (Kennedy & Kenyon, 2008). Thankfully, on the medium term horizon there is the JWST and the ELT/TMT platforms that will come on-line and transform the spectroscopic opportunities in the near- to mid-IR. Combined, ALMA/JWST/TMT-ELT will be sensitive to gas across all distances in protoplanetary disks, and with sufficient throughput to

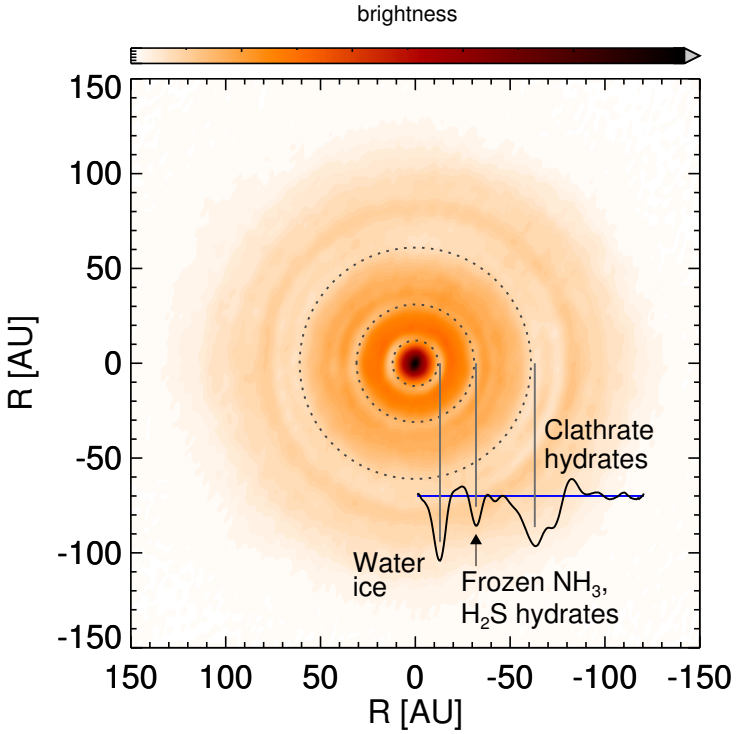


Figure 6.1 A deprojected 1.0 $\mu$m continuum ALMA SV image of the HL Tau protoplanetary disk. The dotted circles represent the locations of emission dips in the long baseline data, radii at which water ice, frozen ammonia/hydrogen sulfide hydrates, and clathrate hydrates with CO and nitrogen are expected to condense using the mid-plane temperature distribution of Men'shchikov et al. (1999). The black curve at lower right shows the radial distribution of surface brightness normalized against a smooth disk profile.

enable the study >100 objects across all stages of planetary system assembly.

# Bibliography

Adams, F. C., Lada, C. J., & Shu, F. H. 1987, ApJ, 312, 788

Aikawa, Y., Miyama, S. M., Nakano, T., & Umebayashi, T. 1996, ApJ, 467, 684

Akeson, R. L., Millan-Gabet, R., Ciardi, D. R., Boden, A. F., Sargent, A. I., Monnier, J. D., McAlister, H., ten Brummelaar, T., Sturmann, J., Sturmann, L., & Turner, N. 2011, ApJ, 728, 96

Alexander, R. 2014, in IAU Symposium, Vol. 299, IAU Symposium, ed. M. Booth, B. C. Matthews, & J. R. Graham, 179–189

Alexander, R. D., & Armitage, P. J. 2007, MNRAS, 375, 500

Alexander, R. D., Clarke, C. J., & Pringle, J. E. 2006a, MNRAS, 369, 216

—. 2006b, MNRAS, 369, 229

Ali-Dib, M., Mousis, O., Petit, J.-M., & Lunine, J. I. 2014, ApJ, 793, 9

Andrews, S. M., Rosenfeld, K. A., Wilner, D. J., & Bremer, M. 2011, ApJ, 742, L5

Andrews, S. M., & Williams, J. P. 2007, ApJ, 659, 705

Andrews, S. M., Wilner, D. J., Espaillat, C., Hughes, A. M., Dullemond, C. P., McClure, M. K., Qi, C., & Brown, J. M. 2011, ApJ, 732, 42

Andrews, S. M., Wilner, D. J., Hughes, A. M., Qi, C., & Dullemond, C. P. 2009, ApJ, 700, 1502

Andrews, S. M., Wilner, D. J., Hughes, A. M., Qi, C., Rosenfeld, K. A., Öberg, K. I., Birnstiel, T., Espaillat, C., Cieza, L. A., Williams, J. P., Lin, S.-Y., & Ho, P. T. P. 2012, ApJ, 744, 162

Armitage, P. J. 2011, ARA&A, 49, 195

Arnold, T. J., Eisner, J. A., Monnier, J. D., & Tuthill, P. 2012, ApJ, 750, 119

Artymowicz, P., & Lubow, S. H. 1994, AJ, 421, 651

Banzatti, A., Meyer, M. R., Bruderer, S., Geers, V., Pascucci, I., Lahuis, F., Juhász, A., Henning, T., & Ábrahám, P. 2012, ApJ, 745, 90

Baulch, D. L., ed. 1972, Evaluated kinetic data for high temperature reactions (CRC Press)

Beckwith, S. V. W., & Sargent, A. I. 1991, ApJ, 381, 250

—. 1993, ApJ, 402, 280

Beckwith, S. V. W., Sargent, A. I., Chini, R. S., & Guesten, R. 1990, ApJ, 99, 924

Benz, W. 2000, Space Sci. Rev., 92, 279

Bergin, E. A., Cleeves, L. I., Gorti, U., Zhang, K., Blake, G. A., Green, J., Andrews, S. M., Evans, II, N. J., Henning, T., Oberg, K., Pontoppidan, K. M., Salyk, C., & van Dishoeck, E. F. 2013, Nature, 393, 7433

Bergin, E. A., Hogerheijde, M. R., Brinch, C., & Fogel, J. e. a. 2010, A&A, 521, L33+

Bethell, T., & Bergin, E. 2009, Science, 326, 1675

Birnstiel, T., Andrews, S. M., & Ercolano, B. 2012, A&A, 544, A79

Birnstiel, T., Dullemond, C. P., & Brauer, F. 2009, Astronomy and Astrophysics, 503, L5

Bitsch, B., Morbidelli, A., Lega, E., Kretke, K., & Crida, A. 2014, A&A, 570, A75

Blake, G. A., & Bergin, E. A. 2015, Nature, 520, 161

Blake, G. A., & Boogert, A. C. A. 2004, ApJ, 606, L73

Blum, J., & Wurm, G. 2008, ARA&A, 46, 21

Bouvier, J., Alencar, S. H. P., Boutelier, T., Dougados, C., Balog, Z., Grankin, K., Hodgkin, S. T., Ibrahimov, M. A., Kun, M., Magakian, T. Y., & Pinte, C. 2007, A&A, 463, 1017

Bouvier, J., Chelli, A., Allain, S., Carrasco, L., Costero, R., Cruz-Gonzalez, I., Dougados, C., Fernández, M., Martín, E. L., Ménard, F., Mennessier, C., Mujica, R., Recillas, E., Salas, L., Schmidt, G., & Wichmann, R. 1999, A&A, 349, 619

Bouvier, J., Grankin, K., Ellerbroek, L. E., Bouy, H., & Barrado, D. 2013, A&A, 557, A77

Bouvier, J., Grankin, K. N., Alencar, S. H. P., Dougados, C., Fernández, M., Basri, G., Batalha, C., Guenther, E., Ibrahimov, M. A., Magakian, T. Y., Melnikov, S. Y., Petrov, P. P., Rud, M. V., & Zapatero Osorio, M. R. 2003, A&A, 409, 169

Brown, J. M., Blake, G. A., Qi, C., Dullemond, C. P., & Wilner, D. J. 2008, ApJ, 675, L109

Brown, J. M., Blake, G. A., Qi, C., Dullemond, C. P., Wilner, D. J., & Williams, J. P. 2009, ApJ, 704, 496

Brown, J. M., Pontoppidan, K. M., van Dishoeck, E. F. v., Herczeg, G. J., Blake, G. A., & Smette, A. 2013, ApJ, 770, 94

Bruderer, S. 2013, A&A, 559, 46

Bruderer, S., van der Marel, N., van Dishoeck, E. F. v., & van Kempen, T. A. 2014, A&A, 562, 26

Bryden, G., Chen, X., Lin, D. N. C., Nelson, R. P., & Papaloizou, J. C. B. 1999, ApJ, 514, 344

Calvet, N., D'Alessio, P., Hartmann, L., Wilner, D., Walsh, A., & Sitko, M. 2002, ApJ, 568, 1008

Carpenter, J. M., Mamajek, E. E., Hillenbrand, L. A., & Meyer, M. R. 2006, ApJ, 651, L49

—. 2009, ApJ, 705, 1646

Carpenter, J. M., Ricci, L., & Isella, A. 2014, ApJ, 787, 42

Carr, J. S., & Najita, J. R. 2008, Science, 319, 1504

Casassus, S., van der Plas, G., M, S. P., Dent, W. R. F., Fomalont, E., Hagelberg, J., Hales, A., Jordán, A., Mawet, D., Ménard, F., Wootten, A., Wilner, D., Hughes, A. M.,

Schreiber, M. R., Girard, J. H., Ercolano, B., Canovas, H., Román, P. E., & Salinas, V. 2013, Nature, 493, 191

Ciesla, F. J., & Cuzzi, J. N. 2006, Icarus, 181, 178

Clarke, C. J., Gendrin, A., & Sotomayor, M. 2001, MNRAS, 328, 485

Cox, A. W., Grady, C. A., Hammel, H. B., Hornbeck, J., Russell, R. W., Sitko, M. L., & Woodgate, B. E. 2013, ApJ, 762, 40

Crida, A., Morbidelli, A., & Masset, F. 2006, Icarus, 181, 587

Cutri, R. M., Skrutskie, M. F., van Dyk, S., Beichman, C. A., Carpenter, J. M., Chester, T., Cambresy, L., Evans, T., Fowler, J., Gizis, J., Howard, E., Huchra, J., Jarrett, T., Kopan, E. L., Kirkpatrick, J. D., Light, R. M., Marsh, K. A., McCallon, H., Schneider, S., Stiening, R., Sykes, M., Weinberg, M., Wheaton, W. A., Wheelock, S., & Zacarias, N. 2003, VizieR Online Data Catalog, 2246, 0

Dahm, S. E., & Carpenter, J. M. 2009, AJ, 137, 4024

D'Alessio, P., Calvet, N., & Hartmann, L. 2001, ApJ, 553, 321

D'Alessio, P., Calvet, N., Hartmann, L., Franco-Hernández, R., & Servín, H. 2006, ApJ, 638, 314

Damjanov, I., Jayawardhana, R., Scholz, A., Ahmic, M., Nguyen, D. C., Brandeker, A., & van Kerkwijk, M. H. 2007, ApJ, 670, 1337

Dauphas, N., & Chaussidon, M. 2011, Annual Review of Earth and Planetary Sciences, 39, 351

de Juan Ovelar, M., Min, M., Dominik, C., Thalmann, C., Pinilla, P., Benisty, M., & Birnstiel, T. 2013, A&A, 560, 111

de Zeeuw, P. T., Hoogerwerf, R., de Bruijne, J. H. J., Brown, A. G. A., & Blaauw, A. 1999, AJ, 117, 354

DENIS Consortium. 2005, VizieR Online Data Catalog, 2263, 0

Desch, S. J. 2007, ApJ, 671, 878

Dodson-Robinson, S. E., Willacy, K., Bodenheimer, P., Turner, N. J., & Beichman, C. A. 2009, Icarus, 200, 672

Donati, J. F., Skelly, M. B., Bouvier, J., Gregory, S. G., Grankin, K. N., Jardine, M. M., Hussain, G. A. J., Ménard, F., Dougados, C., Unruh, Y., Mohanty, S., Aurière, M., Morin, J., Farès, R., & the MaPP collaboration. 2010, MNRAS, 409, 1347

Draine, B. T. 2003, ApJ, 598, 1017

Drążkowska, J., & Dullemond, C. P. 2014, A&A, 572, A78

Dullemond, C. P., & Dominik, C. 2004, A&A, 417, 159

—. 2005, A&A, 434, 971

Dutrey, A., Guilloteau, S., Duvert, G., Prato, L., Simon, M., Schuster, K., & Ménard, F. 1996, A&A, 309, 493

Dutrey, A., Guilloteau, S., Piétu, V., Chapillon, E., Gueth, F., Henning, T., Launhardt, R., Pavlyuchenkov, Y., Schreyer, K., & Semenov, D. 2008, A&A, 490, L15

Eisner, J. A., Chiang, E. I., & Hillenbrand, L. A. 2006, ApJ, 637, L133

Esau, C. F., Harries, T. J., & Bouvier, J. 2014, MNRAS, 443, 1022

Evans, II, N. J., Dunham, M. M., Jørgensen, J. K., Enoch, M. L., Merín, B., van Dishoeck, E. F., Alcalá, J. M., Myers, P. C., Stapelfeldt, K. R., Huard, T. L., Allen, L. E., Harvey, P. M., van Kempen, T., Blake, G. A., Koerner, D. W., Mundy, L. G., Padgett, D. L., & Sargent, A. I. 2009, ApJS, 181, 321

Fedele, D., Bruderer, S., van Dishoeck, E. F. v., Herczeg, G. J., Evans, N. J., Bouwman, J., Henning, T., & Green, J. 2012, A&A, 544, L9

Feigelson, E. D., Getman, K., Townsley, L., Garmire, G., Preibisch, T., Grosso, N., Montmerle, T., Muench, A., & McCaughrean, M. 2005, ApJS, 160, 379

Frisch, P. C., & Slavin, J. D. 2003, ApJ, 594, 844

Fu, W., Li, H., Lubow, S., & Li, S. 2014, arXiv.org

Garaud, P., & Lin, D. N. C. 2007, ApJ, 654, 606

Glassgold, A. E., Meijerink, R., & Najita, J. R. 2009, ApJ, 701, 142

Glassgold, A. E., Najita, J. R., & Igea, J. 2004, ApJ, 615, 972

Gomes, R., Levison, H. F., Tsiganis, K., & Morbidelli, A. 2005, Nature, 435, 466

Gorti, U., Dullemond, C. P., & Hollenbach, D. 2009, ApJ, 705, 1237

Gorti, U., Hollenbach, D., Najita, J. R., & Pascucci, I. 2011, ApJ, 735, 90

Grankin, K. N., Melnikov, S. Y., Bouvier, J., Herbst, W., & Shevchenko, V. S. 2007, A&A, 461, 183

Grosso, N., Bouvier, J., Montmerle, T., Fernández, M., Grankin, K., & Zapatero Osorio, M. R. 2007, A&A, 475, 607

Gutermuth, R. A., Myers, P. C., Megeath, S. T., Allen, L. E., Pipher, J. L., Muzerolle, J., Porras, A., Winston, E., & Fazio, G. 2008, ApJ, 674, 336

Güttler, C., Blum, J., Zsom, A., Ormel, C. W., & Dullemond, C. P. 2010, A&A, 513, A56

Haisch, Jr., K. E., Lada, E. A., & Lada, C. J. 2001, ApJ, 553, L153

Hartmann, L., Hewett, R., Stahler, S., & Mathieu, R. D. 1986, ApJ, 309, 275

Hasegawa, T. I., & Herbst, E. 1993, MNRAS, 261, 83

Hayashi, C. 1981, Progress of Theoretical Physics Supplement, 70, 35

Heinzeller, D., Nomura, H., Walsh, C., & Millar, T. J. 2011, ApJ, 731, 115

Henning, T., & Semenov, D. 2013, Chemical Reviews, 113, 9016

Hirose, S., & Turner, N. J. 2011, ApJ, 732, L30

Hogerheijde, M. R., Bergin, E. A., Brinch, C., Cleeves, L. I., Fogel, J. K. J., Blake, G. A., Dominik, C., Lis, D. C., Melnick, G., Neufeld, D., Panic, O., Pearson, J. C., Kristensen, L., Yldz, U. A., & van Dishoeck, E. F. v. 2011, Science, 334, 338

Horne, K. 1986, PASP, 98, 609

Hubbard, A., & Ebel, D. S. 2014, Icarus, 237, 84

Hughes, A. M., Andrews, S. M., Espaillat, C., Wilner, D. J., Calvet, N., D'Alessio, P., Qi, C., Williams, J. P., & Hogerheijde, M. R. 2009, ApJ, 698, 131

Hughes, A. M., Wilner, D. J., Calvet, N., D'Alessio, P., Claussen, M. J., & Hogerheijde, M. R. 2007, ApJ, 664, 536

Hughes, A. M., Wilner, D. J., Qi, C., & Hogerheijde, M. R. 2008, ApJ, 678, 1119

Ireland, M. J., Kraus, A., Martinache, F., Law, N., & Hillenbrand, L. A. 2011, ApJ, 726, 113

Iro, N., Gautier, D., Hersant, F., Bockelée-Morvan, D., & Lunine, J. I. 2003, Icarus, 161, 511

Isella, A., Carpenter, J. M., & Sargent, A. I. 2009, ApJ, 701, 260

Isella, A., Natta, A., Wilner, D., Carpenter, J. M., & Testi, L. 2010, ApJ, 725, 1735

Isella, A., Pérez, L. M., & Carpenter, J. M. 2012, ApJ, 747, 136

Isella, A., Pérez, L. M., Carpenter, J. M., Ricci, L., Andrews, S., & Rosenfeld, K. 2013, ApJ, 775, 30

Isella, A., Testi, L., & Natta, A. 2006, A&A, 451, 951

Isella, A., Testi, L., Natta, A., Neri, R., Wilner, D., & Qi, C. 2007, A&A, 469, 213

Johansen, A., Blum, J., Tanaka, H., Ormel, C., Bizzarro, M., & Rickman, H. 2014, Protostars and Planets VI, 547

Johansen, A., Oishi, J. S., Mac Low, M.-M., Klahr, H., Henning, T., & Youdin, A. 2007, Nature, 448, 1022

Johansen, A., Youdin, A., & Mac Low, M.-M. 2009, ApJ, 704, L75

Kamp, I., & Dullemond, C. P. 2004, ApJ, 615, 991

Kelling, T., Wurm, G., & Köster, M. 2014, ApJ, 783, 111

Kennedy, G. M., & Kenyon, S. J. 2008, ApJ, 673, 502

Kleine, T., Touboul, M., Bourdon, B., Nimmo, F., Mezger, K., Palme, H., Jacobsen, S. B., Yin, Q.-Z., & Halliday, A. N. 2009, Geochim. Cosmochim. Acta, 73, 5150

Kraus, A. L., Ireland, M. J., Martinache, F., & Lloyd, J. P. 2008, ApJ, 679, 762

Kretke, K. A., & Lin, D. N. C. 2007, ApJ, 664, L55

Kruijer, T. S., Touboul, M., Fischer-Gödde, M., Bermingham, K. R., Walker, R. J., & Kleine, T. 2014, Science, 344, 1150

Lada, C. J., & Wilking, B. A. 1984, ApJ, 287, 610

Lecar, M., Podolak, M., Sasselov, D., & Chiang, E. 2006, ApJ, 640, 1115

Lewis, J. S. 1971, Icarus, 15, 174

Lin, D. N. C., & Papaloizou, J. 1979, MNRAS, 186, 799

Low, F. J., Smith, P. S., Werner, M., Chen, C., Krause, V., Jura, M., & Hines, D. C. 2005, ApJ, 631, 1170

Luhman, K. L., & Mamajek, E. E. 2012, ApJ, 758, 31

Luhman, K. L., Whitney, B. A., Meade, M. R., Babler, B. L., Indebetouw, R., Bracker, S., & Churchwell, E. B. 2006, ApJ, 647, 1180

Luna, R., Satorre, M. Á., Santonja, C., & Domingo, M. 2014, A&A, 566, A27

Lunine, J. I., & Stevenson, D. J. 1985, ApJS, 58, 493

Lynden-Bell, D., & Pringle, J. E. 1974, MNRAS, 168, 603

Mamajek, E. E. 2005, ApJ, 634, 1385

Martín-Doménech, R., Muñoz Caro, G. M., Bueno, J., & Goesmann, F. 2014, A&A, 564, A8

Mathews, G. S., Pinte, C., Duchêne, G., Williams, J. P., & Ménard, F. 2013, A&A, 558, 66

Mathews, G. S., Williams, J. P., & Ménard, F. 2012, ApJ, 753, 59

Mathews, G. S., Williams, J. P., Ménard, F., Phillips, N., Duchêne, G., & Pinte, C. 2012, ApJ, 745, 23

Mathis, J. S. 1990, ARA&A, 28, 37

Mayama, S., Hashimoto, J., Muto, T., Tsukagoshi, T., Kusakabe, N., Kuzuhara, M., Takahashi, Y., Kudo, T., Dong, R., Fukagawa, M., Takami, M., Momose, M., Wisniewski, J. P., Follette, K., Abe, L., Akiyama, E., Brandner, W., Brandt, T., Carson, J., Egner, S., Feldt, M., Goto, M., Grady, C. A., Guyon, O., Hayano, Y., Hayashi, M., Hayashi, S., Henning, T., Hodapp, K. W., Ishii, M., Iye, M., Janson, M., Kandori, R., Kwon, J., Knapp, G. R., Matsuo, T., McElwain, M. W., Miyama, S., Morino, J.-I., Moro-Martin, A., Nishimura, T., Pyo, T.-S., Serabyn, E., Suto, H., Suzuki, R., Takato, N., Terada, H., Thalmann, C., Tomono, D., Turner, E. L., Watanabe, M., Yamada, T., Takami, H., Usuda, T., & Tamura, M. 2012, ApJ, 760, L26

McLean, I. S., Becklin, E. E., Bendiksen, O., Brims, G., Canfield, J., Figer, D. F., Graham, J. R., Hare, J., Lacayanga, F., Larkin, J. E., Larson, S. B., Levenson, N., Magnone, N., Teplitz, H., & Wong, W. 1998, in Society of Photo-Optical Instrumentation Engineers (SPIE) Conference Series, Vol. 3354, Infrared Astronomical Instrumentation, ed. A. M. Fowler, 566–578

McMullin, J. P., Waters, B., Schiebel, D., Young, W., & Golap, K. 2007, in Astronomical Society of the Pacific Conference Series, Vol. 376, Astronomical Data Analysis Software and Systems XVI, ed. R. A. Shaw, F. Hill, & D. J. Bell, 127

Meeus, G., Montesinos, B., Mendigutía, I., Kamp, I., Thi, W.-F., & team, t. G. H. 2012, arXiv.org, astro-ph.GA

Meijerink, R., Pontoppidan, K. M., Blake, G. A., Poelman, D. R., & Dullemond, C. P. 2009, ApJ, 704, 1471

Ménard, F., Bouvier, J., Dougados, C., Mel'nikov, S. Y., & Grankin, K. N. 2003, A&A, 409, 163

Men'shchikov, A. B., Henning, T., & Fischer, O. 1999, ApJ, 519, 257

Miller, K. A., & Stone, J. M. 2000, ApJ, 534, 398

Miyake, K., & Nakagawa, Y. 1993, Icarus, 106, 20

Monet, D. G. 1998, in Bulletin of the American Astronomical Society, Vol. 30, American Astronomical Society Meeting Abstracts, 120.03

Mumma, M. J., & Charnley, S. B. 2011, ARA&A, 49, 471

Muzerolle, J., Flaherty, K., Balog, Z., Furlan, E., Smith, P. S., Allen, L., Calvet, N., D'Alessio, P., Megeath, S. T., Muench, A., Rieke, G. H., & Sherry, W. H. 2009, ApJ, 704, L15

Najita, J. R., Ádámkovics, M., & Glassgold, A. E. 2011, ApJ, 743, 147

Najita, J. R., Carr, J. S., Strom, S. E., Watson, D. M., Pascucci, I., Hollenbach, D., Gorti, U., & Keller, L. 2010, ApJ, 712, 274

Natta, A., Testi, L., Calvet, N., Henning, T., Waters, R., & Wilner, D. 2007, Protostars and Planets V, 767

Öberg, K. I., Guzmán, V. V., Furuya, K., Qi, C., Aikawa, Y., Andrews, S. M., Loomis, R., & Wilner, D. J. 2015, Nature, 520, 198

Öberg, K. I., Murray-Clay, R., & Bergin, E. A. 2011, ApJ, 743, L16

Ossenkopf, V., & Henning, T. 1994, A&A, 291, 943

O'Sullivan, M., Truss, M., Walker, C., Wood, K., Matthews, O., Whitney, B., & Bjorkman, J. E. 2005, MNRAS, 358, 632

Panic, O., Hogerheijde, M. R., Wilner, D., & Qi, C. 2009, A&A, 501, 269

Partnership, A., Brogan, C. L., Perez, L. M., & Hunter, e. a. 2015, ArXiv e-prints

Pecaut, M. J., Mamajek, E. E., & Bubar, E. J. 2012, ApJ, 746, 154

Pérez, L. M., Isella, A., Carpenter, J. M., & Chandler, C. J. 2014, ApJ, 783, L13

Piétu, V., Dutrey, A., & Guilloteau, S. 2007, A&A, 467, 163

Piétu, V., Dutrey, A., Guilloteau, S., Chapillon, E., & Pety, J. 2006, A&A, 460, L43

Piétu, V., Guilloteau, S., & Dutrey, A. 2005, A&A, 443, 945

Pinilla, P., Benisty, M., & Birnstiel, T. 2012, A&A, 545, 81

Pollack, J. B., Hollenbach, D., Beckwith, S., Simonelli, D. P., Roush, T., & Fong, W. 1994, ApJ, 421, 615

Pollack, J. B., Hubickyj, O., Bodenheimer, P., Lissauer, J. J., Podolak, M., & Greenzweig, Y. 1996, Icarus, 124, 62

Pollack, J. B., Lunine, J. I., & Tittemore, W. C. 1991, Origin of the Uranian satellites, ed. J. T. Bergstralh, E. D. Miner, & M. S. Matthews, 469–512

Pontoppidan, K. M., Blake, G. A., van Dishoeck, E. F., Smette, A., Ireland, M. J., & Brown, J. 2008, ApJ, 684, 1323

Pontoppidan, K. M., Meijerink, R., Dullemond, C. P., & Blake, G. A. 2009, ApJ, 704, 1482

Pontoppidan, K. M., Salyk, C., Blake, G. A., & Käufl, H. U. 2010a, ApJ, 722, L173

Pontoppidan, K. M., Salyk, C., Blake, G. A., Meijerink, R., Carr, J. S., & Najita, J. 2010b, ApJ, 720, 887

Pontoppidan, K. M., van Dishoeck, E., Blake, G. A., Smith, R., Brown, J., Herczeg, G. J., Bast, J., Mandell, A., Smette, A., Thi, W.-F., Young, E. D., Morris, M. R., Dent, W., & Käufl, H. U. 2011, The Messenger, 143, 32

Preibisch, T., Brown, A. G. A., Bridges, T., Guenther, E., & Zinnecker, H. 2002, ApJ, 124, 404

Pringle, J. E. 1981, ARA&A, 19, 137

Qi, C., Ho, P. T. P., Wilner, D. J., Takakuwa, S., Hirano, N., Ohashi, N., Bourke, T. L., Zhang, Q., Blake, G. A., Hogerheijde, M. R., Saito, M., Choi, M., & Yang, J. 2004, ApJ, 616, L11

Qi, C., Öberg, K. I., Wilner, D. J., D'Alessio, P., Bergin, E., Andrews, S. M., Blake, G. A., Hogerheijde, M. R., & van Dishoeck, E. F. 2013, Science, 341, 630

Qin, L., Dauphas, N., Wadhwa, M., Masarik, J., & Janney, P. E. 2008, Earth and Planetary Science Letters, 273, 94

Rau, U., & Cornwell, T. J. 2011, A&A, 532, A71

Raymond, S. N., Quinn, T., & Lunine, J. I. 2004, Icarus, 168, 1

Regaly, Z., Juhász, A., Sandor, Z., & Dullemond, C. P. 2012, MNRAS, 419, 1701

Reipurth, B., & Bally, J. 2001, ARA&A, 39, 403

Rettig, T. W., Haywood, J., Simon, T., Brittain, S. D., & Gibb, E. 2004, ApJ, 616, L163

Riviere-Marichalar, P., Ménard, F., Thi, W.-F., Kamp, I., Montesinos, B., Meeus, G., Woitke, P., Howard, C., Sandell, G., Podio, L., Dent, W. R. F., Mendigutía, I., Pinte, C., White, G. J., & Barrado, D. 2012, A&A, 538, L3

Robitaille, T. P., Whitney, B. A., Indebetouw, R., & Wood, K. 2007, ApJS, 169, 328

Ros, K., & Johansen, A. 2013, A&A, 552, A137

Rosenfeld, K. A., Andrews, S. M., Hughes, A. M., Wilner, D. J., & Qi, C. 2013a, ApJ, 774, 16

Rosenfeld, K. A., Andrews, S. M., Wilner, D. J., Kastner, J. H., & McClure, M. K. 2013b, ApJ, 775, 136

Rosenfeld, K. A., Qi, C., Andrews, S. M., Wilner, D. J., Corder, S. A., Dullemond, C. P., Lin, S.-Y., Hughes, A. M., D'Alessio, P., & Ho, P. T. P. 2012, ApJ, 757, 129

Rucinski, S. M., & Krautter, J. 1983, A&A, 121, 217

Salyk, C., Blake, G. A., Boogert, A. C. A., & Brown, J. M. 2007, ApJ, 655, L105

—. 2009, ApJ, 699, 330

—. 2011, ApJ, 743, 112

Salyk, C., Pontoppidan, K. M., Blake, G. A., Lahuis, F., van Dishoeck, E. F., & Evans, II, N. J. 2008, ApJ, 676, L49

Salyk, C., Pontoppidan, K. M., Blake, G. A., Najita, J. R., & Carr, J. S. 2011, ApJ, 731, 130

Sandford, S. A., & Allamandola, L. J. 1993, Icarus, 106, 478

Schmitt, J. H. M. M., & Robrade, J. 2007, A&A, 462, L41

Schwarz, K. R., & Bergin, E. A. 2014, ApJ, 797, 113

Seizinger, A., & Kley, W. 2013, A&A, 551, A65

Simon, J. B., Armitage, P. J., & Beckwith, K. 2011a, ApJ, 743, 17

Simon, J. B., Hawley, J. F., & Beckwith, K. 2011b, ApJ, 730, 94

Sitko, M. L., Day, A. N., Kimes, R. L., Beerman, L. C., Martus, C., Lynch, D. K., Russell, R. W., Grady, C. A., Schneider, G., Lisse, C. M., Nuth, J. A., Curé, M., Henden, A. A., Kraus, S., Motta, V., Tamura, M., Hornbeck, J., Williger, G. M., & Fugazza, D. 2012, ApJ, 745, 29

Skrutskie, M. F., Dutkevitch, D., Strom, S. E., Edwards, S., Strom, K. M., & Shure, M. A. 1990, ApJ, 99, 1187

Snow, T. P., & McCall, B. J. 2006, ARA&A, 44, 367

Stevenson, D. J., & Lunine, J. I. 1988, Icarus, 75, 146

Strom, K. M., Strom, S. E., Edwards, S., Cabrit, S., & Skrutskie, M. F. 1989, AJ, 97, 1451

Supulver, K. D., & Lin, D. N. C. 2000, Icarus, 146, 525

Suzuki, T. K., & Inutsuka, S.-i. 2009, ApJ, 691, L49

Tang, Y. W., Guilloteau, S., Piétu, V., Dutrey, A., Ohashi, N., & Ho, P. T. P. 2012, A&A, 547, 84

Terquem, C., & Papaloizou, J. C. B. 2000, A&A, 360, 1031

Testi, L., Birnstiel, T., Ricci, L., Andrews, S., Blum, J., Carpenter, J., Dominik, C., Isella, A., Natta, A., Williams, J., & Wilner, D. 2014, Protostars and Planets VI

Thi, W.-F., Mathews, G., Ménard, F., Woitke, P., Meeus, G., Riviere-Marichalar, P., Pinte, C., Howard, C. D., Roberge, A., Sandell, G., Pascucci, I., Riaz, B., Grady, C. A., Dent, W. R. F., Kamp, I., Duchêne, G., Augereau, J.-C., Pantin, E., Vandenbussche, B., Tilling, I., Williams, J. P., Eiroa, C., Barrado, D., Alacid, J. M., Andrews, S., Ardila, D. R., Aresu, G., Brittain, S., Ciardi, D. R., Danchi, W., Fedele, D., de Gregorio-Monsalvo, I., Heras, A., Huelamo, N., Krivov, A., Lebreton, J., Liseau, R., Martin-Zaidi, C., Mendigutía, I., Montesinos, B., Mora, A., Morales-Calderon, M., Nomura, H., Phillips, N., Podio, L., Poelman, D. R., Ramsay, S., Rice, K., Solano, E., Walker, H., White, G. J., & Wright, G. 2010, A&A, 518, L125

Tielens, A. G. G. M., & Hagen, W. 1982, A&A, 114, 245

Turner, N. J., Fromang, S., Gammie, C., Klahr, H., Lesur, G., Wardle, M., & Bai, X.-N. 2014, Protostars and Planets VI

Turner, N. J., Sano, T., & Dziourkevitch, N. 2007, ApJ, 659, 729

Uchida, K. I., Calvet, N., Hartmann, L., Kemper, F., Forrest, W. J., Watson, D. M., D'Alessio, P., Chen, C. H., Furlan, E., Sargent, B., Brandl, B. R., Herter, T. L., Morris, P., Myers, P. C., Najita, J. R., Sloan, G. C., Barry, D. J., Green, J., Keller, L. D., & Hall, P. 2004, ApJS, 154, 439

van der Marel, N., van Dishoeck, E. F. v., Bruderer, S., Birnstiel, T., Pinilla, P., Dullemond, C. P., van Kempen, T. A., Schmalzl, M., Brown, J. M., Herczeg, G. J., Mathews, G. S., & Geers, V. 2013, Science, 340, 1199

van Dishoeck, E. F., Herbst, E., & Neufeld, D. A. 2013, Chemical Reviews, 113, 9043

Visser, R., van Dishoeck, E. F. v., & Black, J. H. 2009, A&A, 503, 323

Walsh, C., Millar, T. J., & Nomura, H. 2010, ApJ, 722, 1607

Walsh, C., Nomura, H., Millar, T. J., & Aikawa, Y. 2012, ApJ, 747, 114

Webb, R. A., Zuckerman, B., Platais, I., Patience, J., White, R. J., Schwartz, M. J., & McCarthy, C. 1999, ApJ, 512, L63

Weidenschilling, S. J. 1997, Icarus, 127, 290

Weintraub, D. A., Sandell, G., & Duncan, W. D. 1989, ApJ, 340, L69

Wilson, T. L. 1999, Reports on Progress in Physics, 62, 143

Woitke, P., Kamp, I., & Thi, W.-F. 2009, A&A, 501, 383

Wolk, S. J., & Walter, F. M. 1996, AJ, 111, 2066

Zacharias, N., Monet, D. G., Levine, S. E., Urban, S. E., Gaume, R., & Wycoff, G. L. 2005, VizieR Online Data Catalog, 1297, 0

Zhu, Z., Hartmann, L., Calvet, N., Hernandez, J., Muzerolle, J., & Tannirkulam, A.-K. 2007, ApJ, 669, 483

Zhu, Z., Hartmann, L., & Gammie, C. 2010, ApJ, 713, 1143

Zhu, Z., Nelson, R. P., Dong, R., Espaillat, C., & Hartmann, L. 2012, ApJ, 755, 6

Zubko, V. G., Mennella, V., Colangeli, L., & Bussoletti, E. 1996, MNRAS, 282, 1321